7-2015

Design, Fabrication, and Measurement of a Multiple-Input Multiple-Output (MIMO) Antenna for Mobile Communication

Christopher Charles Arnold
University of Arkansas, Fayetteville

Design, Fabrication, and Measurement of a Multiple-Input Multiple-Output (MIMO) Antenna for Mobile Communication

Design, Fabrication, and Measurement of a Multiple-Input Multiple-Output (MIMO) Antenna for Mobile Communication

A thesis submitted in partial fulfillment
of the requirements for the degree of
Master of Science in Electrical Engineering

by

Christopher C. Arnold
University of Arkansas
Bachelor of Science in Electrical Engineering, 2013

July 2015
University of Arkansas

This thesis is approved for recommendation to the Graduate Council.

Dr. Magda El-Shenawee
Thesis Director

Dr. Jingxian Wu
Committee Member

Dr. Roy McCann
Committee Member

Abstract

This thesis presents the design, fabrication and characterization of a multiband uniplanar MIMO antenna for hand-held mobile communication devices on LTE, WLAN, and WMAN networks. The antenna design methodology combined a variety of broadbanding techniques that resulted in a single-layer hybrid monopole antenna coupled to a meander line element and parasitic structures. The 115×55×1.54 mm antenna was fabricated using an FR4 composite material and occupies only a fractional volume within the size of an average cellular phone allowing ample space to integrate with existing hardware. Characterization of the MIMO antenna included input impedance, scattering parameters and radiation pattern cross sections that were all measured from 500-6500 MHz inside an anechoic chamber. The measurement results indicated four main operating regions of the multiband antenna centered at 875 MHz, 2300 MHz, 3500 MHz, and 5700 MHz with bandwidths of 240 MHz, 740 MHz, 190 MHz, and 370 MHz respectively. Scattering parameter measurements demonstrated excellent coverage of the desired communication spectrum, being able to operate on 30 of the 42 defined LTE bands, as well as common WLAN and WMAN bands. The radiation pattern cross sections in each of the operating regions showed non-directional behavior that is desirable for mobile communication devices. Additionally the envelope correlation coefficient calculated from the measured complex scattering parameters verified that the MIMO antenna achieved good system diversity. Overall, this work resulted in a multiband uniplanar MIMO antenna system suitable for hand-held mobile communication devices. Utilizing cost effective materials and simple geometries allowed fabrication using common methods. The novel antenna can support the high capacity required from evolving communication systems and represents a practical option for use within future generations of mobile devices.

Acknowledgements

I would like to acknowledge and thank Dr. Magda El-Shenawee for her support as my advisor. Without her hard work, guidance, and commitment to excellence this thesis would not have been possible. I would also like to thank my committee members Dr. Jingxian Wu and Dr. Roy McCann and all the faculty and staff at the University Of Arkansas Department Of Electrical Engineering.

Special thanks go to my family and close friends for their encouragement and support. To my parents Chris and Amy Arnold, you have given me the confidence to excel in all areas of life. To my loving wife Cierra Arnold, you kept me going through the most difficult times and never doubted my abilities. Finally, to my grandfather Charles Cook, your work ethic, selfless attitude, and unwavering faith inspired me to achieve my goals while always keeping the bigger picture in perspective.

Table of Contents

I. Introduction 1

A. Motivation 1

B. Evolution of Wireless Communication 3

C. Long Term Evolution (LTE) 6

Multiple-Input Multiple-Output (MIMO) Systems 10

D. Other Wireless Networks 12

Wireless Local Area Networks 12

Wireless Metropolitan Area Networks 13

E. Antenna Characterization and Performance Metrics 14

F. Types of Antennas Used in Wireless Communication 19

Multiple-Input Multiple-Output (MIMO) Antennas 26

G. Discussion of Thesis Goals 29

II. Antenna Design and Simulation 31

A. Computational Methodology 31

Model Domain 33

B. Single Antenna Design 34

C. Single Antenna Simulated Characteristics 49

D. MIMO Antenna Design 56

III. Antenna Fabrication and Measurements 65

A. Fabrication Procedure 65

B. Measurement Equipment 66

C. MIMO Antenna Characterization Results 74

D. Discussion of Measured Results 93

IV. Summary and Conclusion 95

List of Figures

Figure I.1. ITU Statistics showing various types of subscriptions per year 2

Figure I.2. Simple transmission line and antenna model [18] 14

Figure I.3 Radiation pattern and cross sections [18] 15

Figure I.4. Monopole antenna examples 21

Figure I.5. Meander line antenna 23

Figure I.6. Evolution of monopole antennas [19] 24

Figure I.7. Several MIMO configurations showing element and pattern variation 27

Figure II.1. Simulated model domain setup 33

Figure II.2. Antenna model 1 38

Figure II.3. Return loss versus frequency for antenna model 1 38

Figure II.4. Input impedance of antenna model 1 39

Figure II.5. Antenna model 2 40

Figure II.6. Return loss versus frequency for antenna model 2 41

Figure II.7. Input impedance of antenna model 2 41

Figure II.8. Antenna model 3 42

Figure II.9. Return loss versus frequency for antenna model 3 43

Figure II.10. Input impedance of antenna model 3 43

Figure II.11. Antenna model 4 44

Figure II.12. Return loss versus frequency for antenna model 4 45

Figure II.13. Input impedance of antenna of antenna model 4 45

Figure II.14. Antenna model 5 46

Figure II.15. Return loss versus frequency for antenna model 5 47

Figure II.16. Input impedance of antenna model 5 48
Figure II.17. Antenna model 6 49
Figure II.18. Antenna model shown relative to a standard size mobile phone 50
Figure II.19. Single antenna simulated return loss 51
Figure II.20. Simulated radiation patterns of single antenna at 850 MHz 52
Figure II.21. Simulated radiation patterns of single antenna at 2500 MHz 52
Figure II.22. Simulated radiation patterns of single antenna at 3500 MHz 53
Figure II.23. Simulated radiation patterns of single antenna at 5700 MHz 53
Figure II.24. Simulated peak gain for single antenna 54
Figure II.25. Simulated radiation efficiency for single antenna 55
Figure II.26. MIMO simulation model 56
Figure II.27. MIMO simulation scattering parameters 58
Figure II.28. Simulated radiation patterns of MIMO antenna at 850 MHz 59
Figure II.29. Simulated radiation patterns of MIMO antenna at 2500 MHz 59
Figure II.30. Simulated radiation patterns of MIMO antenna at 3500 MHz 60
Figure II.31. Simulated radiation patterns of MIMO antenna at 5700 MHz 60
Figure II.32. Surface currents along ground plane and radiating elements 61
Figure II.33. Simulated peak gain for MIMO antenna 62
Figure II.34. Simulated radiation efficiency for MIMO antenna 63
Figure II.35. Simulated envelope correlation coefficient for MIMO antenna 64
Figure III.1. Fabricated MIMO antenna photograph 66
Figure III.2. Simple block diagram of a network analyzer [78] 67
Figure III.3. Photograph of the HP 8510C network analyzer used for characterization 68

Figure III.4. Input parameter measurement setup comparison 70

Figure III.5. Radiation pattern measurement setup inside anechoic chamber 71

Figure III.6. Photographs of the rotational stage inside the anechoic chamber 72

Figure III.7. Photograph of the dual polarized horn taken inside the anechoic chamber 73

Figure III.8. Measured MIMO antenna scattering parameters 75

Figure III.9. Comparison of measured and simulated S_{11} 75

Figure III.10. Comparison of measured and simulated S_{22} 76

Figure III.11. Comparison of measured and simulated $S_{12,}$ S_{21} 76

Figure III.12. X-Y cross section measured radiation patterns at 850 MHz 79

Figure III.13. X-Z cross section measured radiation patterns at 850 MHz 79

Figure III.14. Z-Y cross section measured radiation patterns at 850 MHz 80

Figure III.15. X-Y cross section measured radiation patterns at 2500 MHz 80

Figure III.16. X-Z cross section measured radiation patterns at 2500 MHz 81

Figure III.17. Y-Z cross section measured radiation patterns at 2500 MHz 81

Figure III.18. X-Y cross section measured radiation patterns at 3500 MHz 82

Figure III.19. X-Z cross section measured radiation patterns at 3500 MHz 82

Figure III.20. Y-Z cross section measured radiation patterns at 3500 MHz 83

Figure III.21. X-Y cross section measured radiation patterns at 5700 MHz 83

Figure III.22. X-Z cross section measured radiation patterns at 5700 MHz 84

Figure III.23. Y-Z cross section measured radiation patterns at 5700 MHz 84

Figure III.24. X-Y cross section measured radiation patterns at 850 MHz plotted against simulated results with coaxial cable included 86

Figure III.25. X-Z cross section measured radiation patterns at 850 MHz plotted against simulated results with coaxial cable included 86

Figure III.26. Z-Y cross section measured radiation patterns at 850 MHz plotted against simulated results with coaxial cable included..... 87

Figure III.27. X-Y cross section measured radiation patterns at 2500 MHz plotted against simulated results with coaxial cable included..... 87

Figure III.28. X-Z cross section measured radiation patterns at 2500 MHz plotted against simulated results with coaxial cable included..... 88

Figure III.29. Y-Z cross section measured radiation patterns at 2500 MHz plotted against simulated results with coaxial cable included..... 88

Figure III.30. X-Y cross section measured radiation patterns at 3500 MHz plotted against simulated results with coaxial cable included..... 89

Figure III.31. X-Z cross section measured radiation patterns at 3500 MHz plotted against simulated results with coaxial cable included..... 89

Figure III.32. Y-Z cross section measured radiation patterns at 3500 MHz plotted against simulated results with coaxial cable included..... 90

Figure III.33. X-Y cross section measured radiation patterns at 5700 MHz plotted against simulated results with coaxial cable included..... 90

Figure III.34. X-Z cross section measured radiation patterns at 5700 MHz plotted against simulated results with coaxial cable included..... 91

Figure III.35. Y-Z cross section measured radiation patterns at 5700 MHz plotted against simulated results with coaxial cable included..... 91

Figure III.36. Measured envelope correlation coefficient for MIMO antenna 92

List of Tables

Table I.1. Overview of Generational Changes in Mobile Communication Technology 6

Table I.2. FDD LTE Bands 7

Table I.3. TDD LTE Frequency Bands 8

Table I.4. Performance Requirement Comparisons 10

Table II.1. Initial Design Parameter Summary 37

I. Introduction

A. Motivation

Reliable mobile communication is a necessity in our modern society. Today's mobile communication devices allow users to enjoy high voice call quality, high speed internet connection, access to email, streaming mobile media, and limitless other applications. Mobile communication technology provides a source of entertainment for many; however, it also fulfils much more critical needs. The ability to instantly contact personnel for medical or other emergencies offers a high sense of security to end users. Access to reliable and consistent wireless communication allows us to connect with people worldwide. Recently mobile communication has had the highest impact in developing countries. The fastest growth rates seen in mobile communication subscriptions are in developing counties, where often there is little or no infrastructure for fixed communication. Mobile communication systems provide a cost effective and reliable solution giving people opportunities to connect, explore, and even become educated. Reliable mobile communication can allow small business to grow and expand, reaching global markets, that were previously not possible. The mobile communication industry has boosted the global economy by providing millions of jobs as well as connecting global markets. In 2014 alone, the mobile industry accounted for 3.8% of global gross domestic product (GDP), corresponding to over US$ 3 trillion in economic value spread across more than 230 countries [1].

Overall, the telecommunications industry has seen unprecedented growth in the past decade. Statistics published by the International Telecommunications Union (ITU) in [2], showed an excess of 6.9 billion mobile-cellular subscriptions in 2014, with over 2.3 billion being active mobile-broadband subscriptions i.e. smart phones with access to the internet. Figure I.1

below, illustrates the recent trends in communication system access. Mobile technology, both cellular and broadband have shown continual growth in the past decade, while fixed-telephone services are in steady decline. This trend in communications, which shows more users going mobile, and less relying on hard-wired systems comes as we continue to progress into cheaper, faster, and more reliable wireless communication standards.

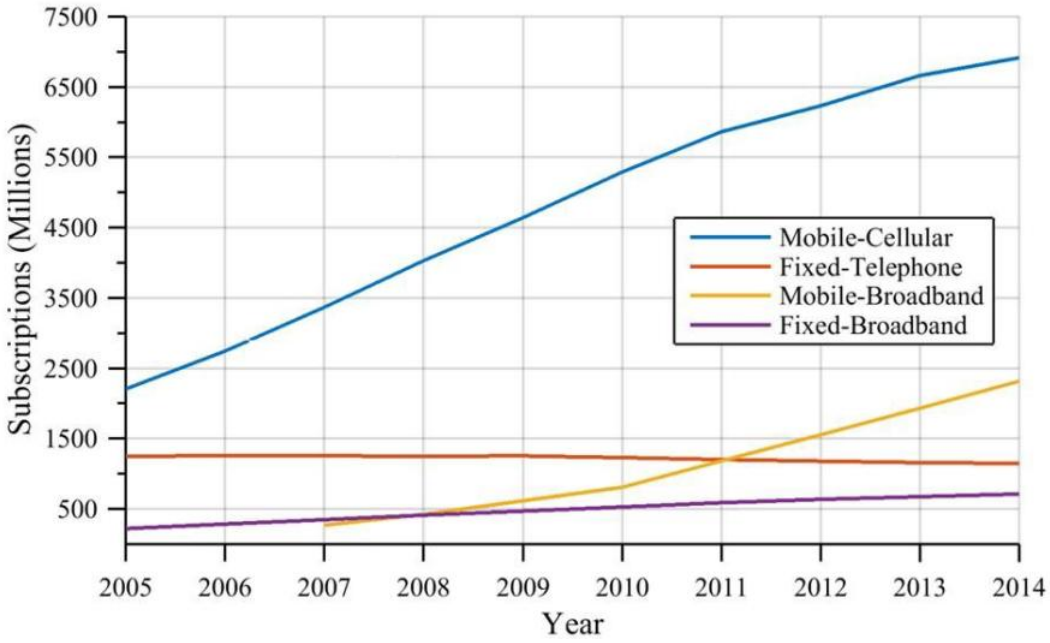

Figure I.1. ITU Statistics showing various types of subscriptions per year

While supporting technology such as high-speed integrated circuits, advanced signal processing and complex coding algorithms have all evolved considerably, the antennas have conventionally been the limiting technology due their direct size correlation to operating frequency. It is important to view the total evolution of wireless communication to understand the growing need for new innovative high performance antennas. This work presents a multiband cost efficient uniplanar antenna structure capable of supporting new generations of wireless communication devices with a physical profile that can easily be integrated into hand-held mobile devices.

B. Evolution of Wireless Communication

The evolution of wireless communication technology can be categorized into consecutive stages known as generations; in which each preceding generation overcomes the limitations of the previous. The first generation (1G) mobile communication devices consisted of analog systems. The 1G systems supported voice only services and no roaming. This technology featured frequency modulation (FM), frequency division duplexing (FDD), and frequency division multiple access (FDMA) methods [3]. The antennas used in these early communication technologies were single band, large whip style monopoles that protruded from the device. First generation wireless systems faced many problems such as low capacity, inconsistent voice quality, cross talk between users, and bulky equipment [4]. The analog technology used in 1G systems severely limited the popularity of mobile communication and restricted the use of this technology to niche markets.

Digital communication advancement's in the 1980's provided a foundation on which a new cellular communication system could take root. The 2G systems relied on digital signal modulation; as opposed to the previous analog modulation, which provided a much higher throughput capacity as well as digital encryption [5]. The combination of consistent voice quality along with the advent of reasonably sized devices opened the door for an expanded market that was attractive to a wide variety of people. Two forms of channel access methods became prominent in second generation wireless systems. Time division multiple access (TDMA) methods allowed multiple users to transmit and receive on the same frequency channel by splitting the signal into individual time slots for each user. Some 2G standards based on this time division method were GSM and PDC [4]. The alternate method was code division multiple access (CDMA) in which users can transmit and receive information across the same channel at

the same time. This is possible when each user has a specific code to which they can modulate and demodulate their transmitted signal. The most common 2G standard based on the code division access scheme was IS-95. 2G technologies brought with it the opportunity for the first true mobile data services such as text messaging, picture messaging, and email. Initial peak data rates of 9.6 kbits/s were common in second generation devices although high data rates were seen later in the evolution of 2G technology [4]. Early second generation cellular phones still featured external single-band whip style monopoles however as the devices began transitioning to alternate shapes such as flip style phones some manufacturer's implemented internally integrated antennas.

As mobile communication technology became more popular and practical worldwide, a strong push for a common international standard arose. The International Telecommunications Union (ITU) defined a new set of specifications for mobile communication known as the International Mobile Telecommunications 2000 (IMT-2000) [6]. Third generation (3G) mobile technology is based on standards that comply with IMT-2000. One commonly marked at 3G technology is the Universal Mobile Telecommunication System (UMTS). This was defined by the Third Generation Partnership Project (3GPP), a global organization that originally set out to define its own 3G system based on updated GSM specifications [4]. Some other technologies that comply with the IMT-2000 or 3G standards are CDMA2000, WiMAX, and EDGE.

Third generation mobile devices provided much higher data rates than previous technologies, while exact data rates were not defined under IMT-2000. Originally peak data rates of 200 kbits/s were observed, however later releases of 3G, such as 3.5 G and 3.75G featured data rates capable of 10 Mbits/s. Smart phones, or phones that have access to the internet became a commodity as 3G technology became faster, cheaper, and more reliable. Third generation

mobile devices featured antennas that were internally integrated. These antennas suddenly had the need to support multiple operating frequencies with higher overall bandwidth, which began required more complex designs and geometries.

In 2008, the ITU published its first set of requirements for fourth generation mobile telecommunication technology in [7]. These were named the International Mobile Telecommunications Advanced standards or IMT-Advanced standards. IMT-Advanced requires a nominal data rate of 100 Mbps while moving, and 1 Gbps data rates while stationary. Several other requirements must be met to qualify as 4G such as: internet protocol (IP) packet switched networks, scalable channel bandwidth, as well as has high quality advanced multimedia support. One fourth generation communication technology is 3GPP's Long Term Evolution (LTE). Similar to how the 3GPP used updated GSM standards to define UTMS, which met IMT-2000 standards, this time the 3GPP set out to update UTMS and called it LTE. Technically the original release of 3GPP LTE was seen as 3G technology however it greatly exceeded IMT-2000 standards and fell just short of meeting IMT-Advanced standards. The true step into 4G was seen with a later revision of LTE. 3GPP's LTE release 10 is commonly known as LTE-Advanced, where the name change only highlights the relation to the IMT-Advanced standards [4]. The antennas used in 4G technologies became exceeding complex, as they have continually needed to support more wideband operating regions to facilitate high data rates, while the overall size has needed to become smaller to fit into the compact devices.

The past four decades have shown the general trend of old mobile communication technology facing major impairments and a new generation taking its place. A brief summary of the evolution of mobile communication technology is made in [8] and outlined with the major antenna styles used for each generation in Table I.1 below.

Table I.1. Overview of Generational Changes in Mobile Communication Technology

Technology	1G	2G	3G	4G
Initial Design	1970	1980	1990	2000
Implementation	1981	1991	2001	2010
Services	Analog voice	Digital voice, SMS	Higher capacity, data rates > 2Mbps	Higher capacity, IP-oriented, multimedia
Data Rates	n/a	14.4kbps	2 Mbps	>200 Mbps
Multiplexing	FDMA	TDMA, CDMA	CDMA	OFDM
Antenna Style	Monopole	Monopole	Monopole, ILA, Meander Line	Monopole, ILA, Meander Line, PIFA, MIMO

C. Long Term Evolution (LTE)

The idea of a Long Term Evolution (LTE) standardization was originally conceived in 2004 as a progression out of 3G and into 4G technology by means of an updating UMTS. The main drivers for LTE focused on increasing data rates, lowering latency, and increasing system capacity [4].

The number of internet based services and applications have rapidly increased in the past two decades. Many mobile devices began supporting internet-based applications and the result became known as mobile broadband. Since the late 1990's, there has been an enormous demand for increased mobile data rates. As mobile technology has progressed from 1G into 4G, the peak data rates have increased from kbits/s to Gbits/s. One goal of LTE standardization was to immediately address this issue and set high standards for mobile device data rates [9]. New mobile services that have become increasing popular such as web browsing, real time gaming, and interactive file transfers require a very low delay to function properly [4]. Previously system latency did not pose much of a problem in mobile communication systems, however this became a key driver in long term evolution standardization. Along with high data rates, and decreased latency, addressing the overall system capacity was an important factor considered. The system

capacity is the total data rate that can be provided on average from each base station site and per hertz of licensed spectrum [4]. As LTE gains popularity and the number of wireless communication users continue to increase as seen in Figure I.1, the spectral efficiency becomes very important.

A key driver in LTE standardization was spectrum flexibility. Frequency spectrum is a very limited resource, and efficient use of spectrum has become a focus in the telecommunication industry. LTE mobile communication devices must support networks across a wide range of allocated frequencies. Since 3GPP's Long Term Evolution is a global standard, there are many regional requirements that had to be satisfied. The goal of LTE was not to create and define and entirely new infrastructure, it was to evolve and globally unify many existing ones. This led to the adoption of a wide range of LTE frequency bands. The LTE spectrum can be split into two main categories based on the duplexing method employed, the first is Frequency Division Duplexing (FDD) and the alternate is Time Division Duplexing (TDD).

Table I.2. FDD LTE Bands

Band	Uplink (MHz)	Downlink (MHz)	Main Regions
1	1920-1980	2110-2170	All
2	1850-1910	1930-1990	NA
3	1710-1785	1805-1880	All
4	1710-1755	2110-2155	NA
5	824-849	869-894	NA
6	830-840	875-885	APAC
7	2500-2570	2620-2690	EMEA
8	880-915	925-960	All
9	1749.9-1784.9	1844.9-1879.9	APAC
10	1710-1770	2110-2170	NA
11	1427.9-1447.9	1475.9-1495.9	Japan
12	699-716	729-746	NA
13	777-787	746-756	NA
14	788-798	758-768	NA
17	704-716	734-746	NA

Table I.2. FDD LTE Bands (Cont.)

Band	Uplink (MHz)	Downlink (MHz)	Main Regions
18	815-830	860-875	Japan
19	830-845	875-890	Japan
20	832-862	791-821	EMEA
21	1447.9-1462.9	1495.9-1510.9	Japan
22	3410-3490	3510-3590	EMEA
23	2000-2020	2180-2200	NA
24	1626.5-1660.5	1525-1559	NA
25	1850-1915	1930-1995	NA
26	814-849	859-894	NA
27	807-824	852-869	NA
28	703-748	758-803	APAC
29	*	717-728	NA
30	2305-2315	2350-2360	NA
31	452.5-457.5	462.5-467.5	CLA
32	*	1452-1496	EMEA
Asia and Pacific (APAC); Europe, Middle East, and Africa (EMEA); North American (NA); Central Latin America (CLA)			

Table I.3. TDD LTE Frequency Bands

Band	Spectrum (MHz)	Main Regions
33	1900-1920	EMEA
34	2010-2025	EMEA
35	1850-1910	NA
36	1930-1990	NA
37	1910-1930	NA
38	2570-2620	EMEA
39	1880-1920	China
40	2300-2400	China
41	2496-2690	All
42	3400-3600	
43	3600-3800	
44	703-803	APAC
Asia and Pacific (APAC); Europe, Middle East, and Africa (EMEA); North American (NA); Central Latin America (CLA)		

The full LTE spectrum consists of many regional and universal bands. The ability to utilize a variety of difference frequency bands provides benefits to the end user and service provider of the LTE network. The more LTE bands a specific mobile communication device can operate on, the more diverse the reception coverage will be. The capability to operate on a variety of frequency bands allows the user to travel outside of regional coverage and still maintain functionality. For example in today's market many cellular phones are only operable in specific regional areas, that is to say if a cellular phone was purchased in the United States, its antenna may be tuned only to work on specific bands supported within US. Taking the device outside of the U.S. to other countries could be problematic if they utilize other areas of spectrum. A device that can operate on many LTE frequency bands is be beneficial to the user, as well as to the manufacturer. Having one design that can be manufactured to operate in all areas of the world would ideally be cost saving for the manufacturer and end user.

As previously mentioned, the ITU-R established the IMT-Advanced requirements that mobile communication devices must meet in order to be considered a fourth generation technology. Release 10 of 3GPP's LTE was setup to meet these standards and become one of the major 4G technologies. Many of the requirements set in IMT-Advanced are high level, which cannot be quantified by performance metrics [10], these can be seen in [11] which include :

- A high degree of commonality of functionality worldwide while retaining the flexibility to support a wide range of services and applications in a cost efficient manner;
- Compatibility of services within IMT and with fixed networks;
- Capability of interworking with other radio access systems;
- High quality mobile devices;
- User equipment suitable for worldwide use;

- Worldwide roaming capability;

Along with the high level requirements, LTE technologies must also meet some requirements not set in IMT-Advanced. LTE-Advanced networks require backward compatibility [12], meaning that LTE-Advanced can be deployed in a spectrum already occupied by LTE with no impact on the existing LTE network. Additionally LTE-Advanced requires spectrum flexibility so that functionality is maintained across areas where regional regulations pose restrictions on specific frequency bands. The IMT-Advanced standards also define a requirement of; enhanced peak data rates to support advanced services and applications (100 Mbits/s for high mobility and 1 Gbit/s for low mobility) [12]. The quantifiable requirements of IMT-Advanced as well as LTE-Advanced shown in [10] are summarized below in Table I.4.

Table I.4. Performance Requirement Comparisons

Metric	Transmission Path	Antenna Configuration	LTE-Advanced	IMT-Advanced
Peak spectrum efficiency (bps/Hz)	DL	8×8	30	15
	UL	4×4	15	6.75
Peak data rate	DL	8×8	1 Gbps	1 Gbps
	UL	4×4	500 Mbps	500 Mbps
Capacity (bps/Hz/cell)	DL	4×2	2.6	2.2
	UL	2×4	2.0	1.4

Multiple-Input Multiple-Output (MIMO) Systems

One of the main drivers of LTE was to support exceedingly high data rates. Many methods to achieve high data rates are employed in LTE technology, which include the use of multiple-input multiple-output antenna systems, along with orthogonal frequency-division multiplexing (OFDM). A MIMO system helps to overcome multipath fading, a major performance impairment of wireless communications systems. In order to recognize the benefits of MIMO, the limitations of a traditional single-input single-output (SISO) system must be

understood. There are a number of factors that limit peak data rates, also known as channel capacity, and some are easier to control than others. The Shannon capacity theorem [13], provides a theoretical prediction of the capacity of an error free channel for a SISO system. When a single channel is corrupted by additive white Gaussian noise (AWGN) the capacity can be expressed as:

$$C = \log_2\left(1 + SNR\right) \tag{I.1}$$

where C is the capacity of the system in bits/s/Hz, and SNR represent the received signal to noise power ratio. One way to increase the system capacity can thus be seen; for every 3dB increase in signal to noise ratio the capacity is increased by an extra bit/s/Hz [13]; However trying to increase capacity by increasing signal received power has practical limitations of using excess power to transmit signals. In reality the capacity of the wireless channels are also subject to random fading which is accounted for in the equation below. Where h is the unit-power complex Gaussian amplitude of the channel [14]:

$$C = \log_2\left(1 + SNR\left|h\right|^2\right) \tag{I.2}$$

In a MIMO system where there are N number of transmit antennas and M number of receiving antennas, the wireless channel can now be written as an $M \times N$ matrix with random independent elements; expressed as $\boldsymbol{H}$. Now the capacity of the channel without any prior transmit information becomes [13]:

$$C = \log_2\left(\det\left(\boldsymbol{I}_M + \frac{SNR}{N}\boldsymbol{H}\boldsymbol{H}^*\right)\right) \tag{I.3}$$

where SNR now represents the average signal to noise ratio of the receiving antennas. Since the capacity is a random quantity, it is useful to calculate the cumulative distribution function (CDF)

rather than any instantaneous values. Considering the average capacity C_a when $M=N$ the previous expression can be simplified to:

$$C_a \approx N \log_2\left(1 + {SNR}/{N}\right) \tag{I.4}$$

The benefits of implementing a MIMO system can be clearly seen from this ideal case compared to the SISO model in Eq. I.1. The capacity can be increased by deploying more than one antenna element since the MIMO channel is subsequently split into N virtual parallel channels.

One key to achieving high channel capacity or high data rates, is to have channel diversity. Channel diversity can come in the time domain by repetition, in the frequency domain by using multiple bands, or in the spatial domain by deploying multiple antennas [15]. MIMO systems utilize what was traditionally a major impairment of wireless communications systems, multipath fading, to their advantage. Multipath fading is the phenomenon that occurs when a receiver sees multiple copies of a transmitted signal. Since the transmitted signal reflects and transmits around and through various obstacles before reaching the receiver, the final received signal is a superposition of the transmitted signal that may contain components out of phase with one another causing significant attenuation in the total received signal. In a SISO system, multipath fading leads to a higher error probability in received data which reduces the capacity, whereas a diverse MIMO system can decode these signals leading to a higher probability and capacity.

D. Other Wireless Networks

Wireless Local Area Networks

Developed alongside mobile communication systems were Wireless Local Access Networks (WLAN). The Institute of Electrical and Electronic Engineers (IEEE) defined the WLAN standards in IEEE 802.11. Wireless local area networks provide a method for any

wireless device to connect via modems to the internet. The high speed internet access of WLAN was quickly integrated into mobile technology. Mobile communication devices utilize WLAN to gain faster, and cheaper internet access, bypassing their main cellular communication service provider. WLAN is often used synonymously with Wireless Fidelity (Wi-Fi), however the Wireless Fidelity Alliance (Wi-Fi Alliance) labels devices as, Wi-Fi enabled, only after certification against the IEEE 802.11 standards have met.

There are many released protocols within IEEE 802.11 that specifically define operating parameters, however it is typical for wireless local area networks to operate on 2.4, 3.6, 5 and 60 GHz frequency bands. The specific protocols define the data rates, modulation techniques and bandwidths of a wireless local area network.

Wireless Metropolitan Area Networks

Wireless Metropolitan Area Networks (WMAN) are series of wireless broadband standards defined by IEEE in the IEEE 802.16. The standard was developed to provide a high bandwidth alternative to cable and DSL [16]. Worldwide Interoperability for Microwave Access (WiMAX) is the official term used for technology that is certified to meet IEEE 802.16 standards. The IEEE originally defined WiMAX in the IEEE 802.16 standard, which limited WiMAX to stationary access points. The IEEE 802.16 was later revised to 802.16e that specifies portable mobile broadband connectivity later termed Mobile WiMAX. WiMAX along with LTE-Advanced were the first two technologies to be considered in the original release of IMT-Advanced [4].

Wireless metropolitan area networks can provide up to 30 miles of line of site coverage, a much larger range compared to local area networks [17]. The most common frequency bands utilized by WMAN include 2.3 GHz, 2.5 GHz, 3.5 GHz, and 5.8 GHz.

E. Antenna Characterization and Performance Metrics

There are several standard metrics used to characterize the performance of an antenna. No single parameter can sum up the behavior of an antenna thus many different measurements are used to better understand the antennas overall behavior and response. Typically the first metric viewed deals with how well the antenna accepts power. In a single port system the scattering parameter S_{11} is called the reflection coefficient. The reflection coefficient is a representation of the ratio of reflected power to supplied incident power. Alternatively, the measurement of accepted power to incident power is known as return loss. The reflection coefficient and return loss represent the same metric; they are equivalent in magnitude but opposite in sign. This can be easily understood by examining a classic transmission line model.

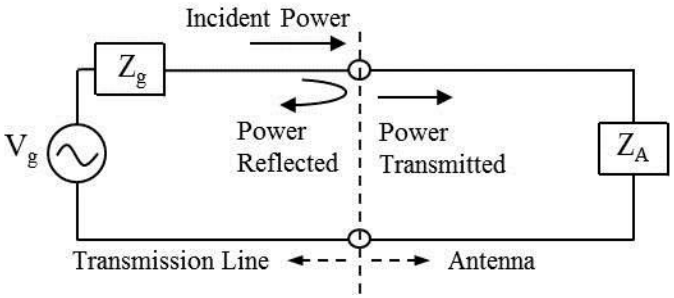

Figure I.2. Simple transmission line and antenna model [18]

Reflection coefficient [19] $$S_{11}(dB) = 10\log_{10}\frac{P_{ref}}{P_{inc}} = 20\log_{10}\left|\frac{Z_A - Z_G}{Z_A + Z_G}\right| \quad \text{(I.5)}$$

Return loss [19] $$RL(dB) = 10\log_{10}\frac{P_{inc}}{P_{ref}} = -20\log_{10}\left|\frac{Z_A - Z_G}{Z_A + Z_G}\right| \quad \text{(I.6)}$$

The reflection coefficient is normally given in a decibel ratio. The smaller the value of the reflection coefficient the more power the antenna is accepting. A large reflection coefficient corresponds to poor impedance matching at the input terminal as seen from Eq. I.5-6. In most cases, coaxial and microstrip transmission lines feeding the antenna have an impedance of 50 Ω.

In order to obtain maximum power transfer between the antenna and line, the characteristic impedance of each must match. Both the antenna input impedance and return loss can be valuable and relate how efficiently the antenna accepts the supplied power. It is important to note that since the impedance is a function of frequency, the return loss also varies with frequency thus these values are usually plotted over a range of frequencies.

Other than the return loss and impedance input parameters, radiation patterns represent another metric used to characterize the behavior of an antennas. A radiation pattern is a three dimensional representation of the normalized power measured across an imaginary spherical surface in the antennas far field. The far field is defined as the region surrounding an antenna where the angular field distribution is essentially independent of the distance away from the antenna [18]. The far field can be described in the following equation:

$$R > 2D^2/\lambda \tag{I.7}$$

Where R is the distance away from the antenna, D is the largest dimension across the antenna structure, and λ is the operating wavelength. An example of a simple dipole far field radiation pattern is shown below.

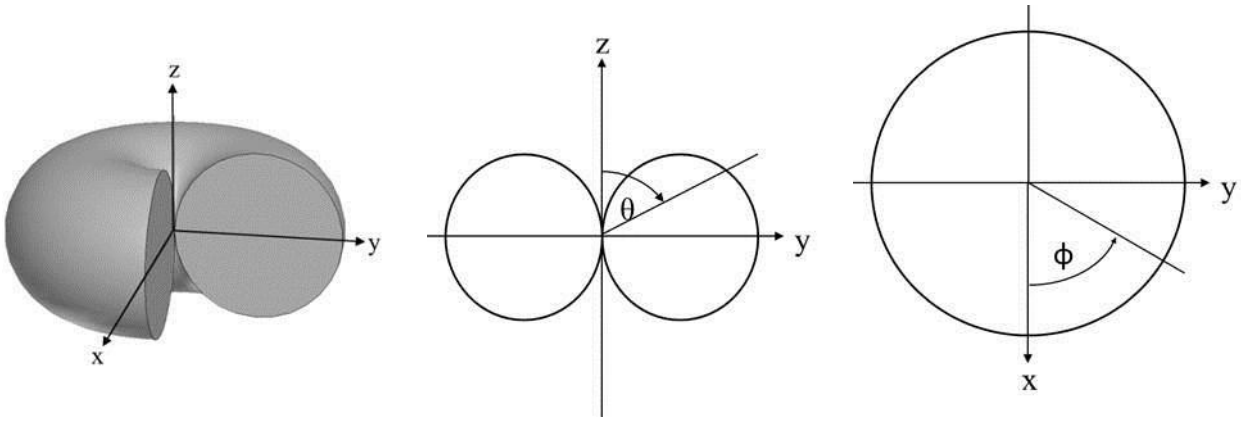

(*a*) 3D radiation pattern (*b*) ZY radiation pattern cross section sweeping θ (*c*) XY radiation pattern cross section sweeping ϕ

Figure I.3 Radiation pattern and cross sections [18]

In many cases the full three dimensional radiation pattern is difficult to measure, however several cross sections of the pattern give good indication of the overall behavior. The cross sectioned patterns show how the power is distributed, for example in Figure I.3(*c*) the pattern is omnidirectional, that is in the X-Y cross section the power distribution is uniform. Some antennas are designed to be omnidirectional as in the case of mobile communication devices, whereas other applications need highly directional antennas.

Another quantitative description of an antenna is the radiation efficiency. The radiation efficiency is a ratio of the radiated power to input power [18].

$$e_r = \frac{P_{rad}}{P_{in}} \tag{I.8}$$

This is an important metric to consider because even when an antenna shows good return loss and is accepting power, that does not necessarily correlate to the amount of power radiated. For example, a 50 Ω resistor would exhibit an extremely low reflection coefficient due to its impedance match with the transmission line, however the radiation efficiency would be nearly 0 because it is dissipating the power in the form of heat rather than electromagnetic radiation. Losses in an antenna generally arise from two sources, dielectric losses and conduction losses.

Another performance characteristic commonly measured is the gain. An antennas gain is a representation of how much energy is concentrated in a specific direction with respect to the average energy radiated in all directions [19].

$$G(\theta,\phi) = \frac{U(\theta,\phi)}{P_{in}/4\pi} \tag{I.9}$$

Where $U(\theta,\phi)$ represents the radiation intensity and P_{in} is the net power accepted by the antenna, thus the denominator represents the isotropic average power across a three dimensional sphere. Since gain is a power ratio it is often expressed in units of dB or dBi, both units are the

same regarding antenna gain. The units dBi are used only to emphasize that the reference power is that of an isotropic radiator. The gain is inherently a function of θ and ϕ as shown in the formula, however often it is beneficial to know the maximum value, which is known as peak gain. The peak gain is useful because it can give a quick indication of an antennas efficiency and directivity when plotted versus frequency.

For any single antenna, the return loss, impedance, radiation patterns, radiation efficiency and gain provide enough information to fully understand the behavior however when considering a MIMO antenna there are additional parameters that should be quantified. Since a MIMO antenna consists of more than one antenna element, each single element should be characterized by the previous metrics in addition to characterizing the diversity between elements.

In the case of a MIMO antenna the scattering parameters provide more information than just the reflection coefficients. In the case of a 2 element MIMO system, S_{11} would be the reflection coefficient of antenna element 1, and S_{22} would be the reflection coefficient of the second antenna element. The scattering parameters S_{21} represents the ratio of power seen at the port of antenna element 2 when antenna element 1 is excited. Alternatively, S_{12} represents the ratio of power seen at the port of antenna element 1 when antenna element 2 is excited. These two scattering parameters represent the isolation between ports in a two element MIMO system. Since MIMO systems need diversity to be effective, a very low isolation coefficient needs to exist in an efficient MIMO antenna.

One metric used to evaluate the diversity of a MIMO system is the envelope correlation coefficient (ECC). The ECC is often used in characterizing MIMO antennas used in mobile communication devices, in which an antenna is said to have diversity when the ECC value is 0.5 or less [20]. The envelope correlation coefficient can be calculated from the following:

$$\rho_e = \frac{\left| \iint_{4\pi} \left(\overline{F}_1(\theta,\phi) \bullet \overline{F}_2(\theta,\phi) \right) d\Omega \right|^2}{\iint_{4\pi} \left| \overline{F}_1(\theta,\phi) \right|^2 d\Omega \iint_{4\pi} \left| \overline{F}_2(\theta,\phi) \right|^2 d\Omega} \tag{I.10}$$

where $\overline{F}_i(\theta,\phi)$ represents the complex field radiation pattern of antenna element i and $\bullet$ represents the Hermitian product [21]. This approach to calculating the ECC is a very labor intensive process since the full three dimensional complex field radiation patterns have to be known and then integrated for each frequency of interest. An alternative approach to calculating the envelope correlation coefficient for MIMO system has been derived in [21] and verified in [22]–[24] which uses the scattering parameters of the antenna system and is shown in the equation below.

$$\rho_e = \frac{\left| S_{11}^* S_{12} + S_{21}^* S_{22} \right|^2}{\left(1 - \left(|S_{11}|^2 + |S_{21}|^2 \right)\right)\left(1 - \left(|S_{22}|^2 + |S_{12}|^2 \right)\right)} \tag{I.11}$$

In a MIMO system two or more antennas are used together to receive a signal and the two replicated received signals are combined in a way to improve the performance of the overall system. The diversity gain is another metric used to characterize the effectiveness of a MIMO system. The diversity gain of a MIMO antenna can be defined as the ratio between the elements combined cumulative distribution function (CDF) and a single element reference at a certain probability level, typically chosen to be 1% [25]. In other words the diversity gain describes the enhancement of the total systems received signal against fading compared to any single element within system.

$$G_{app} = 10\sqrt{1 - \left| 0.99\rho_e \right|^2} \tag{I.12}$$

The apparent diversity gain derived in [26] is shown in Eq. I.12 above. This method uses the envelope correlation coefficient to calculate the apparent diversity gain, where the maximum apparent diversity gain is 10 at a 1% CDF level.

Overall MIMO antennas can be fully characterized by calculating the return loss, radiation patterns, efficiency, and gain of each individual antenna element in addition to the isolation scattering parameters and the ECC or diversity gain. These metrics provide good characterization of the entire MIMO antenna.

F. Types of Antennas Used in Wireless Communication

Inherently as the number of mobile device applications has increased, the antennas supporting them have also increased in complexity. Today's modern cellular phones for example must not only meet the challenging technical demands of mobile communication applications but must also have a large high definition display, built in speakers, long battery life, and be aesthetically pleasing. In addition the device must feature an ergonomic design that can comfortably fit in ones hand while still being slim enough to conceal in a pocket. All of these demands pose unique challenges to design engineers, specifically the main challenges in designing antennas for mobile communication devices are: limited or small size, multiband operation, and the ability to integrate with other device components.

Advanced materials research and evolved manufacturing technology have allowed electrical components to exponentially shrink in size over the past several decades. Although the size of electronic components in mobile devices are continually decreasing following Moore's law, the size of the antennas supporting these devices cannot follow the same trend. Antennas are fundamentally limited not by manufacturing technology but by the underlying physics that govern their operation [19].

Electrically small antennas (ESA's) are antennas that have a size much less than their operating frequency. The antennas incorporated in mobile communication technology are often considered electrically small since they are designed to fit within a volume much smaller than their operating wavelength. Electrically small antennas face a few fundamental tradeoffs that cannot be overcome as shown in [27]. An electrically small antenna's size is always inversely related to its efficiency, bandwidth, and gain. An ESA can be optimized to a fractional wavelength size however the bandwidth would be very narrow and the antenna would suffer from poor efficiency. These fundamental tradeoffs give rise to many diverse and unique solutions for antennas incorporated into mobile communication technology. Ultimately, there are three antenna styles commonly used in mobile communication devices, the monopole, meander line antenna, and planar inverted-F antenna; and in some cases hybrid designs utilize more than one of the main geometric styles.

Monopole Antennas

The monopole antenna has long been used in wireless communication devices. The simple monopole style antenna was implemented dating back to the first generation wireless devices due to the antennas desirable characteristics. Monopole antennas provide omnidirectional radiation patterns which is preferred in the telecommunication industry. Having a non-directional radiation pattern allows the device to properly send and receive signals at nearly any orientation. Other benefits of monopole style antennas include having an impedance that can easily be matched giving low losses and high overall efficiency.

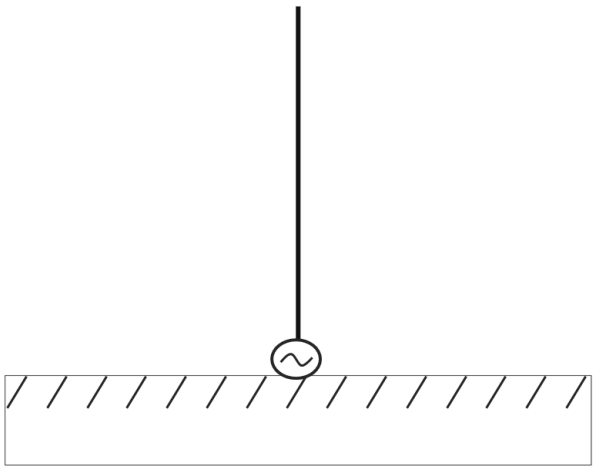

(*a*) Simple monopole antenna

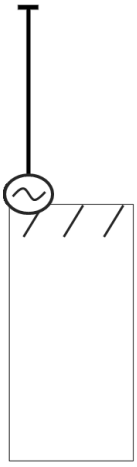

(*b*) Whip monopole antenna used in early generation mobile communication devices [19]

Figure I.4. Monopole antenna examples

Monopole antennas for mobile communication still exist and are commonly used in devices today. Although external whip antennas are no longer seen in mobile communication devices, the operating characteristics of monopole antennas pose so many advantages the general style of antenna is still used. Many internal monopoles designed for LTE operation have been developed [28]–[37].

One of the main problems monopole antennas face is the overall size of the radiating element as well as the size of the finite ground plane. Some monopole antenna designs feature very wide bandwidth which covers nearly all of the LTE spectrum, however they are simply too large or feature unusual geometries that are not practical to use in mobile communication devices such as cellar phones [28]–[30], [38]. The extra size requirements posed by these antennas make them suitable for applications such as PC's, laptops, and tablets but they are not a viable solution for smaller handheld devices. Alternatively small monopole antennas, acceptable for all sized mobile communication devices have been presented in [31]. The smaller size of these antennas provides a more reasonable solution for 4G LTE devices however the reduced size comes with the tradeoff of decreased bandwidth. These small monopole antennas are severely limited in the

number of frequency bands they can cover and are difficult to optimize at the lower LTE frequency spectrum. Nevaro-Mendez *et al.* attempted to maintain a wide bandwidth while reducing size by implementing some special monopole geometries such as a Vivaldi structure in [32], which featured an operational bandwidth of nearly 200% however; overall the size limitations still posed problems. Work by Lizza and Messa explored the use of fractal monopoles in [33]. The fractal design showed a 24% size reduction compared to a standard quarter wavelength monopole, however the antenna was limited by narrow bandwidth, only covering 2 LTE operating bands.

Other common techniques to enhance the performance of monopole antennas include introducing lumped circuit elements into the radiating path of the antenna [30],[34]. The addition of inductors and capacitors allow monopole antennas to obtain a better impedance match and thus increases the bandwidth. The tradeoff to this approach is that the circuit elements require additional height to the overall design. Also the components must be soldered onto the antenna which decreases the durability of the design as well as introduces new potential sources for error in a final product.

Simulation results of parasitic elements on the ground plane were presented by Augustin *et al.* and give additional operating bandwidth to a monopole style antenna shown in [35]. This antenna had excellent performance throughout all major LTE bands as well as compact size however it failed to address much of the WLAN and WMAN spectrum and neither fabrication or measurements were performed. Guo *et al.* shows a combination of antenna broadbanding techniques in [36]. The proposed monopole hybrid antenna featured a long parasitic shorted strip in addition to an altered ground plane to help improve LTE lowband performance, the measured antenna observed 6-dB return loss or better from 691-956 MHz and 1554-2730 MHz. A novel

monopole design by Xiao *et al.* in [39] also features a long parasitic element. The proposed monopole antenna incorporated a three dimensional geometry as well as a surface mounted capacitor and inductor which gave a large midband operating region from 1450-3000 MHz. The main concern of this design is the additional height of the radiating structure as well as the lumped components that could be impractical in a mobile communication device that is very thin.

Meander Line Antennas

Meander line antennas are a variation of monopole that is folded several times into a specific pattern. A typical meander line antenna is shown in Figure I.5. Similar to monopoles, they exhibit a non-directional radiation pattern and also suffer from narrow bandwidths.

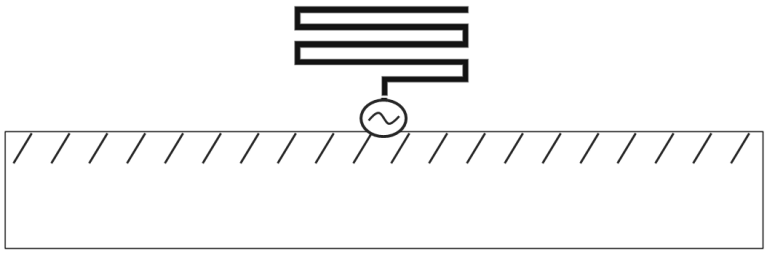

Figure I.5. Meander line antenna

Numerous meander line antennas have been explored for use in mobile communication devices [40]–[47], since they offer similar operating characteristics to the monopole antenna with a smaller footprint. While the meander line antennas inherently occupy less space than the monopole, they still must overcome the natural narrow bandwidth behavior to be practically considered for use in communication devices. Meander line antennas that cover only single LTE/WLAN have been studied [40], [41]. Additionally dual band meander line styles have been explored in [42]–[44]. Several techniques have been presented to increase bandwidth such as adding a conductor line to the end of the meander line antenna [45]. One way to improve the impedance match of the meander line antenna is to alter the shape of the ground plane on the

reverse side of the antenna, as studied in [47] by cutting slots with various lengths and widths. Work presented by Sultan *et al.* combines the conductor line technique with etched slots and electromagnetic bandgap (EBG) structures to provide a multiband antenna with greater than 6-dB return loss across many of the major LTE bands [48].

Planar Inverted-F Antennas

Planar inverted-F antennas (PIFA) evolved from the simple monopole antenna. As the frequency spectrum began expanding during the evolution of mobile communication, the quarter wave monopole featured in first and second generation mobile communication systems became less practical. Although the monopole still had desirable performance traits such as omnidirectional coverage, and good impedance matching; it became excessively tall at lower frequency bands such as 700-1000 MHz. The solution was to bend the monopole over to decrease the height as shown in Figure I.6(*a*). The inverted-L antenna (ILA) provided the uniform radiation characteristics like that of the monopole in addition to a low profile. One disadvantage of the ILA design is that as the antenna along with the overall devices became smaller the antenna turns highly capacitive causing impedance matching problems [19].

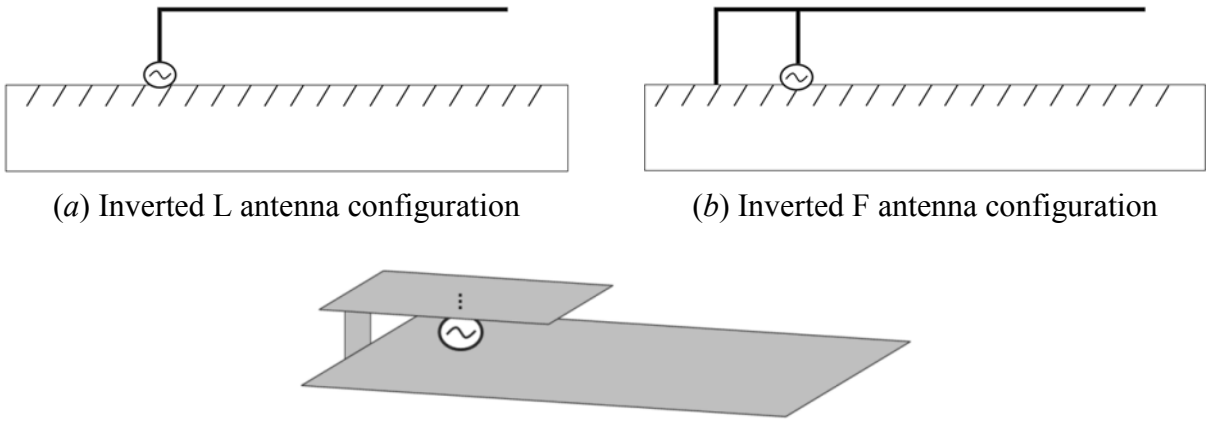

(*a*) Inverted L antenna configuration (*b*) Inverted F antenna configuration

(*c*) Planar inverted-F antenna

Figure I.6. Evolution of monopole antennas [19]

To overcome the capacitive reactance of the ILA and help improve bandwidth a small shorted section can be added. The addition of the shorted piece helps overcome some of the limitations of the ILA, the new geometry is then called an inverted-F antenna (IFA). The IFA allows wider bandwidth and easier impedance matching since there are now more design parameters to work with. Substituting linear wires for planar patches is a common technique used for many types of antennas in order to increase bandwidth. Taking an IFA and applying this technique gives rise the planar inverted-F antenna (PIFA). The PIFA is inherently an evolution of the ILA however it can also be thought of as an abstract quarter wave patch antenna with shorted plate. This is a common design in mobile cellular technology. Many PIFA style antennas have been proposed for use in mobile communication systems [49]–[55].

Traditional PIFA's can provide sufficient coverage for various single LTE frequency bands as well WLAN and WMAN bands [49], [50]. The limitation of the simple PIFA style is once again the large bandwidth requirements of the LTE spectrum, which cannot be easily met by a single PIFA. There have been a variety of methods proposed in the literature to help overcome these bandwidth limitations. One such technique explored by Kang and Wong in [51] implemented multiple ground planes in a clam shell style phone to achieve wide bandwidth. The dual ground plane design featured two operating regions 750-1040 MHz and 1580-2790 MHz however as mobile phone designs transitioned away from calm shell styles, the implementation of this technique became impractical. Lee and Sung presented work in [52] that featured a PIFA with parasitic strip lines and PIN diode which provided an alternate and tunable method to increase bandwidth of the PIFA style antenna. Using a DC bias to turn on the PIN diode, the PIFA antenna showed a region centered at 2200 MHz experienced a 46% increase in bandwidth. A planar inverted F antenna proposed in [53] used a small coupling branch to excite the antenna,

which provided improved low frequency return loss, however the higher frequency LTE bands were not addressed. Naturally, common impedance matching methods, such as adding circuit elements that were explored for use in monopoles and meander lines, were also seen in PIFA designs [54], [55].

Multiple-Input Multiple-Output (MIMO) Antennas

As previously mentioned, using more than one antenna together in a system allows diversity to be created which manifests in higher data rates and more efficient network coverage. MIMO antennas in mobile communication devices can achieve diversity in various ways. Spatial diversity can be achieved by keeping the distance between two elements as far as possible, polarization diversity occurs when two or more antennas are oriented orthogonally to one another, additionally pattern diversity is when each antenna element features a unique radiation pattern. Single antennas designed for mobile communication devices already face the challenging task of multiband operation within strict size limitations. Introducing a MIMO antenna in a mobile device adds even more complexity to the overall design. The size limitations imposed on mobile devices provide the biggest problem to MIMO antennas due to the near field coupling effects that the antennas have on one another. Multiple closely spaced antennas operating on the same ground plane will have a significant effect on the diversity of the system; any correlation between antennas will reduce the overall system capacity [56]. Without diversity, a MIMO antenna will not provide any benefit over a single element antenna.

The advantages of utilizing MIMO antennas in mobile communication devices greatly outweigh the challenges faced by system designers. The literature shows a variety of styles and diversity enhancement techniques aimed at MIMO antennas for mobile communication devices [57]–[74]. Electrically small MIMO antennas designed for mobile communication devices often

consist of antenna elements that are common in mobile devices such as the monopole and bent monopole style [57]–[61], meander line style [62]–[64], and PIFA style [65]–[67]. The challenge is implementing the MIMO antenna elements in efficient ways as to minimize the correlation between elements.

Antenna element placement within a MIMO system provides a simple means to improve diversity between elements. Consideration to not only the physical separation of antennas but also the radiation pattern overlaps and polarizations of the elements all become important in locating the best position and orientation of the antenna elements. Figure I.7 below shows an example of a MIMO system composed of two meander line style elements on a common ground plane, in which the element spacing and radiation pattern diversity can be observed.

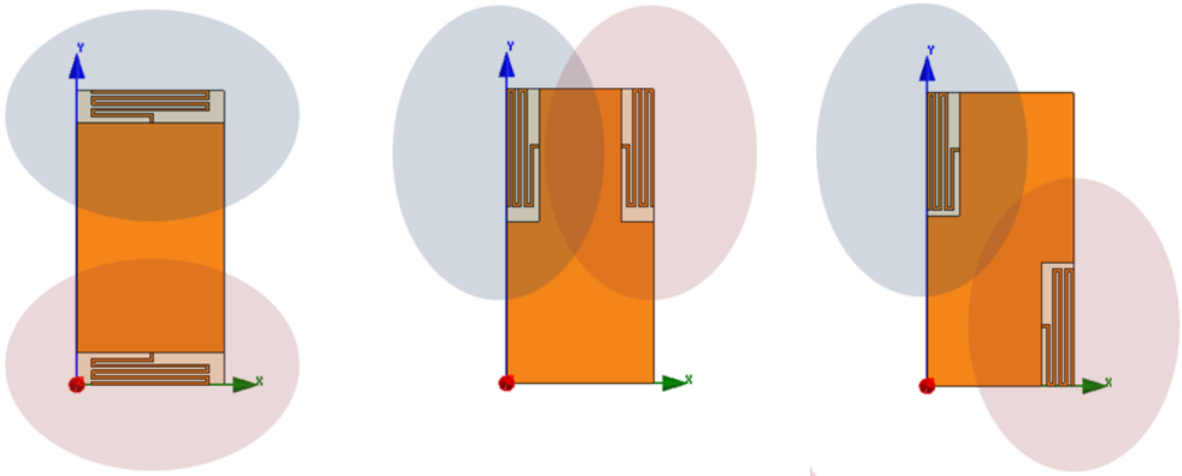

(*a*) Elements mirrored x-axis (*b*) Elements mirrored y-axis (*c*) Elements mirrored x and y-axis

Figure I.7. Several MIMO configurations showing element and pattern variation

A variety of approaches have been proposed to help reduce the correlation between elements in MIMO antennas. Electromagnetic bandgap structures (EBGs) can help provide some isolation between antennas as shown in [65], [68], [75]. The EBG structures placed on the ground plane between two MIMO elements act as band-stop filters; effectively isolating the

ground plane surface currents between ports. EGB structures have shown to enhance isolation by as much as 8 dB in [69], however ultimately their resonant nature causes bandwidth limitations that cannot cover the most of the LTE, WLAN, and WMAN spectrum. While EBG structures act as band-stop filters on the ground plane, other techniques to improve diversity involve manipulations to the ground plane as well. Introducing slots and notches in the ground planes of MIMO antennas can improve isolation between elements by disturbing surface currents along the ground plane; examples of this method are further explored by groups in [57], [58], [62], [66], [70]. Srinivas *et al.* utilizes scattering ground plane slots to improve isolation of a MIMO antenna by over 7.5 dB from 1 GHz. 4GH in [57], corresponding to a decreased ECC of 0.75 to 0.27. Overall the literature showed utilizing defected ground planes provided a more practical solution for improving isolation over the EBG ground planes, since the defected ground planes are not a subject to a specific resonant mode operation.

Other methods used to improve diversity within MIMO systems include using decoupling networks [71]–[74]. The decoupled networks presented in [71]–[73] introduced shorted components and some microstrip line elements that created additional current paths effectively reducing the undesirable induced ground currents. Other than using microstrip line elements, work presented by Kim *et al.* featured a lumped element decoupled network for a dual band MIMO antenna [74]. A surface mount inductor helped to improve isolation between the PIFA elements by nearly 10 dB and the simulations resulted in an ECC less than 0.1; however the decoupled network was designed for only dual band operation. Implementing a similar style over multiple operating regions would become extremely challenging, requiring excessive lumped components and physical space on the antenna.

G. Discussion of Thesis Goals

In conclusion the literature shows numerous styles and techniques for designing antennas suitable for some mobile communication devices. Many of the single antenna designs featured acceptable 6-dB return loss covering the major LTE, WLAN, or WMAN spectrum with a variety of bandwidth enhancement methods utilized. However; as communication standards continue to globalize and the number of mobile communication users increases, the need for an extremely multiband MIMO antenna that can support much of the LTE spectrum as well as WLAN and WMAN bands is needed. The research presented in this thesis looks to address the shortfalls of the aforementioned single and MIMO antenna designs. The MIMO antenna presented in this thesis was designed to address the following goals:

- Efficiently exploit as much LTE spectrum as possible in addition to covering the major WLAN and WMAN bands;
- Implement an overall practical size and shape to allow easy integration with current mobile communication technology;
- Maintain geometries that can be processed by simple fabrication techniques;
- Utilize common materials and components to minimize costs;

The first goal listed to efficiently exploit as much of the LTE spectrum as possible while also covering the major WLAN and WWAN bands was the key driver of this research. Since it would not be practical to try and design a MIMO antenna to cover all the wireless communication spectrum, the goal then was to efficiently operate on as much as possible. This includes not only meeting the 6-dB return loss requirement but to exceed it; while also exhibiting omnidirectional radiation patterns, and high radiation efficiency across the spectrum. Additionally since the MIMO antenna was designed for mobile devices; a goal was set to limit

the total size of the antenna. The final antenna must have a size compatible with current mobile technology so that it can be easily integrated into future devices. The last two goals of the antenna design are to ensure that it can be practically manufactured and implemented. By using cost effective materials and fabrication techniques the antenna gains practical value. The following chapters of this thesis present the antenna design methodology, simulation results, fabrication techniques, and final characterization measurements of the device.

II. Antenna Design and Simulation

The process of designing a MIMO antenna for mobile communication technology can be separated into individual steps. This simplifies the process; reducing design time and excessive computational burdens. By first designing a single antenna optimized for LTE operation, the approach remains similar to traditional antenna design and the computational requirements remain minimal compared with a two port MIMO antenna system. From a single antenna design, a two element MIMO system can be created by coping the design onto a different area of ground plane and then optimizing to achieve maximum isolation between the two. The approach taken for LTE MIMO antenna presented in this thesis was to first optimize a single antenna, followed by the implementation of a duplicate on the same structure. This chapter outlines the design steps taken and simulation results for both a single antenna and a two element MIMO antenna.

A. Computational Methodology

The computational results shown in this thesis were simulated using ANSOFT HFSS™; a commercially available computational electromagnetics software based on the finite element method. The finite element method utilized by HFSS™ is a frequency domain, volumetric discretization approach to solving complex electromagnetic problems. As with any computational electromagnetic problem, the accuracy of results produced are extremely sensitive to many externally set parameters. The analysis of all FEM based problems consist of four main steps shown below [76]:

- Discretize the domain into a finite number of elements
- Derive of the governing equations for each element
- Assemble the elements within the computational domain
- Solve the system of equations for a solution region.

HFSS™ follows these same basic steps during computational analysis of a model and begins by discretizing the domain into individual elements in a process called meshing. The software featured an adaptive meshing process that aimed to eliminate any substantial error due to inaccurate meshing. Specifically HFSS™ meshes and then solves the entire domain; followed by a repeated process that takes the original elements and splits them into even smaller pieces, effectively increasing overall number of elements. Upon resolving inside the domain, an error factor can be observed that shows the difference in total energy between the first mesh and the second. The process is then repeated until the error is very small, indicating that the mesh size is small enough that any reduction in size will not significantly affect the solution. This becomes important because as the number of individual elements increases with each mesh, the computational complexity increases and the overall time and memory requirements to solve increase. Understanding the tradeoffs between accuracy of a solution and time and memory requirements to solve is an important concern.

Once the domain is discretized into elements, HFSS™ then defines the governing equations for typical elements, that is elements not touching a boundary or excitation. The equations used are the derivative forms of Maxwell's equations. When defining an excitation, the elements touching the source also are subject to follow Maxwell's equations, however these special elements have initial values that are constant based on the setup of excitation parameters. In addition to the excited elements, the elements along boundaries also have special considerations that are subject to the parameters defined. Some examples of boundaries include perfect electric conductors, perfectly matched layer, impedance boundaries, and radiation boundaries. The boundary conditions have significant impact on the solution.

Once the excitation and boundary conditions have been set, the next step in the process is to assemble the elements into a large system of equations and then solve the system throughout the domain. The final result is a solution to Maxwell's equations for each single element within the domain, based on this the overall behavior of the domain and the behavior of any component within it can be seen.

Model Domain

The model domain implemented in HFSS™ for the simulation results shown in this thesis consist of an air box, surrounded by a perfectly matched layer. All antenna models are placed in the center of the air box that extends a quarter wavelength from each antenna structure edge as seen in Figure II.1.

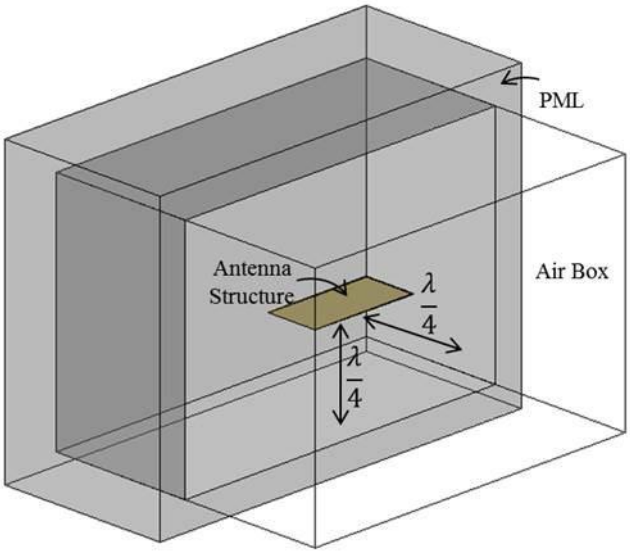

Figure II.1. Simulated model domain setup

700 MHz was considered as the lowest frequency of interest (LTE band 12), however a 600 MHz wavelength was used to determine the size of the air box to ensure accurate solutions even below 700 MHz. The corresponding quarter wavelength was approximately 150 mm.

Within HFSS™ the external air box boundaries were defined as perfectly matched layers (PML). A PML boundary is a boundary condition such that the impedance seen on both sides of the boundary are perfectly matched. These boundaries set up a condition that replicates free space. When any electromagnetic wave encounters the edge of the air box, all of the energy is transferred into the region and none is reflected back into the computational domain. This allows the entire domain to replicate a solution solved in infinite free space, which otherwise is not computationally possible. The power of the wave incident to the PML can then be transformed to the far field and useful results such as radiation patterns, total radiated power, and radiation efficiency can be obtained.

Apart from the boundary conditions, another critical component of the computational domain is the excitation. There are many ways to excite a model within HFSS™ which include plane waves, wave ports, lumped ports, and terminal ports. The various excitations each have advantages and limitations, and it is important to know the practical behavior of each. Since the proposed antenna model will be fabricated and fed via a coaxial cable, the best choice of excitation is a lumped port. A lumped port allows a modal excitation of a known impedance. It represents an infinitely long transmission line feed and can be placed anywhere within the computational domain. Setting the lumped port excitation's characteristic impedance to 50 Ohms will replicate a coaxial cable fed. HFSS™ will excite the model across the lumped port and the solution will consist of not only field data within the domain, but also modal data such as input impedance and scattering parameters.

B. Single Antenna Design

Before computational simulation began to take place, many physical parameters and limitations were considered with respect to the final goals that were set. Keeping the simulation,

fabrication, and measurement processes all in mind during the initial design process helped to avoid potential problems. The first task in the antenna design process was to review the literature of previous LTE antenna designs and to gather all of the required parameters. The design flow began by taking into consideration all of the physical constraints; for mobile LTE operation the antenna must physically be small enough to fit within a mobile device such as a cell phone or tablet. This gave initial size constraints to work with.

The average size of some recently released mobile phones such as the Apple Iphone6 and the Galaxy S6 is approximately 140×70×6.6 mm. This size includes touch displays, front and side panel buttons, battery, as well in internal circuity. Antennas within LTE devices are integrated into the printed circuit board of the device, they do not act as standalone components. Considering this, the antenna design must not only be small enough to fit within the physical constraints of the device but must have radiating elements that take up a minimal amount of space so that it can be easily incorporated into the full system design. The first parameter then set is the physical size limits of the antenna. The practical starting point was a total size 115×55×1.54 mm with the radiating element consuming a 15×55×1.54 mm section of the top. This total size would fit easily within the outer casing of the device as well as allow room along the side for additional features since the initial size limits are already smaller than the average size of mobile communication devices. The 1.54 mm thickness was selected not only due to the size restrictions of mobile technology but also because this represents a standard size thickness of printed circuit board material. This size would be easily attainable from a variety of manufactures at a low cost. Additionally 1.54 mm thick FR4 is suitable for milling fabrication.

Once the overall dimensions were set, the supporting substrate material was selected. Again, considering the goal of cost efficiency, an FR4 material was chosen. FR4 is a fiber-glass

composite laminated with an epoxy resin. It is one of the most common and cheapest printed circuit board materials used in industry. FR4 has relatively stable electrical properties across the LTE operating frequencies however exact specifications are not standardized and can vary between process batches and suppliers. The cheap cost and high availability of FR4 outweigh the potential challenges that come with slight uncertainty in the electrical behavior across the LTE spectrum.

With the size and material selected, the next initial consideration was determining the style of antenna to utilize. Ideally an antenna for mobile devices could operating on all LTE, WLAN, and WMAN frequency bands, and as shown previously in Table I.2-3 there are 42 separate bands ranging from 450-3800 MHz. A frequency independent antenna such as a spiral could easily be designed to cover this full spectrum, however based on the bandwidth required, a spiral antenna covering this spectrum would be over 1.5 m in diameter. The review of the literature showed that electrically small antennas for mobile communication devices were mainly limited to monopoles, meander lines, and PIFAs; and many optimization techniques and design variations can be implemented to meet the specific goals. The decided antenna design featured a combination of monopoles and meander lines due to their uniplanar nature which can easily be fabricated and utilizes only a two dimensional geometry thus maximizing the antennas volume. For similar reasons PIFA styles antennas were avoided since they require additional height to implement and the fabrication can be more complicated.

A summary of the initial design parameters can be seen in Table II.1. Using these parameters as initial conditions, a computational model was then setup in order to begin the antenna design and optimization process.

Table II.1. Initial Design Parameter Summary

Parameter		Design
Overall Dimensions		115mm×55mm×1.54mm
Radiating Element Dimensions		15mm×55mm×1.54mm
Material		FR4
	Relative Permittivity	4.2
	Dielectric Loss Tangent	0.02
	Relative Permeability	1
Antenna Style		Monopole/Meander Line

Model 1

The first design step in creating the multiband uniplanar LTE antenna was to implement a direct fed bent monopole or ILA. This step is critical to the overall design since this element will be the only direct fed component of the antenna. It must act as a radiating element as well as a coupling device that will be able to support additional radiating elements to be added in later design steps. Using a direct fed component to couple feed other antenna elements is a broadbanding technique shown by Guo *et al.* in [36], which featured a direct fed IFA coupled to other elements in a single LTE antenna design. The direct fed ILA component had a total length of 49 mm with a vertical component length of 9 mm. The width of the ILA was 0.6 mm and the feed gap between the radiating element and the ground plane was 1.0 mm which allowed room for a coaxial line to be soldered in later phases of fabrication. The overall configuration can be seen in Figure II.2 which depicts the top view and an isometric view of the simulation model.

The simulation model was excited with a 50 Ohm lumped port, which is representative of the behavior and impedance of a coaxial cable. The frequency was swept from 0.5 GHz to 6.5 GHz to observe the characteristics of the antenna across the frequency bands of interest. The return loss and impedance versus frequency are plotted in Figure II.3 and Figure II.4. The direct fed bent monopole with a length of 49 mm and shows operating frequencies of 1.2 GHz, 3.53 GHz and 5.23 GHz, with bandwidths of 320 MHz, 490 MHz and 800 MHz respectively.

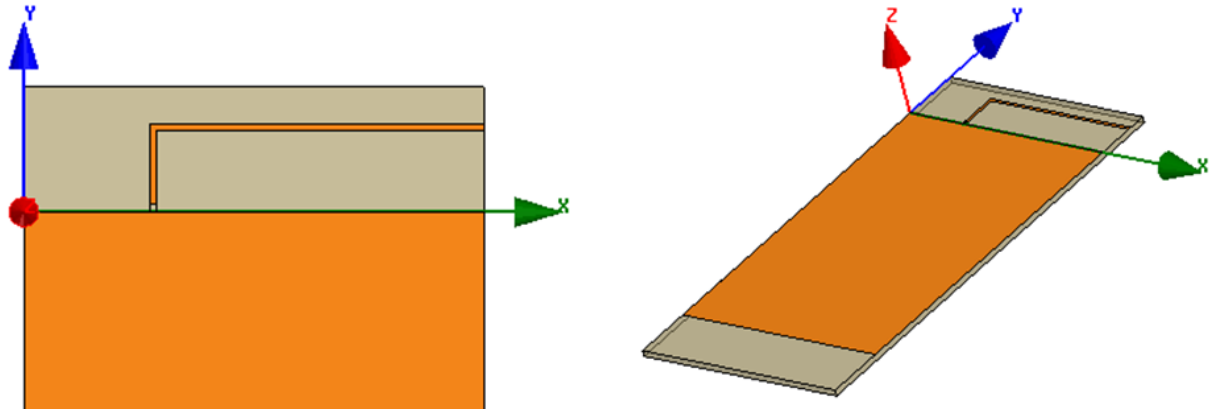

(*a*) Top view of antenna (*b*) Isometric view of antenna

Figure II.2. Antenna model 1

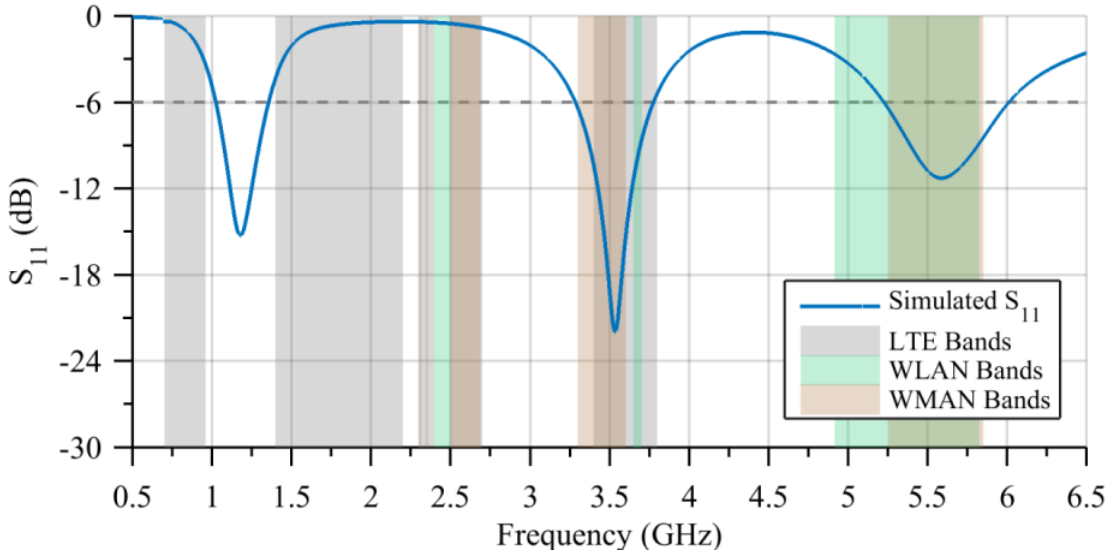

Figure II.3. Return loss versus frequency for antenna model 1

The return loss for this element provided desirable operating characteristics in the higher frequency WLAN and WMAN spectrum. In addition the 3.53 GHz operating mode covers several LTE, WLAN, and WMAN bands. Although the single ILA showed good performance in the upper frequency bands, additional elements will have effects on these resonances. Since additional elements will alter the impedance of the antenna; the design is not optimized at this point, as any optimizations would have to be changed to account for mutual coupling effects later in the design process.

It can be seen that the lowest resonant mode for the ILA offers no additional coverage of the desired frequency bands. This lowband region needs to be adjusted such that it either shifts into the midband LTE spectrum or shifts into the lowband LTE region. One main advantage to the design of the ILA is that the real part of the lowband impedance is already near the desired 50 Ω, as shown in Figure II.4.

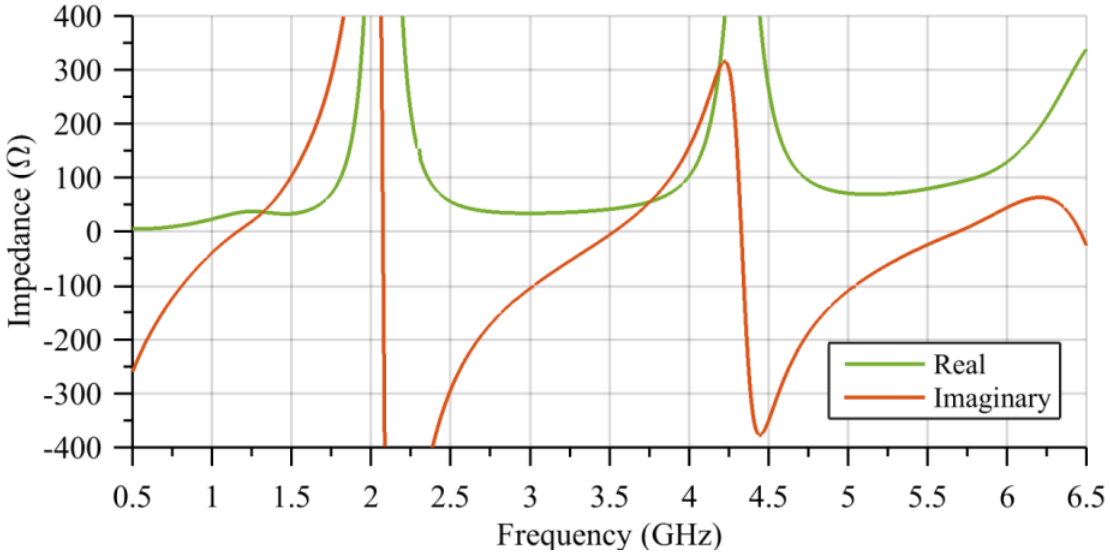

Figure II.4. Input impedance of antenna model 1

The lowband impedance can undergo further adjustment by adding additional coupling or parasitic elements to the antenna. The coupling of additional elements can have a large impact on the imaginary part of the impedance, which can be shifted to nearly 0 Ω in the desired operating range. This will allow the antenna to cover some of the LTE spectrum at the lower frequencies.

Model 2

Additional elements needed to be added to the direct fed ILA which failed to cover any of the lower or middle LTE spectrum. Due to the fundamental limitations and tradeoffs of electrically small antennas, it is clear that the 49 mm ILA could not sufficiently cover any of the lowest LTE bands. In order to address the lower LTE spectrum, a longer antenna element was

added. A 117 mm planar monopole was folded into a C-shape configuration and placed above the original ILA. The orientation of the new antenna can be seen in Figure II.5.

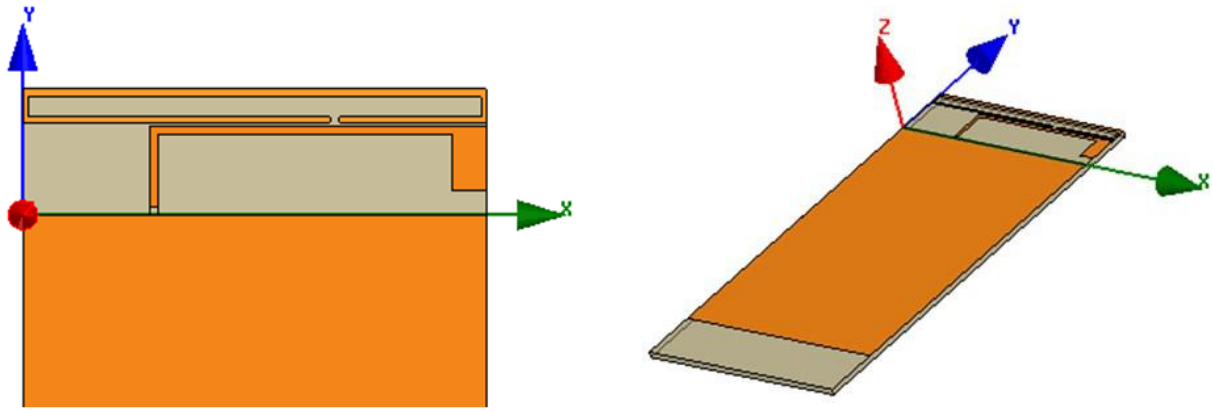

(*a*) Top view of antenna (*b*) Isometric view of antenna

Figure II.5. Antenna model 2

The original direct fed ILA element was also slightly changed from the previous design step. A small patch was added to the end of the ILA which increased the length of the monopole. The new antenna's return loss behaves very differently than the single ILA. The C-shaped monopole features a line width of 0.6mm and a gap between the two ends of 0.5mm. Two key parameters arose when analyzing the coupling between the C-shaped monopole and the direct fed ILA; the position of the gap in relation to the ILA, as well as the separation distance between the two elements. Adjusting either of these parameters fundamentally alters the effect that the new C-shaped monopole has on the entire antenna system.

The 117 mm C-shaped monopole extended the operating range of antenna. The new coupled radiating element shifts the lowest band of operation to 1.01 GHz with a bandwidth of 305 MHz. Additionally this creates another 6-db operating frequency of 2.62 GHz with a bandwidth of 320 MHz which can be seen in Figure II.6. Although the lowest resonant frequency of the C-shaped monopole is very sharp and narrow, it does allow the overall antenna to begin

covering some of the lowband LTE spectrum. The sharp resonance can be seen even more clearly when observing the impedance in Figure II.7.

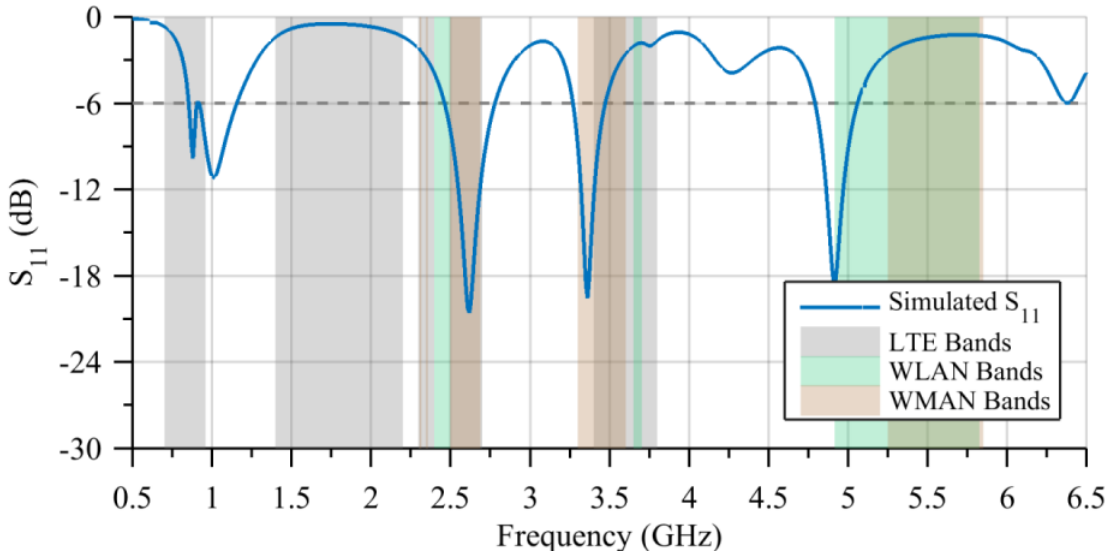

Figure II.6. Return loss versus frequency for antenna model 2

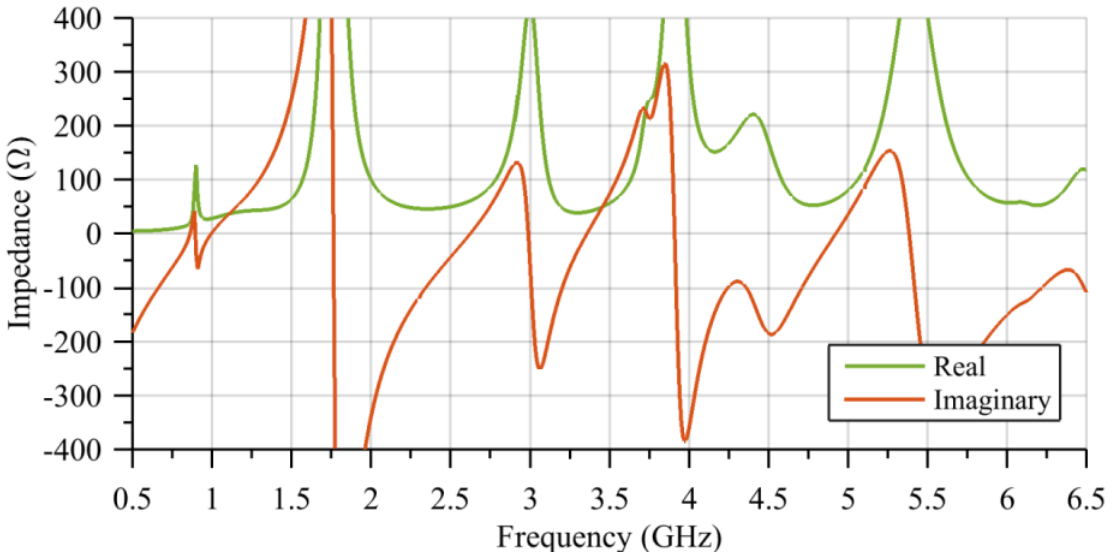

Figure II.7. Input impedance of antenna model 2

Increasing the ILA's effective length shifted the two highest resonant modes to slightly lower frequencies. Coverage of the upper LTE bands as well as the WLAN and WMAN bands decreased during this design step. The decreased high frequency performance of the antenna is

not a concern during the present design step, since the high frequency behavior of the antenna can be easily adjusted by small physical alterations. In contrast, covering the lower frequency bands is much more difficult to design for, due to the limits of electrically small antenna's.

Model 3

Coverage of the midband LTE spectrum is addressed by adding a parasitic element next to the direct fed ILA. Using coupled parasitic elements connected to the ground plane is another broadbanding method that has been effective in the literature [28], [35], [52] .The parasitic element which is connected to the ground plane of the antenna couples to the ILA adding new resonant frequencies, and altering the impedance of the antenna

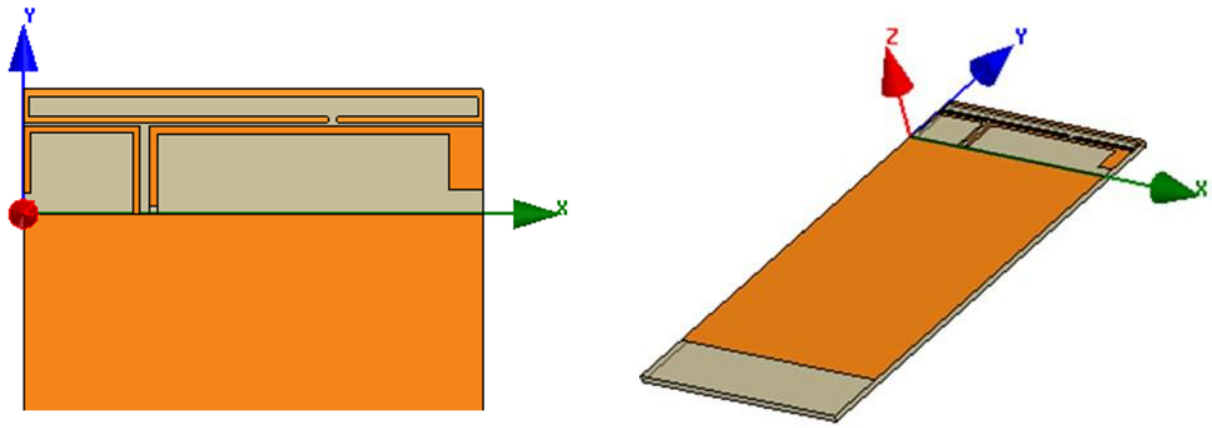

(*a*) Top view of antenna (*b*) Isometric view of antenna

Figure II.8. Antenna model 3

Previously a 2.6 GHz resonant mode with 320 MHz bandwidth covered several LTE,WLAN and WMAN bands. By introducing another resonant mode near 2.0 GHz, the two bands combine to cover a large bandwidth from 1.9 GHz through 2.6 GHz as shown in Figure II.9. Additionally the parasitic elements allows a 1.7 GHz 6-dB return loss to appear. It can be seen from the return loss that the LTE lowband still lacks sufficient spectrum coverage by the antenna. This is further understood by observing the impedance in Figure II.10, that shows the real part of the lowband impedance is very low and needs to be increased in order to match the

50 Ω. Additionally the imaginary part of the impedance shows the capacitive nature of the low frequency region of the antenna.

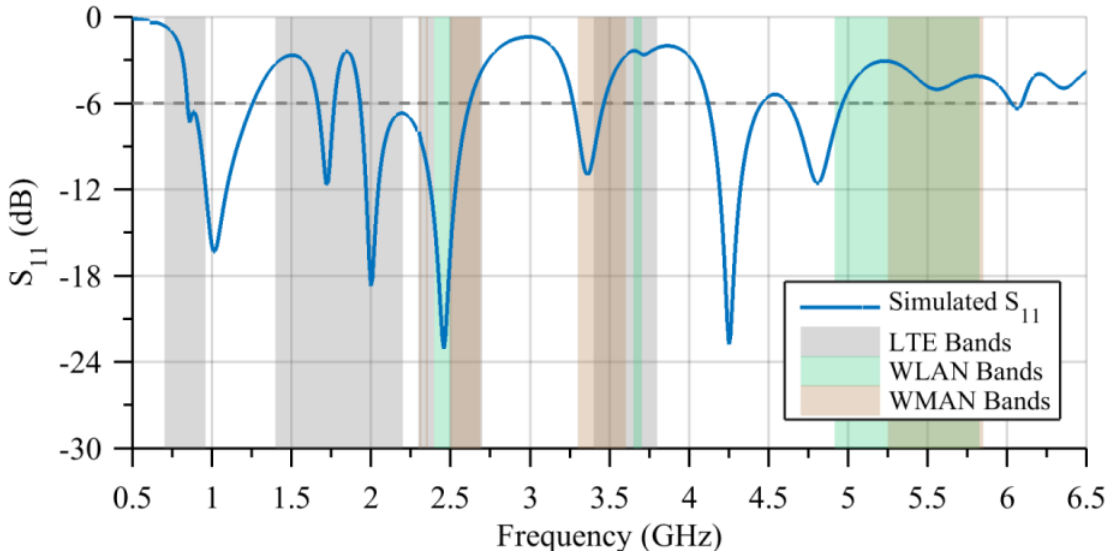

Figure II.9. Return loss versus frequency for antenna model 3

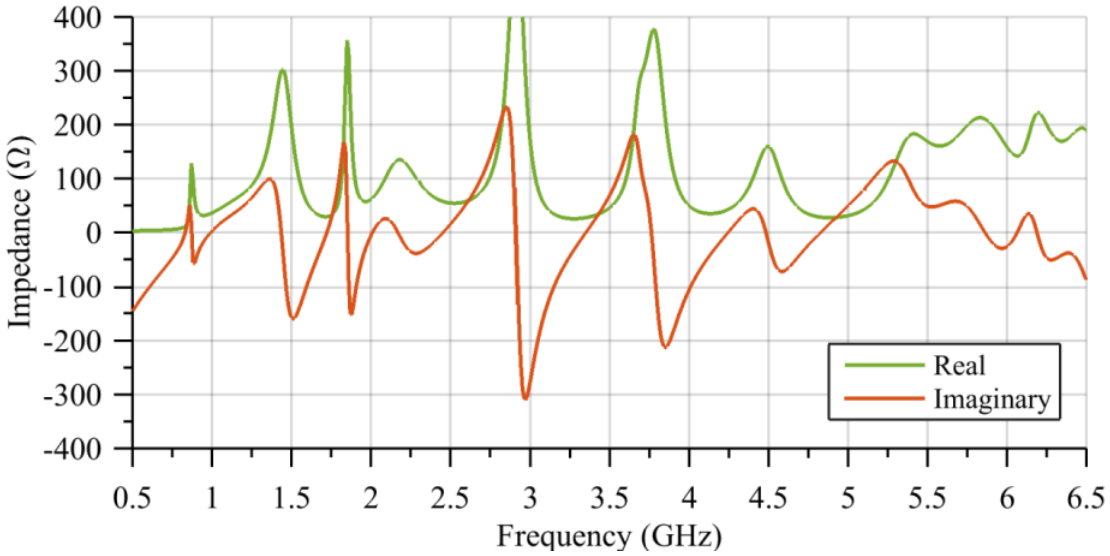

Figure II.10. Input impedance of antenna model 3

Model 4

Compensating for the capacitive behavior of the antenna at low frequency, an inductive element was introduced to help achieve a 0 Ω reactance. This step in the design process consisted

of adding a meander line parasitic element beneath the main monopole element. This broadbanding method was shown by Chang and Liao in [38]; who used a long parasitic meander element coupled to the main antenna to add inductance to an LTE antenna designed for laptops. The new element featured an overall electrical length of 130 mm with a section on top in which two traces are run parallel so that surface current can flow along both traces giving parallel impedance effect.

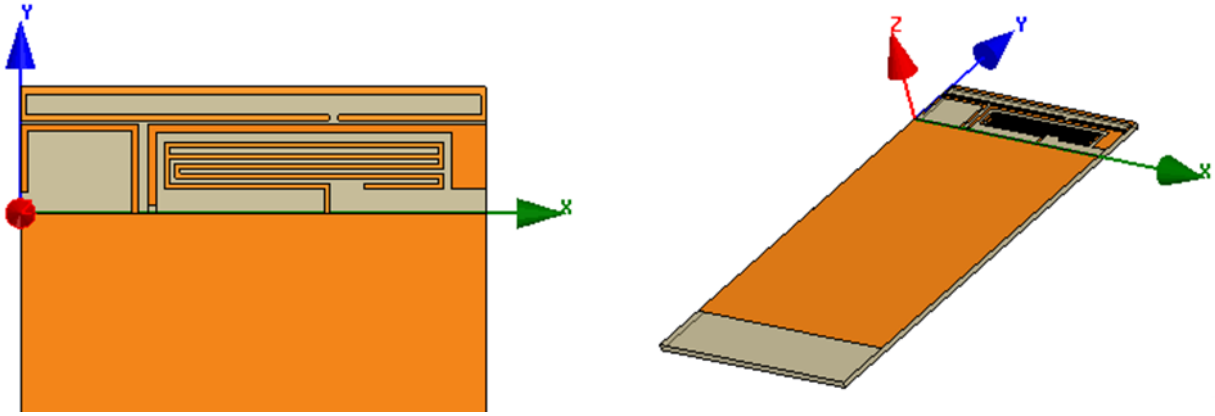

(*a*) Top view of antenna (*b*) Isometric view of antenna

Figure II.11. Antenna model 4

Several new design parameters resulted from the meander line structure such as; the gap between folded traces, the ground connection position, and the distance from the direct fed ILA. Small variations in these parameters introduce noticeable changes in the coupling and overall behavior of the antenna. Some of the effects that the long meander line element has on the performance of the antenna are observed by viewing the return loss. Additional midband operating frequencies are a result of the new structure, as well as small shifts in the low frequency bands.

Direct benefits of the meander element are not fully understood by analyzing the return loss alone; however the antennas impedance shows the main advantages of having such a structure. It is clear in Figure II.13 that an additional low frequency resonance resulted from the parasitic meander line, although this does not show in the return loss due to the real part of the

impedance being very large. Further optimization of the antenna will reduce this impedance so that it can achieve better matching and higher efficiency across the lowband spectrum

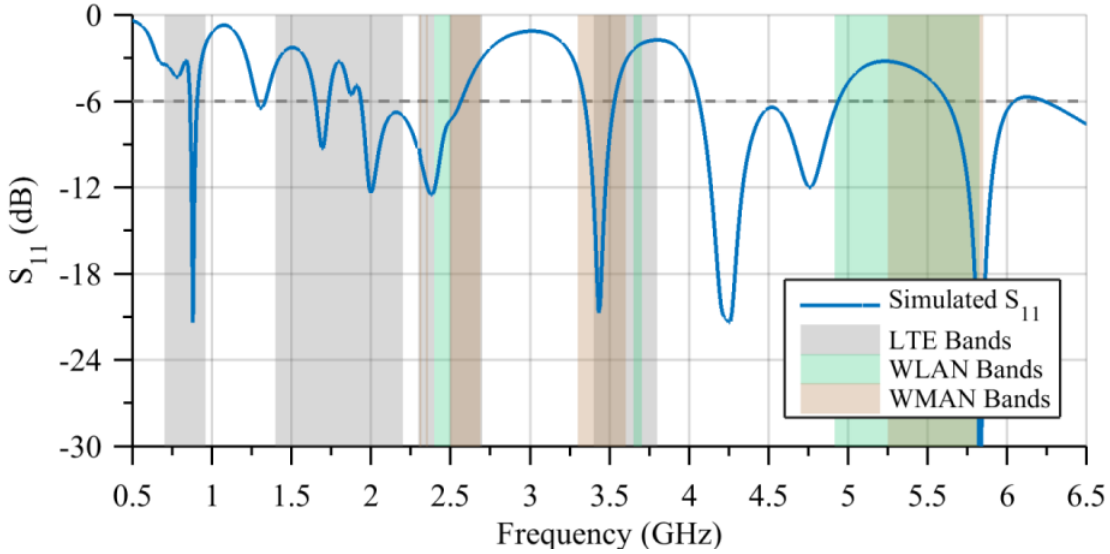

Figure II.12. Return loss versus frequency for antenna model 4

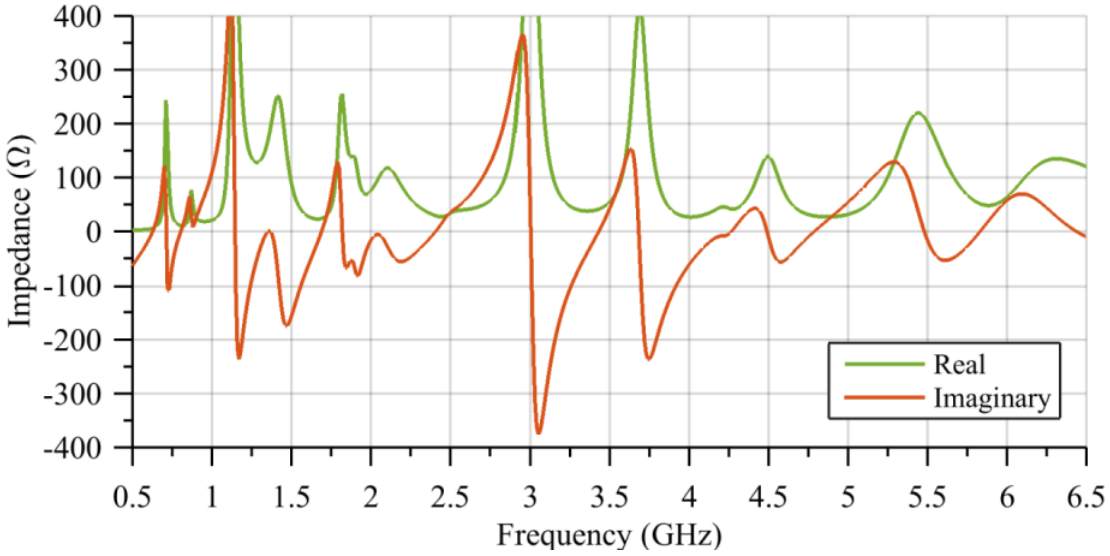

Figure II.13. Input impedance of antenna of antenna model 4

Model 5

Previously elements were added to the antenna based off of a variety of broadbanding methods proven in the literature. Following the addition of these elements, there were sufficient

physical parameters so that a large optimization could be set up. Continuing in the design evolution, there is no need for additional radiating elements. Small changes in the elements were able to affect the performance of the antenna across all desirable operating frequencies.

An initial optimization of all four radiating elements resulted in the antenna configuration shown in Figure II.14. Many considerations affected the optimization technique used; in this step the main objective of the optimization was to have the lowest return loss across as much of the LTE/WLAN/WMAN spectrum as possible based off the first goal of this thesis. In addition to optimizing the antenna elements, it was important to for the antenna to maintain a practical geometry. Since the antenna will be fed by a soldered coaxial cable, the area which will be soldered should be physically large enough to accommodate the process. This led to an increased width at the base of the direct fed monopole. A large flared area was added to the bottom of the ILA to account for this practical feature. The larger solder pad area decreases potential error later introduced by the soldering process.

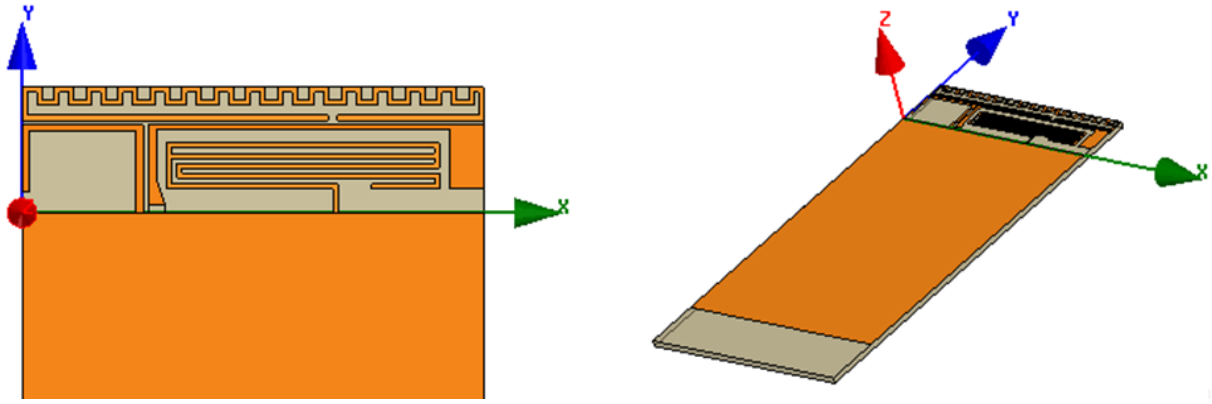

(*a*) Top view of antenna (*b*) Isometric view of antenna

Figure II.14. Antenna model 5

Some of the important changes that took place during optimization included; adjusting the thickness of each element, the gap position and length of the C-shaped monopole, the gaps between elements, the height and position of the meander line element, as well as several

smaller, less noticeable parameters. The C-shaped monopole underwent the most drastic changes during the optimization. Since there was no further room for the element to expand, it was folded into itself in order to create an effectively longer antenna. Meander line antennas utilize the same technique to minimize the size of the antenna.

The return loss that resulted from this optimization step is shown below in Figure II.15. The lowband LTE spectrum bandwidth showed an increase of over 100 MHz. The increased length of the C-shaped coupled monopole shifted its resonance close to that of the meander line element which provided the additional bandwidth across the lower frequency LTE spectrum. Following the first level of optimization the midband LTE spectrum shows a center frequency of 2.3 GHz with over a 1 GHz bandwidth. An operating frequency of 3.45 GHz with a bandwidth of 120 MHz provides coverage of some of the WMAN spectrum. The high frequency operation of the antenna shows an operating bandwidth of over 1.0 GHz and covers both WLAN and WMAN spectrum.

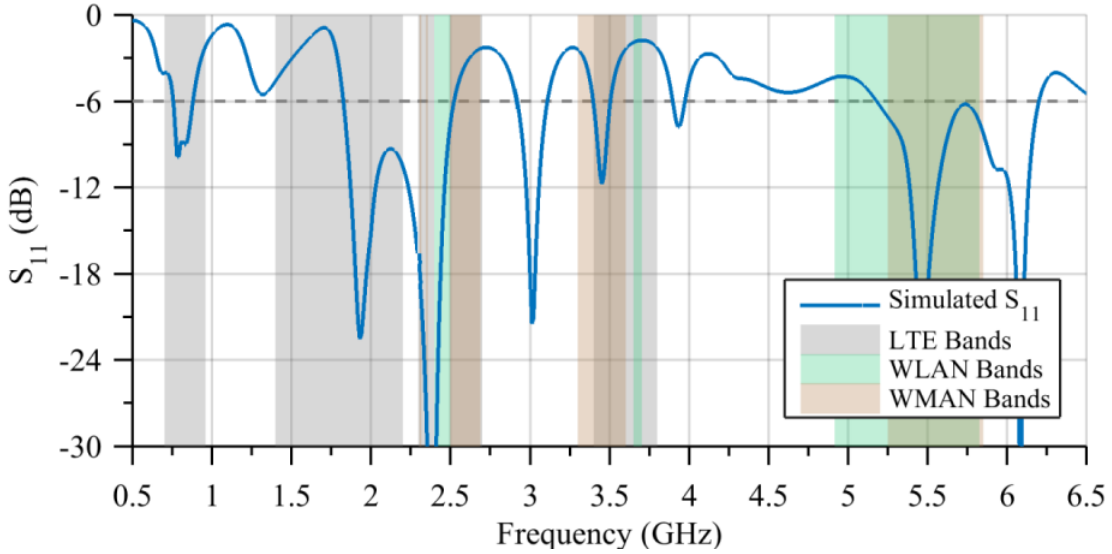

Figure II.15. Return loss versus frequency for antenna model 5

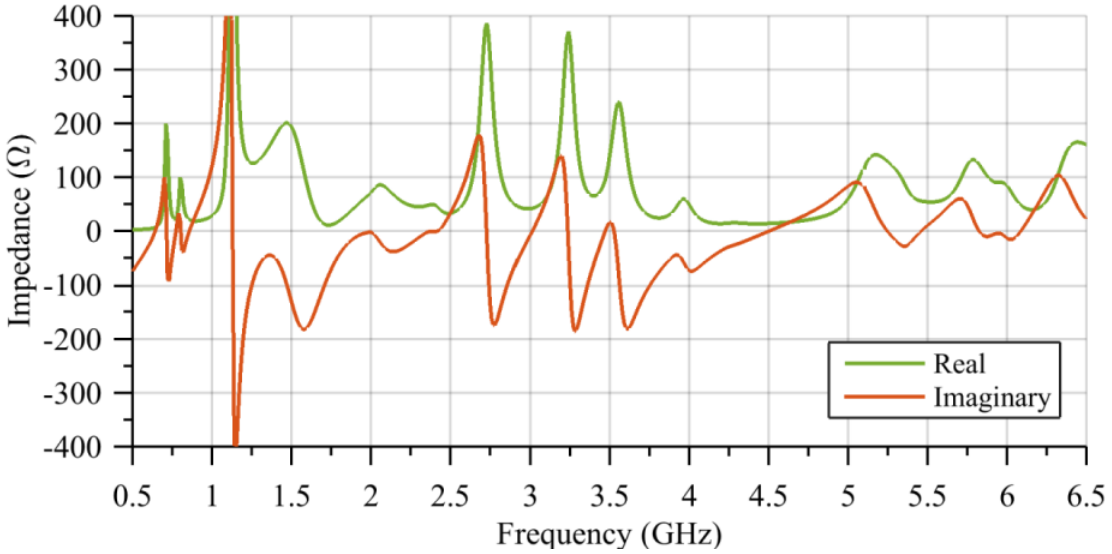

Figure II.16. Input impedance of antenna model 5

Model 6

There are two main components that face size limitations due to physics rather than manufacturing technology in mobile communication devices. The first is clearly the antenna which has been addressed, and the latter is the battery technology within the device. Since the antenna geometry can be more easily optimized than the battery, purposely altering the ground plane to create space required for a battery will allow an easier integration of these two size limited components. Thus the last feature added to the antenna was a ground plane cutout. The 45×30 mm planar cut away area is comparable in size to that of common batteries in cell phones today. Similar ground plane alterations have even been used as a broadbanding technique for a single antenna by Lu *et al.* in [37] however trying to adopt this technique for a MIMO antenna proves difficult due to the high correlation between antennas on the ground plane.

Changing the size and shape of the substrate and ground plane has an effect on the fundamental Eigen mode resonances of the structure that mostly alters the low frequency behavior of the antenna. Accounting for these major changes, the antenna was optimized with

more focus on the low frequency bands. Once again increasing the length of the C-shaped coupled monopole positively affected the low frequency performance of the antenna. The high frequency behavior was less affected by the changes because the elements radiating power at high frequency are using the parasitic elements to drive against rather than the main ground plane. The following section shows a more extensive overview of the antennas behavior, resulted from the last step in the single antenna design process.

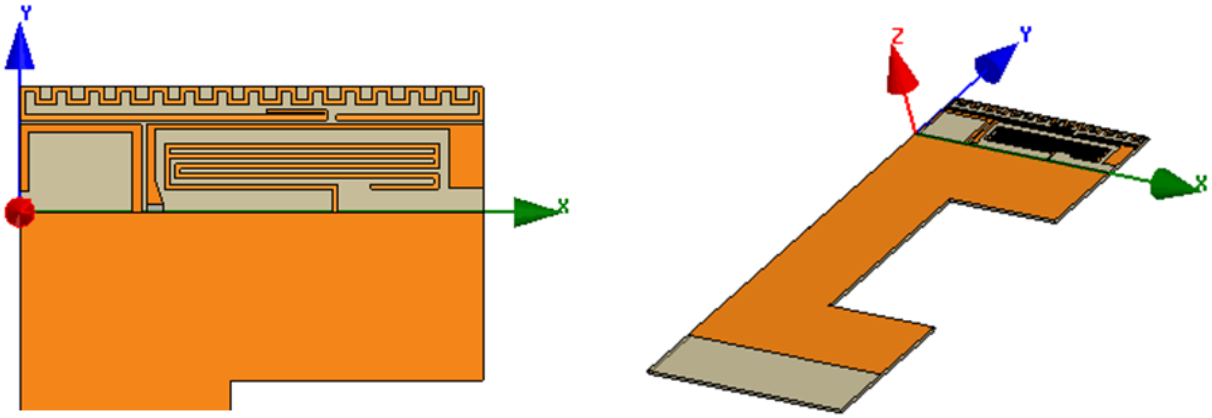

(*a*) Top view of antenna (*b*) Isometric view of antenna

Figure II.17. Antenna model 6

C. Single Antenna Simulated Characteristics

The previous design methodology resulted in a single antenna featuring a uniplanar design with a direct fed ILA, coupled to parasitic elements and a meandered monopole structure. The simple uniplanar design utilizes geometries that can be easily fabricated and integrated with current mobile communication devices. An example of the antenna within a skeleton of a mobile phone shown below in Figure II.18. Since the antenna was designed with initial size limited constraints, it easily fits within the average size of a mobile phone device. The entire antenna substrate occupies less than 13 % of the total volume within the phone, while the radiating elements take up less than 2 % of the space.

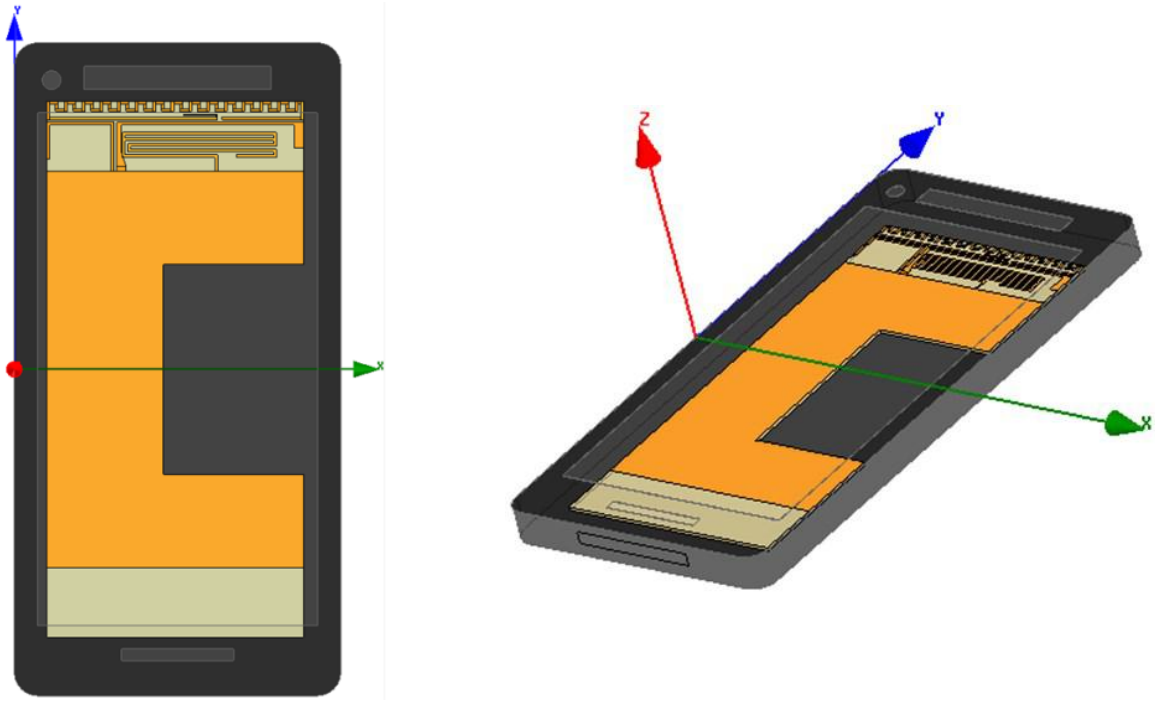

Figure II.18. Antenna model shown relative to a standard size mobile phone

The characterization of the antenna consisted of observing several different quantifiable results of the simulation including as return loss, radiation patterns, peak gain and efficiencies. Using these standard metrics to characterize the antenna provided insight into the behavior of the single antenna relative to previously discussed mobile communication antennas from the literature as well as the goals set forth in Chapter 1.

Return Loss

The scattering parameters shown in Figure II.19 indicate the amount of power accepted by the antenna. The 6-dB return loss cutoff is shown via a dashed line in the figure, an S_{11} below that indicates acceptable values for operation in mobile communication devices. The simulated antenna showed several wide bandwidth regions of operation. The lowest operating range of the antenna was 745-985 MHz providing a bandwidth of 240 MHz. Based on the 6-dB return loss criteria, the low frequency region shows good performance across LTE bands 5, 6, 8, 13, 14, 17, 18, 19, 20, 26, 27, 28, 44 found in Table I.2-3. These low frequency bands represent the most

challenging design problems for mobile communication antennas due to the size restraints of the devices.

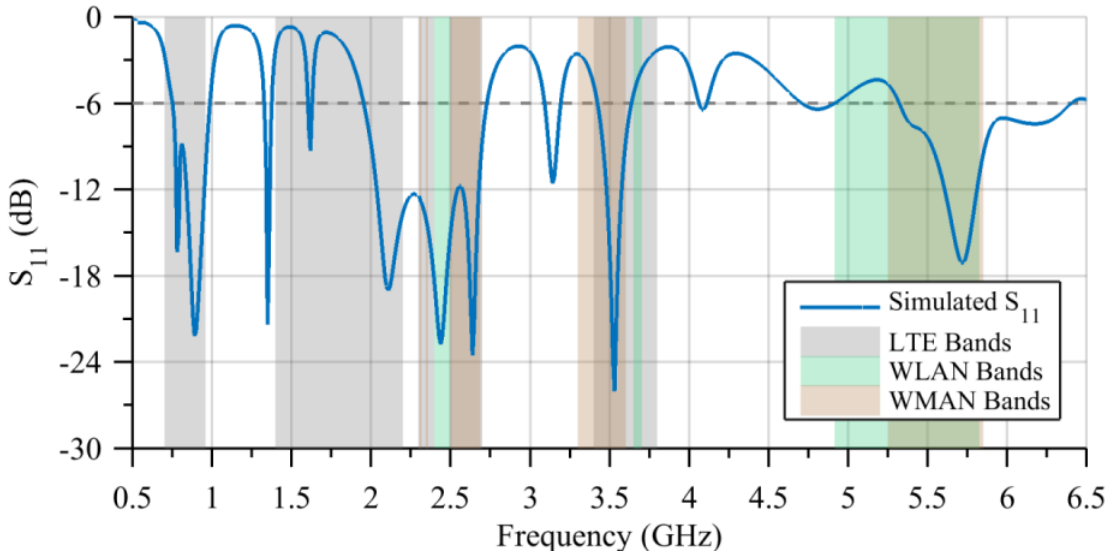

Figure II.19. Single antenna simulated return loss

Again based on the 6-dB return loss standards, a midband operating region is defined from 1950-2720 MHz. This region covers LTE bands 1, 7, 23, 30, 34, 36, 38, 40, 41 as well as the common 2.5 GHz WLAN band, 2.3 GHz and 2.5 GHz WMAN bands. The simulated antenna shows another operating region centered at 3.5 GHz and experienced greater than 6-dB return loss from 3420-3640 MHz covering LTE bands 22, 42, 43. The 3.5 GHz operating region also covers the 3.5 GHz WMAN spectrum. Additionally the highest spectral range that the antenna shows good return loss across is 5300-6400 MHz. This high frequency wide bandwidth region covers the majority of the WLAN and WMAN 5 GHz spectrum.

Radiation Patterns

The antennas radiated power patterns below in Figure II.20-23 show the three main cross sections of the antenna, X-Y where $\theta=90^0$ and φ is swept (a), X-Z where $\varphi=0^0$ and θ is swept (b), and Z-Y where $\varphi=90^0$ and θ is swept (c). The overall radiating behavior of the antenna can

be interpolated from these three major cross sections. Since the radiating properties of an antenna are frequency dependent it was important to consider the characteristics across a wide range of spectrum; so the radiation patterns shown were taken in the center of the four main operating regions of the antenna.

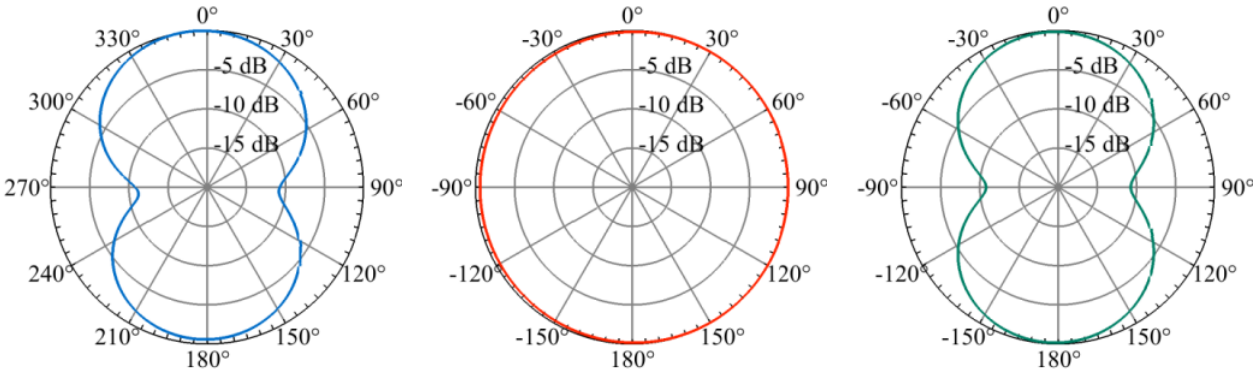

(*a*) X-Y cross section θ=90^0 (*b*) X-Z cross section φ=0^0 (*c*) Z-Y cross section φ=90^0

Figure II.20. Simulated radiation patterns of single antenna at 850 MHz

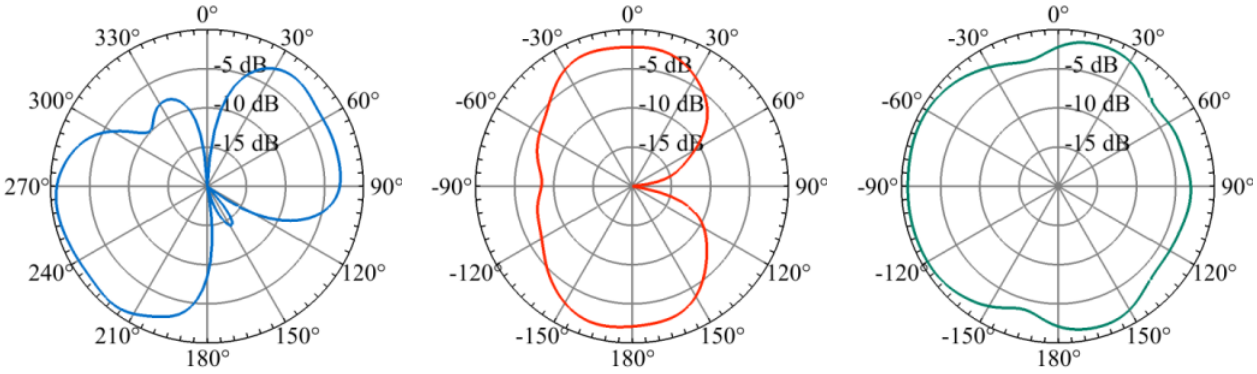

(*a*) X-Y cross section θ=90^0 (*b*) X-Z cross section φ=0^0 (*c*) Z-Y cross section φ=90^0

Figure II.21. Simulated radiation patterns of single antenna at 2500 MHz

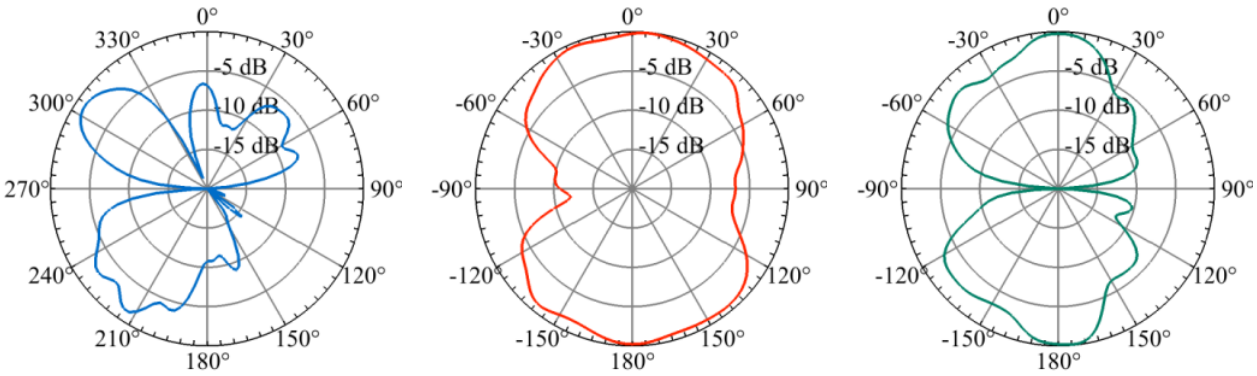

(*a*) X-Y cross section θ=90^0 (*b*) X-Z cross section φ=0^0 (*c*) Z-Y cross section φ=90^0

Figure II.22. Simulated radiation patterns of single antenna at 3500 MHz

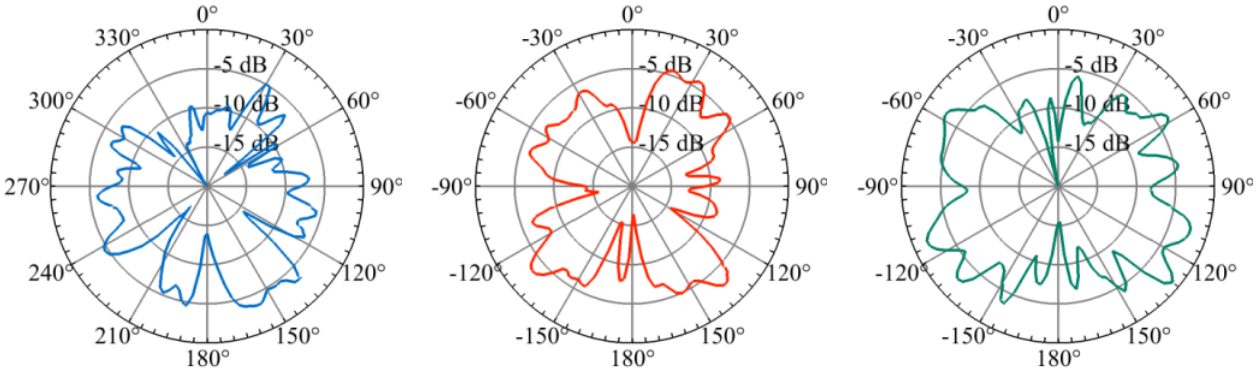

(*a*) X-Y cross section θ=90^0 (*b*) X-Z cross section φ=0^0 (*c*) Z-Y cross section φ=90^0

Figure II.23. Simulated radiation patterns of single antenna at 5700 MHz

The observed far field radiated power plots in Figure II.20 at 850 MHz show a nearly ideal pattern concerning communication devices. These cross-sectioned patterns have the desired omnidirectional doughnut shaped coverage. At higher frequencies the radiation patterns begin to become slightly distorted. The patterns in Figure II.21 at 2500 MHz show a similar overall behavior to the 850 MHz patterns, however it is clear that the fields are orthogonal. The low frequency pattern show a uniform radiated power across the X-Z plane, whereas the midband patterns are most uniform in the Z-Y plane, which is an indication that different antenna elements are responsible for the radiated fields. In other words, at 850 MHz the strongest

components of the surface currents on the antenna are in the parallel to the Y axis, while at 2500 MHz the strongest components are parallel to the X axis. As the operating frequency is increased up to 5700 MHz it is clear from the patterns that many antenna elements are affecting the behavior of the overall radiated power. Still, even at this high frequency the patterns shows mostly non-directional behavior as very few deep nulls occur.

Gain

Another characteristic of the antenna to observe is the peak gain. The peak gain at a given frequency can be added to the radiation pattern plots to result in gain plots. Figure II.24 plots the peak gain versus frequency of the single antenna simulation showing the trend in behavior of the antenna. The peak gain was shown only across frequencies in which the return loss was 6-dB or better. Outside of these frequency bands, the antenna is not accepting enough power to be considered operating thus the gain has no practical meaning.

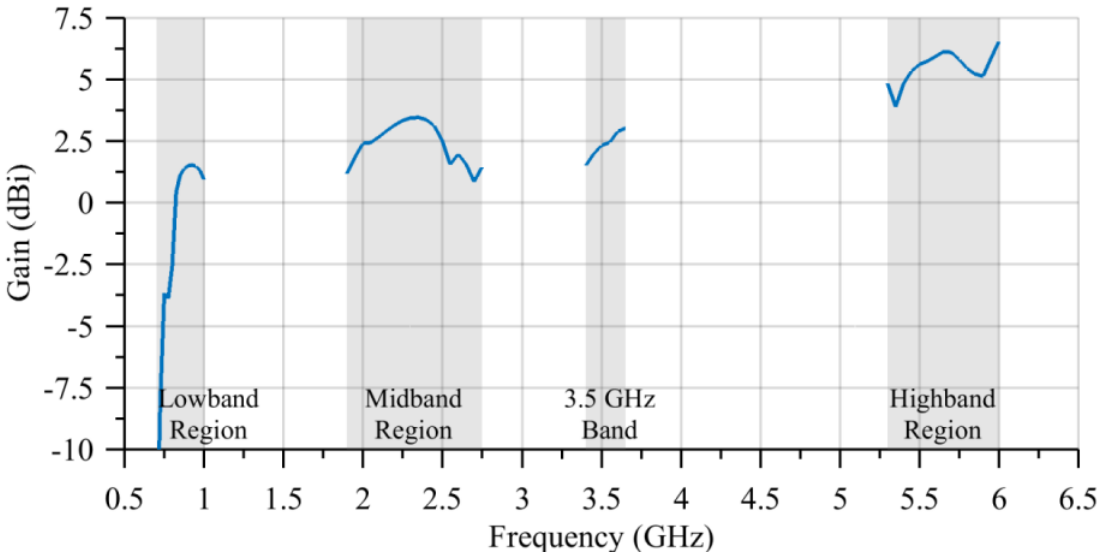

Figure II.24. Simulated peak gain for single antenna

As expected, at lower frequencies when the antennas radiation pattern is very omnidirectional, the peak gain is around 2.15 dBi. Also as the antenna becomes more directional

and the radiated power is not evenly distributed such as the high frequency cases, the peak gain becomes greater. The inverse correlation between the uniform distribution of radiated power and gain is observed for the antenna, and can be understood from Eq. I.9. The 6-dB return loss was used as criteria for defining regions of operation, however the lowband region from 745-800 MHz shows a peak gain of less than -2.5dBi indicating that despite accepting power indicating the antenna may not be radiating power.

Efficiency

The simulated antenna shows high efficiency across all operating regions except for the lowband region from 745-800 MHz. Despite having good return loss in this region, initial assumption after viewing the peak gain data that this region is not efficiently radiating power holds true. This is the due to the antenna dissipating power in the form of heat rather than radiating.

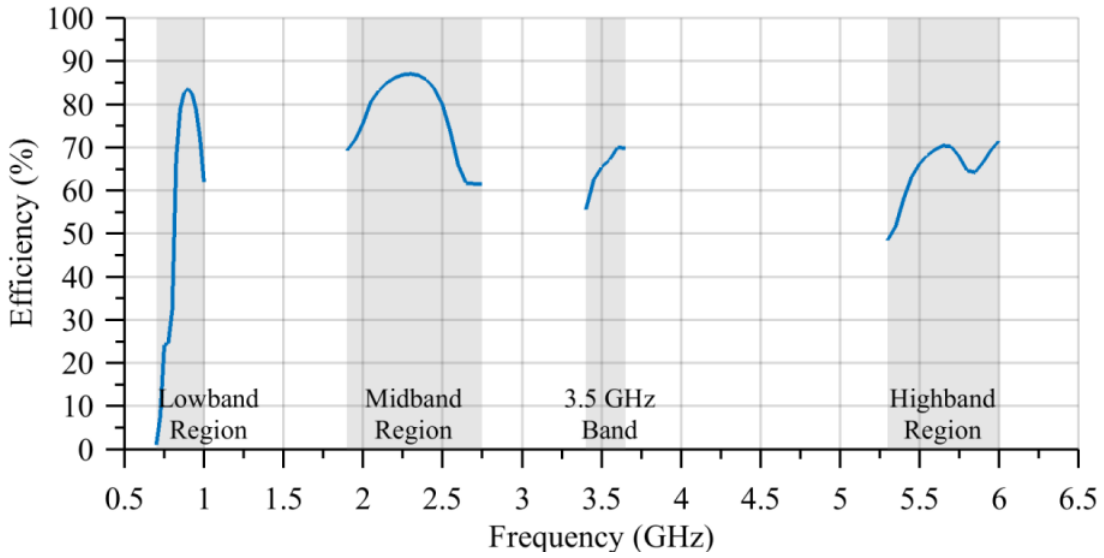

Figure II.25. Simulated radiation efficiency for single antenna

As previously mentioned, electrically small antennas typically suffer from poor radiation efficiently due to the fundamental limitations of electrically small antennas so the low efficiency

is not completely surprising. Apart from the small area in the lowband region, all other operable regions show good efficiency and indicate that the antenna is performing well across the spectrum.

D. MIMO Antenna Design

Maintaining the original substrate size and geometry of the single antenna design, a MIMO configuration was implemented, shown in Figure II.26. A space, 15×55×1.54 mm was left available on the bottom half of the substrate so that the single antenna element could be mirrored across the center of the board. Intentionally removing the conductive layer in that area throughout the single antenna design allowed for the MIMO antenna to be integrated onto the substrate with ease. The MIMO antenna simulation model in Figure II.26 clearly depicts both radiating elements along with their individual feed points. The design featured the original size and shape of the substrate and antenna element 1, with the second element mirrored across the ground plane. The two-element MIMO antenna was simulated using HFSS™ with the same model domain and boundary conditions as the single antenna.

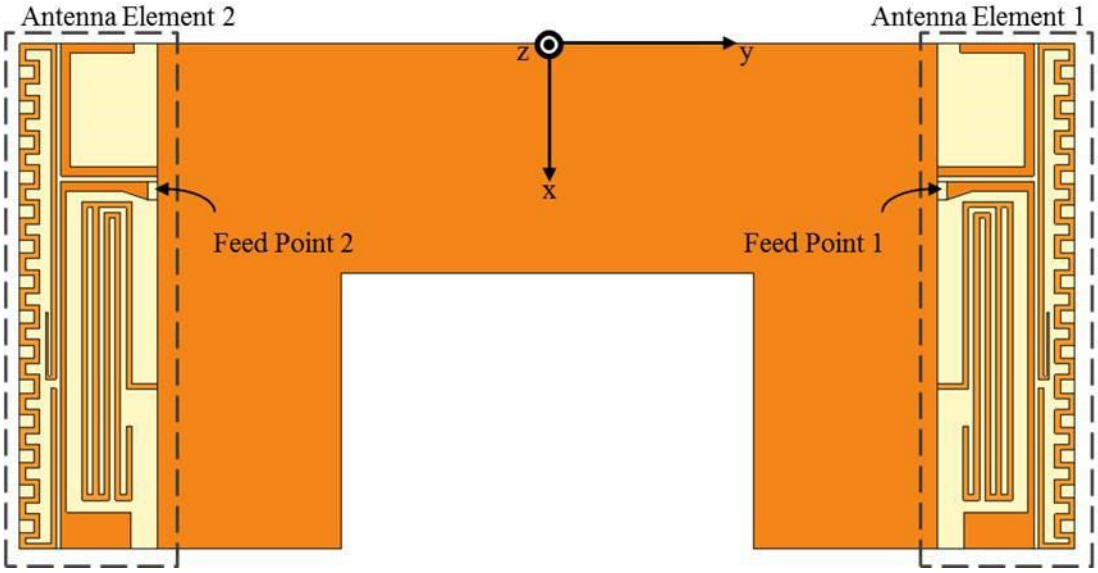

Figure II.26. MIMO simulation model

The only difference between models is the addition of the second antenna element and feed source.

Scattering Parameters

While the single antenna's scattering parameters only consisted of the S_{11} reflection coefficient or return loss; the MIMO antennas scattering parameters contain much more information. Each antenna element within the MIMO system has a unique reflection coefficient since they are excited separately. Therefor S_{11} represents the reflection coefficient for element 1, and S_{22} is the reflection coefficient for the second antenna element. Additionally the transmission coefficient S_{21} is the ratio of power seen at element 2 when element 1 is excited; likewise S_{12} would be the ratio of power seen at element 1 when element 2 is excited. The transmission coefficient is also known as insertion loss or mutual coupling because it represents the correlation between two separate ports. Since the MIMO antenna is a passive network, S_{12} will always be equal to S_{21} which is the reasoning for plotting them as one value in the figures. The scattering parameters of the simulated model are shown in Figure II.27.

The return loss of antenna element 1 and 2 are nearly indistinguishable from one another. Since both antenna elements are geometrically identical, the similar input behavior of the elements was expected. The only difference between the two elements is their orientation relative to the ground plane cutout. The isolation parameters between ports show good diversity in the midband, 3.5 GHz, and highband regions; all of which show an S_{12} and S_{21} below -12 dB. The lowband region of operation shows a much higher correlation between ports with the isolation parameters reaching nearly -6 dB. The lower isolation in this region is not surprising, since the low frequency region uses the ground plane to help radiate. This correlation is a result of the mutual surface currents generated on the ground plane at the low frequencies.

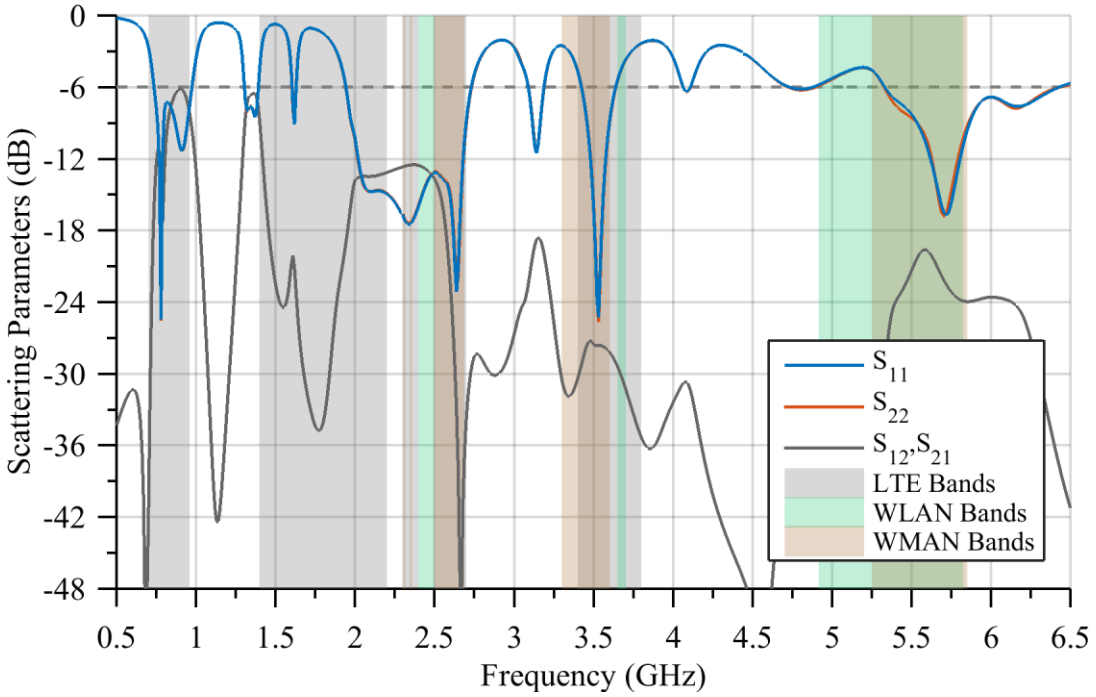

Figure II.27. MIMO simulation scattering parameters

The four main operating regions are similar to the single antenna results. The lowband provides greater than 6-dB return loss from 730-995 MHz which covers LTE bands 5, 6, 8, 12, 13, 14, 17, 18, 19, 20, 26, 27, 28, 44 from Table I.2-3. An 800 MHz bandwidth region meets the 6-dB return loss criteria from 1940-2740 MHz. This midband region can operate on LTE bands 1, 7, 23, 30, 34, 36, 38, 40, and 41. Additionally the antenna system shows good performance on the 2.5 and 2.3 GHz WLAN and WMAN bands. The MIMO antenna's third main operating region is in the 3.5 GHz spectrum, 3420-3640 MHz, which is responsible for LTE bands 22,42, 43 as well as the 3.5 GHz WMAN band. The antenna shows a 1100 MHz bandwidth high frequency operating region, 5330-6430 MHz exhibiting a 6-dB return loss or greater. This highband spectrum covers many of the 5 GHz WLAN and WMAN channels. Overall the MIMO antenna completely covered 19 LTE bands, and partially covered another 12 LTE bands meaning

the MIMO antenna is operable on 31 of the 42 LTE bands as well as the common WLAN and WMAN spectrum.

Radiation Patterns

Independent power radiation patterns cross sections can be observed for each antenna element by exciting one terminal while terminating the other with a 50 Ω load. Similar to the single antenna setup, the radiation patterns are plotted below in the center of each operating band so that the frequency dependent behavior is shown. The three major radiation pattern cross sections; X-Y, X-Z, and Z-Y are shown below for each radiating element.

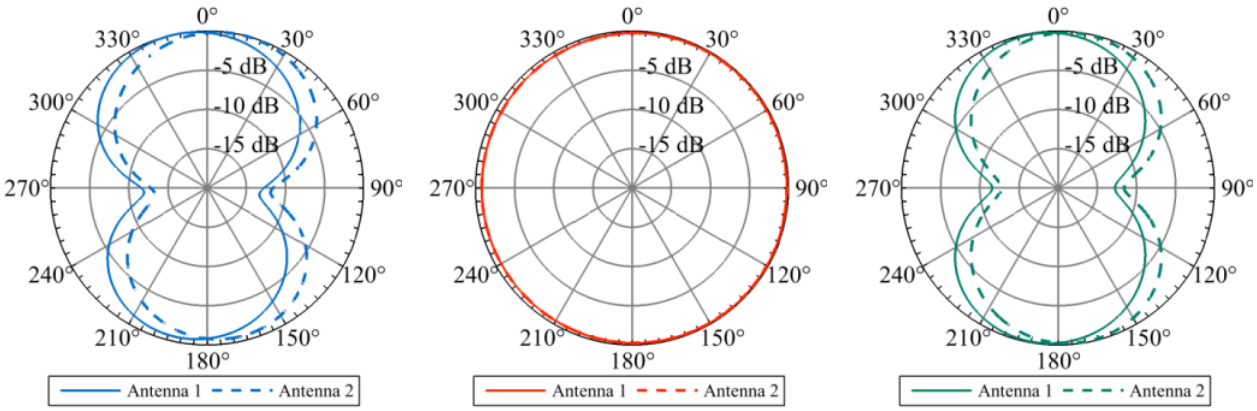

(*a*) X-Y cross section θ=90^0 (*b*) X-Z cross section φ=0^0 (*c*) Z-Y cross section φ=90^0

Figure II.28. Simulated radiation patterns of MIMO antenna at 850 MHz

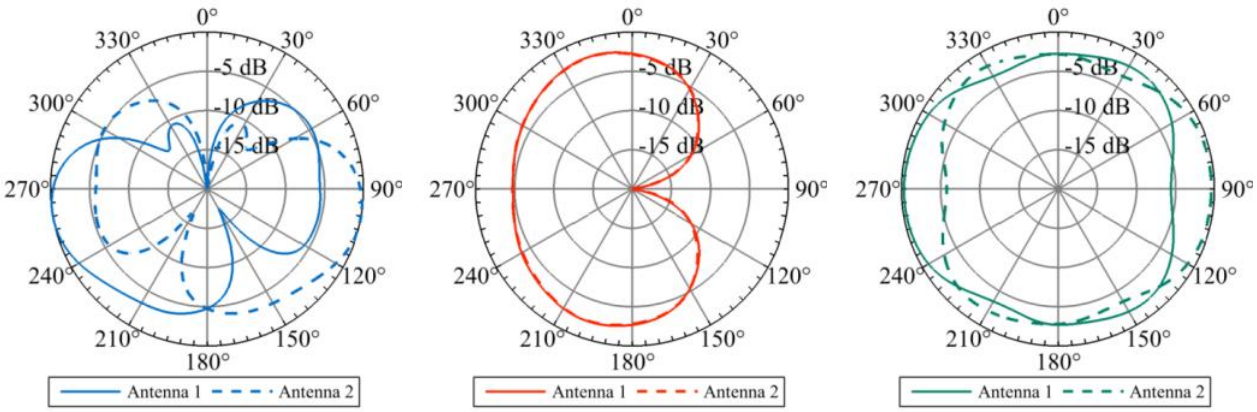

(*a*) X-Y cross section θ=90^0 (*b*) X-Z cross section φ=0^0 (*c*) Z-Y cross section φ=90^0

Figure II.29. Simulated radiation patterns of MIMO antenna at 2500 MHz

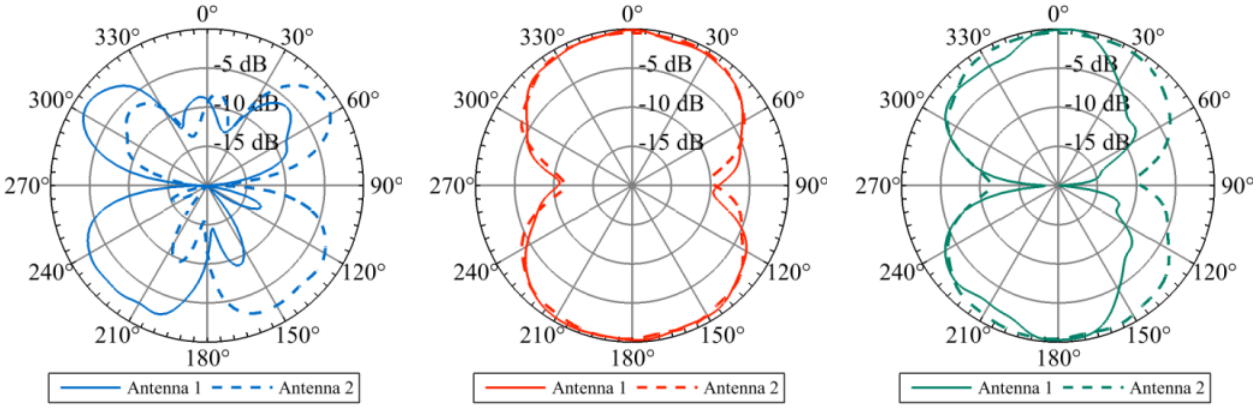

(*a*) X-Y cross section θ=90^0 (*b*) X-Z cross section φ=0^0 (*c*) Z-Y cross section φ=90^0

Figure II.30. Simulated radiation patterns of MIMO antenna at 3500 MHz

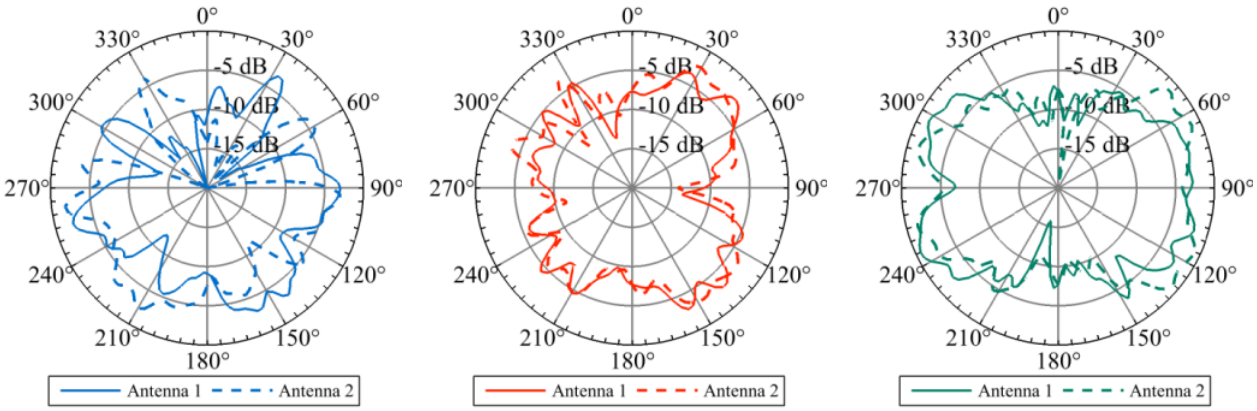

(*a*) X-Y cross section θ=90^0 (*b*) X-Z cross section φ=0^0 (*c*) Z-Y cross section φ=90^0

Figure II.31. Simulated radiation patterns of MIMO antenna at 5700 MHz

Since the second radiating element was mirrored normal to the X-Z plane, the radiation patterns cut across the Y-axis were expected to be a reflection of the first antenna element. This expectation holds true for all of the radiation pattern cuts shown above in Figure II.28-32 (*a*) and (*c*). The radiating behavior of the MIMO elements have very similar qualities to the single antenna simulations previously shown. Following this trend, the low frequency radiation patterns are omnidirectional and the higher frequency patterns show the scattering interference from several radiating elements affecting the overall directivity. Despite the interference, even at

5700MHz there exist very few nulls less than -15 dB and the radiated power distribution remains relatively uniform.

The 850 MHz radiation patterns that show omnidirectional behavior in the X-Z cross section can be explained by observing the surface currents. Figure II.32. *(a)* below shows the surface currents at 850 MHz when antenna element one is excited. The strong alignment on the ground plane parallel to the Y axis are responsible for the X-Z omnidirectional behavior. Additionally Figure II.32. *(b)* shows the currents at 2500 MHz. At 2500 MHz it is noted that the surface currents along the ground plane do not show significant alignment parallel to the Y axis, in this case the majority of surface currents are running parallel to the X axis which creates gives the omnidirectional behavior in the Z-Y cross section.

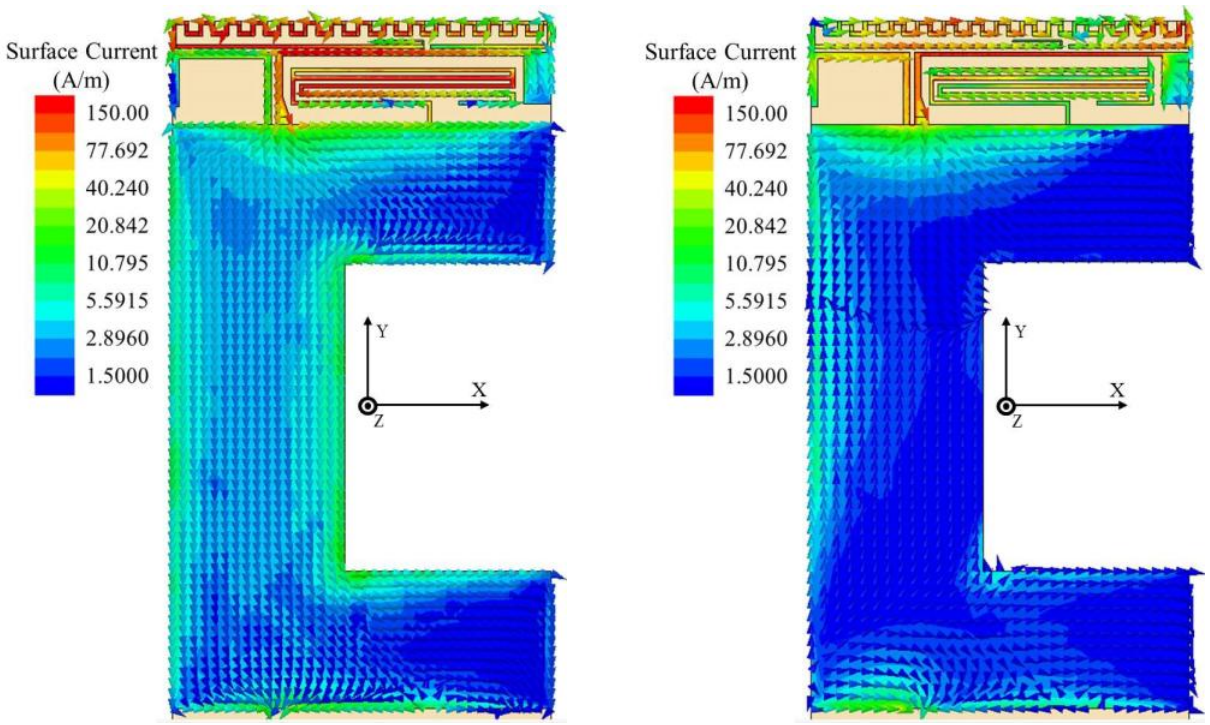

(*a*) 850 MHz (*b*) 2500 MHz

Figure II.32. Surface currents along ground plane and radiating elements

Gain

Since the antenna elements were independently excited, the peak gain could be calculated for each; the results are in shown in Figure II.33. Once again these calculations are only shown in regions where the antenna met or exceeded the 6-dB return loss criteria for operation since areas outside of this region are not of interest.

Similar to the single antenna results; the peak gain of the MIMO antenna elements shows consistent and expected behavior aside from the 745-800 MHz region. Although the low gain experienced in this region is not desired, it is not an unexpected phenomenon since the single antenna displayed the same performance.

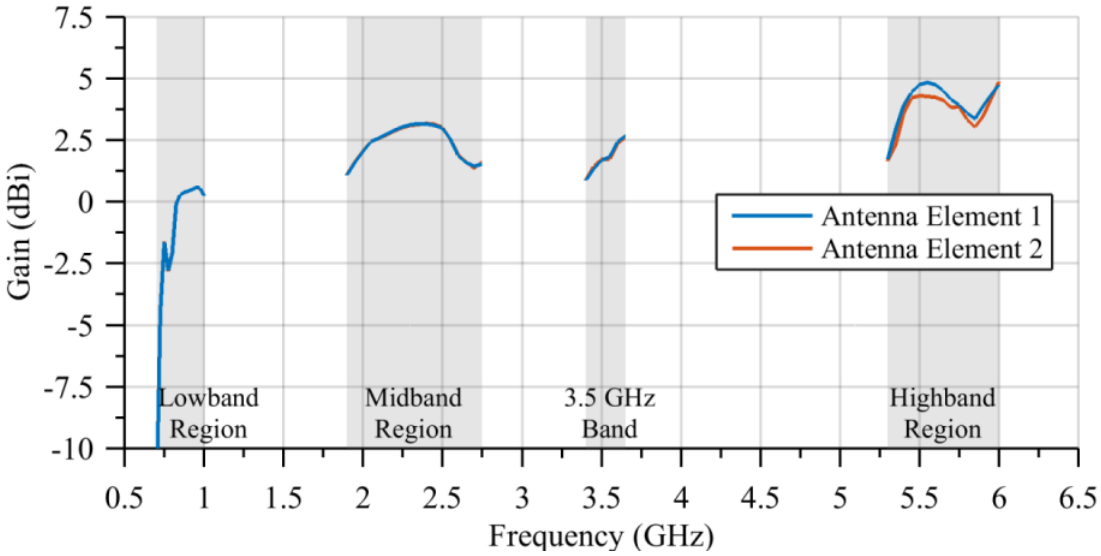

Figure II.33. Simulated peak gain for MIMO antenna

Efficiency

The radiation efficiency for each MIMO antenna element was also calculated; the results are shown below in Figure II.34. Outside of the previously mentioned obscure lowband region, the radiation efficiencies are as also as expected. The radiation efficiency is slightly less for each MIMO element compared with the single antenna results previously shown in Figure II.25. This

behavior arises from the additional loss caused by the extra conductive components that make up the second radiating element as well as some destructive interference along the ground plane. The radiation efficiency of 39-63% from 750-1000 MHz is comparable or better than similar sized LTE antennas in the literature such as [30], [39], [71]. The midband, 3.5 GHz, and highband operating regions of the MIMO antenna all show high radiation efficiency ranging from 50-85 %.

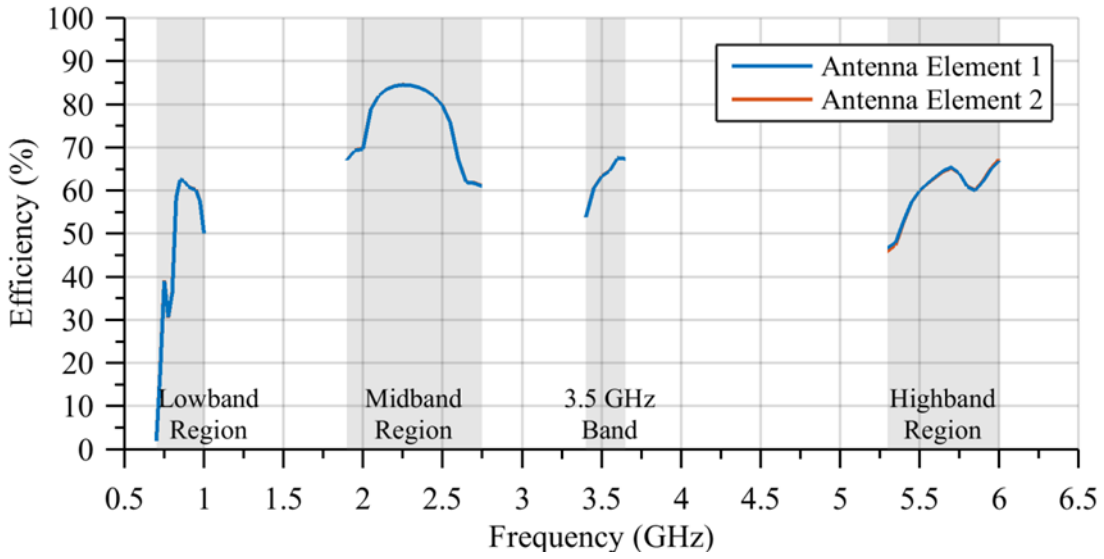

Figure II.34. Simulated radiation efficiency for MIMO antenna

Envelope Correlation Coefficient

Using the complex scattering parameters from the MIMO antenna simulation, the envelope correlation coefficient was calculated with Eq. I.11. As previously mentioned lower ECC values correspond to lower correlation between antenna elements and thus a greater system diversity which is needed for a MIMO system to operate effectively.

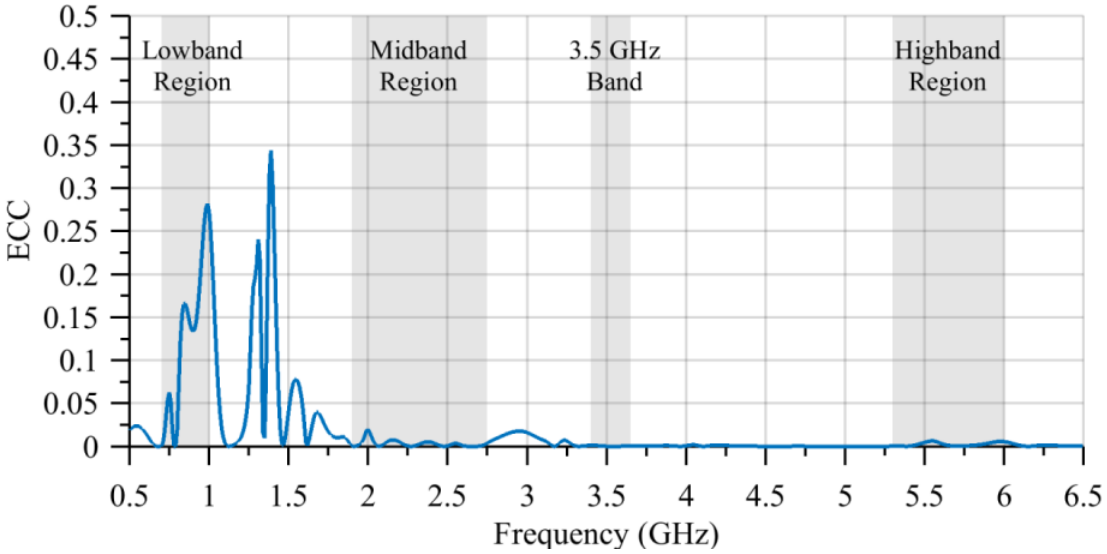

Figure II.35. Simulated envelope correlation coefficient for MIMO antenna

Despite the electrically small limitations of the lowband, the envelope correlation coefficient was less than 0.28 across the entire region meaning the MIMO antenna provided good diversity. Additionally the midband, 3.5 GHz, and highband operating regions of the MIMO antenna all show a low correlation of less than 0.02 in each region. The low correlation values shown by the simulated MIMO model are in good agreement with the original goals set in Chapter 1 and should provide an increased channel capacity.

III. Antenna Fabrication and Measurements

A. Fabrication Procedure

One of the goals for the MIMO antenna was to make use of cost effective materials in the design. The FR4 material used was 370HR by ISOLA. The 370HR was single sided 1 oz. copper with a thickness of 1.56mm. This material was selected since it is readily available and has physical properties that are strong enough to withstand the process of milling. The milling process consisted of mechanically removing the top layer of exposed copper by means of various high-speed drill bits.

An Accurate CNC 427 milling machine was used along with PhCNC prototyping software to etch the designed antenna structure onto the single sided ISOLA 370HR substrate. The CNC milling machine featured an absolute position accuracy (X,Y) of 7.5 μm and a minimum gap size of 0.1 mm [77]. The milling machine provided much greater resolution than required to fabricate the antenna which had a minimum resolution sizes of 0.1 mm and gaps of 0.6 mm. Since the antenna featured simple geometries and majority of the board was the ground plane that did not require etching; the milling process was completed in under one hour. Once the MIMO antenna board was milled, the coaxial connectors had to be attached to the feed points on the antenna structure. The coaxial connecters represent the interface to which the antenna can be connected to external measurement equipment for characterization. Pasternack PE3109 RG405 coaxial cables were used for the antenna feed. One end of the rigid 12 inch, 50 Ω coax line was bent to form an easy connecting interface protruding from the ground plane of the antenna. The other end was cut and stripped exposing around 1mm of the center conductor which was then folded down and soldered to the feed point of the direct fed ILA. After the center conductor was soldered to the antenna, the outer conducting jacket of the coaxial cable was

soldered directly to the ground plane. Soldering multiple locations ensured that the surface currents on the ground plane would behave as simulated and not meander along only the coaxial cable.

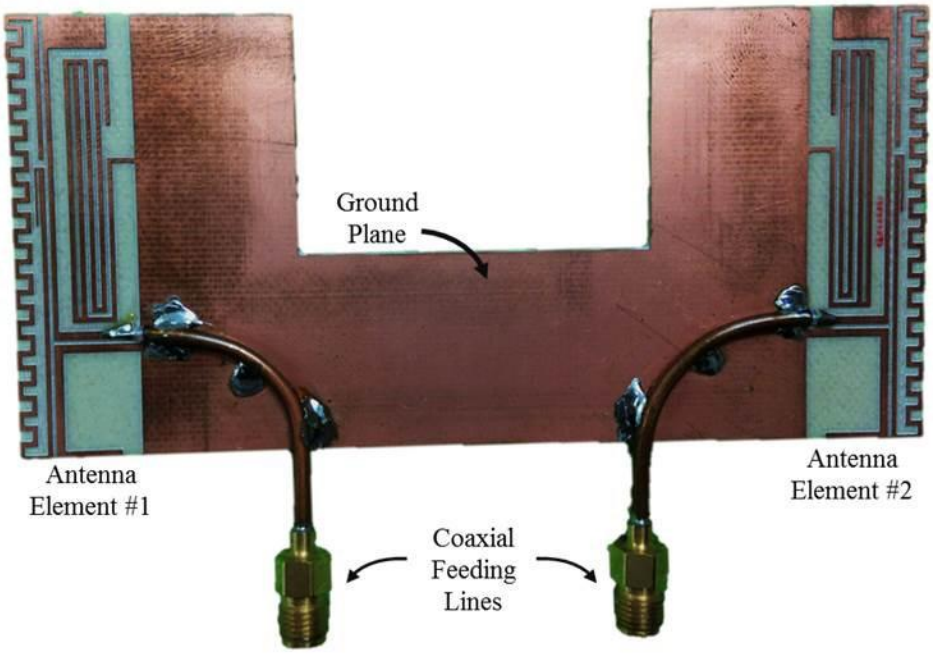

Figure III.1. Fabricated MIMO antenna photograph

B. Measurement Equipment

Network Analyzer

Various measurement techniques and equipment were utilized in the characterization of the MIMO antenna. Vector network analyzers are the most fundamental measurement equipment for all RF and microwave devices. A network analyzer is a piece of equipment that features a continuous wave variable frequency source which excites a device; the reflection and transmission seen from each port on the analyzer can then be measured and the device parameters can be calculated. Vector network analyzers can measure both magnitude and phase of transmitted and reflected signal which provides a means to measure complex frequency domain responses such as scattering parameters and impedance, as well as time domain

responses. A basic block diagram showing the principle operating theory of a vector network analyzer is shown in the figure below.

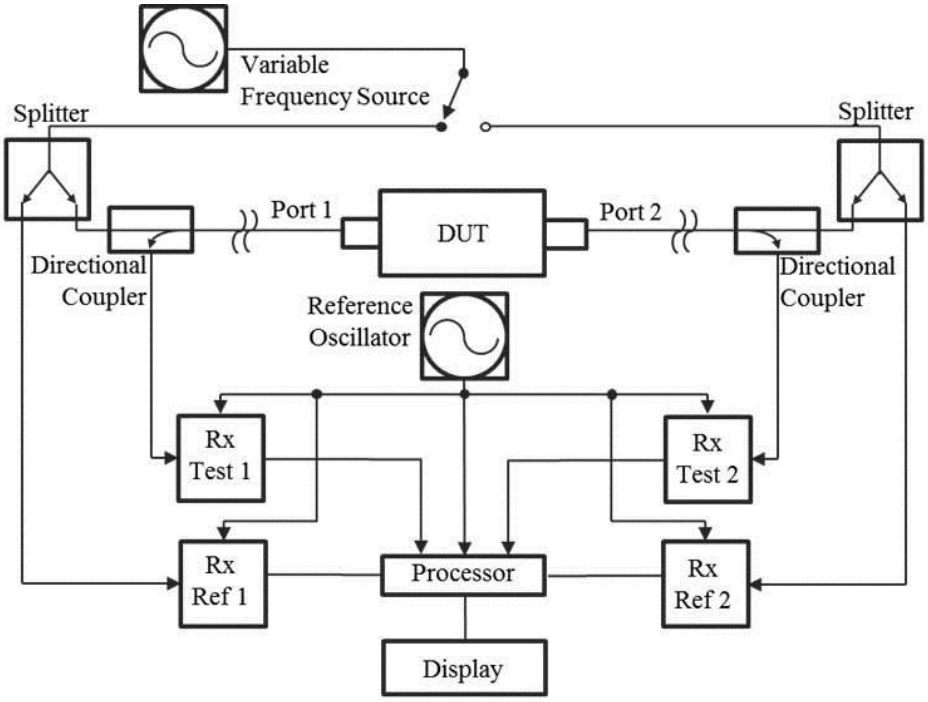

Figure III.2. Simple block diagram of a network analyzer [78]

The figure shows the measurement of a two port device under test (DUT) in the middle. The analysis begins by a variable frequency source supplying power to either port 1 or port 2. The power is then split so that a reference for the measured power signal is available. The other part of the split signal travels to port 1 of the device under test where some of the power is then reflected back from the input of the device. This reflected power is then filtered through the directional coupler and measured at Rx Test1. The network analyzer then processes and compares the test power and the reference power to calculate the magnitude and phase of the reflection seen at port 1 of the DUT, this value would be the S_{11} parameter. Alternatively power can be supplied to port 1 and measured at port 2, the S_{12} value, or supplied to port 2 and measured at port 2 giving the S_{22} value.

An HP 8510 network analyzer was used to characterize the fabricated MIMO antenna. This network analyzer is capable of sourcing and measuring signals from 45 MHz to 26.5 GHz. It is capable of measuring power levels as low as -100dBm (0.1pW) and has a receiver dynamic range of 103dBm. The HP network analyzer can supply between +3dBm to -90dBm reference power at either of the two measurement ports. A photograph of the HP 8510 network analyzer can be seen in the figure below. The two port configuration of the HP network analyzer allowed the MIMO antenna input parameters to be measured simultaneously as each port was connected via a coaxial cable to one of the MIMO elements.

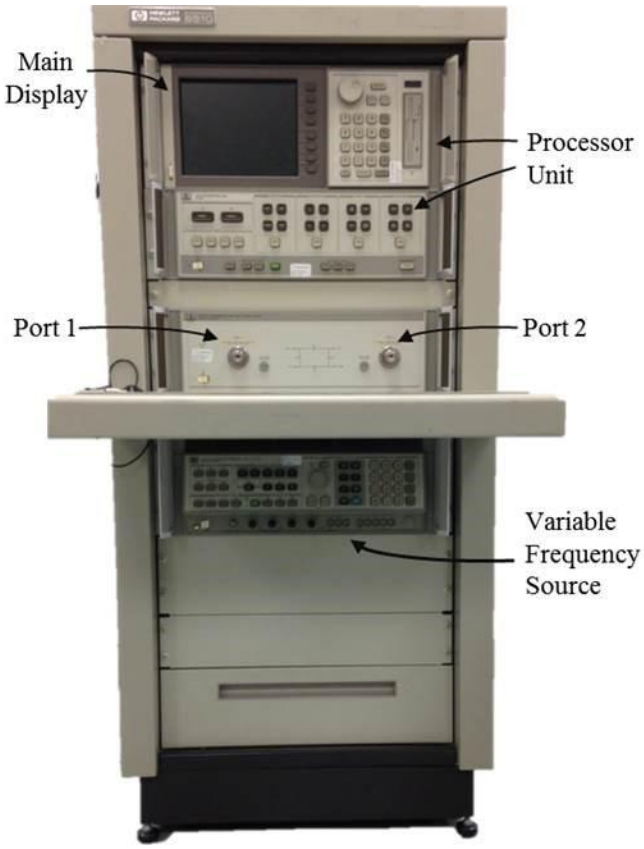

Figure III.3. Photograph of the HP 8510C network analyzer used for characterization

Calibration

In order for a network analyzer to provide highly accurate measurements, it had to undergo a calibration procedure to eliminate error within the measurement domain. The

calibration of a network analyzer is necessary since it is not possible to create perfect hardware and it would be impractical to design the hardware to high enough standards so that calibration is not needed. The calibration procedure measures errors from within the network analyzer as well as any external cables and adapters used in the measurement configuration. The calibration measurements represent systematic repeatable errors that can be mathematically corrected within the system so that the final results eliminate these errors. The common short, open, load and thru (SOLT) calibration technique was used on the HP network analyzer prior to the MIMO antenna characterization. Ideally the characteristic impedance of all components within the network analyzer and external coaxial cable is 50 Ω with no imaginary components, however in reality all of the connections and cables have some stray inductance and capacitance. The cumulative result of all components within the measurement domain can be accounted for via the various calibration standards. The open circuit standard gives a measurement result for the system capacitance. The short circuit standard will measure the system inductance, and the load standard accounts for how close the actual system is to the ideal 50 Ω . These three calibration standards are used to eliminate the return loss error at port 1 and port 2 (S_{11} and S_{22}).The isolation and transmission (S_{12} and S_{21}) errors are eliminated by connecting the two system ports together via the thru calibration standard. A mathematical model is then created within the system and which eliminates all of the mentioned errors so that very accurate and repeatable measurements can be recorded.

Anechoic Chamber

Network analyzer calibration is necessary in order to obtain reliable measurement data when characterizing any RF devices. When antenna measurements are involved, further steps must be taken to ensure the measurements are accurate which includes placing the antenna

within an anechoic chamber. The input parameters of an antenna represent the behavior when the antenna is radiating in free space, an environment that cannot be practically set up within a laboratory setting. Any objects nearby an antenna such as ceilings, walls, tables, network analyzers, and even feeding cables will cause power to be reflected back to the antenna thus interfering with the actual device measurements. An anechoic chamber replicates free space for the purposes of characterizing antennas because there are no objects for the radiated waves to reflect off of.

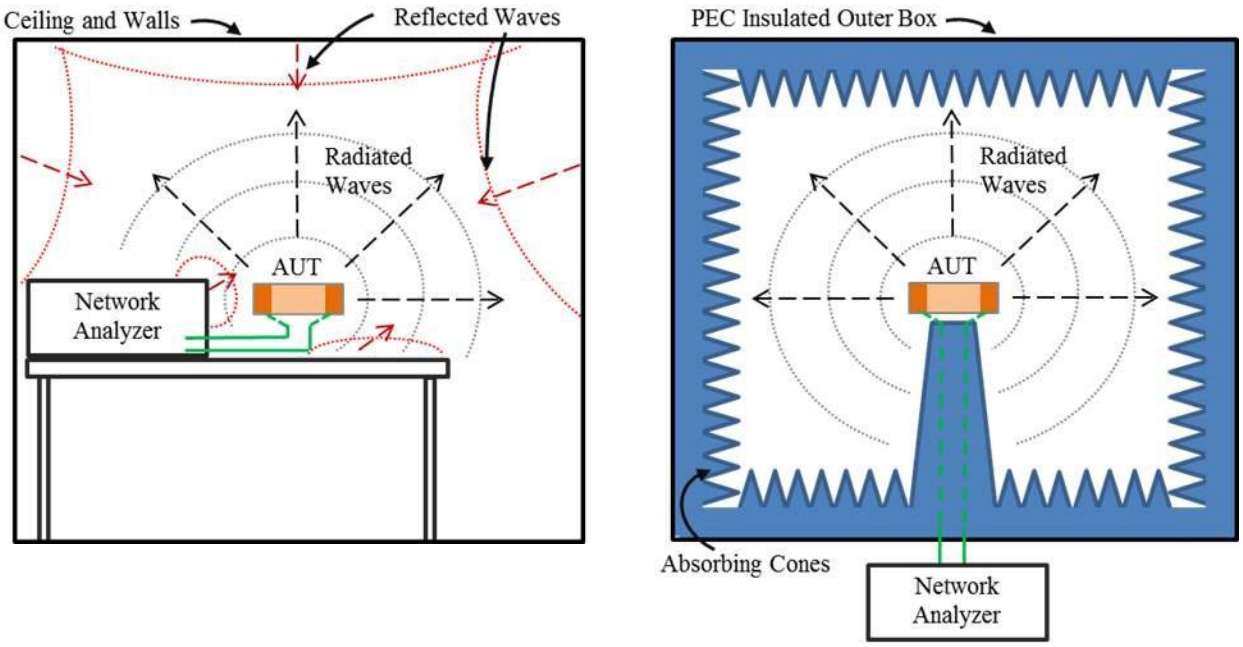

(*a*) Antenna on lab table in open air (*b*) Antenna inside anechoic chamber

Figure III.4. Input parameter measurement setup comparison

The anechoic chamber is essentially a fully enclosed metal box with insulting material lining the interior. No outside signals can interfere with measurements within the chamber since these signals cannot penetrate the outer perfect electric conductor (PEC) shell of the chamber. Inside the chamber large pyramidal cones are used to absorb any incident radiated waves. The insulating cones absorb power by converting the radiated energy to thermal energy. The cones are distinctly shaped so that the impedance seen by an incident wave does not discretely change

but slowly transitions from free space impedance to infinite impedance as the cones get thicker at the base. It is this slow continual impedance transformation that allows incident waves to be absorbed rather than reflected. Any external signals or noise as well as self-destructive interference were minimized by taking the input parameter measurements of the MIMO antenna inside the anechoic chamber.

The radiation pattern measurements of the MIMO antenna were also performed in the anechoic chamber, but featured an alternate configuration. When measuring radiation patterns the MIMO antenna under test (AUT) is placed on an elevated rotational stage at one end of the chamber and dual polarized horn antennas are setup at the other illustrated in Figure III.5.

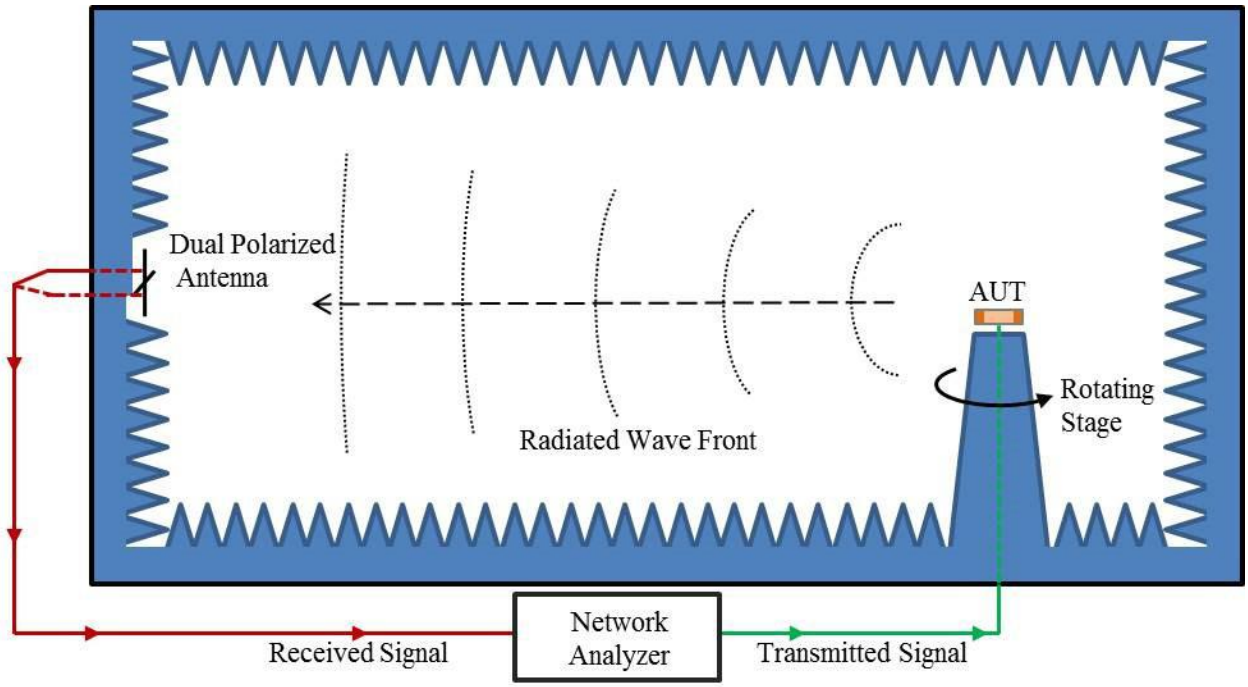

Figure III.5. Radiation pattern measurement setup inside anechoic chamber

The network analyzer transmits a signal via coaxial cable to excite the AUT and then the two perpendicularly polarized horn antennas independently measure a received signal. It is important that sufficient separation exists between the AUT and measurement horn antennas so that the horn is in the far field region of the AUT. Since the receiving antennas are setup in the far field

region, the incident radiated wave should be a plane wave consisting of an X polarization component and a Y polarization component. The total radiated power for each position is calculated as the summation of the vertical and horizontal polarization components. Measurements are recorded as the AUT is rotated so that a full 360° radiation pattern cross section results. The three main pattern cross sections were measured using this technique for each MIMO antenna element.

Photographs of the anechoic chamber used for the MIMO antenna measurements can be seen in Figure III.6-7 that shows the dual polarized horn antennas, and rotational stage; additionally the cone and wedge absorbers can be seen in the background.

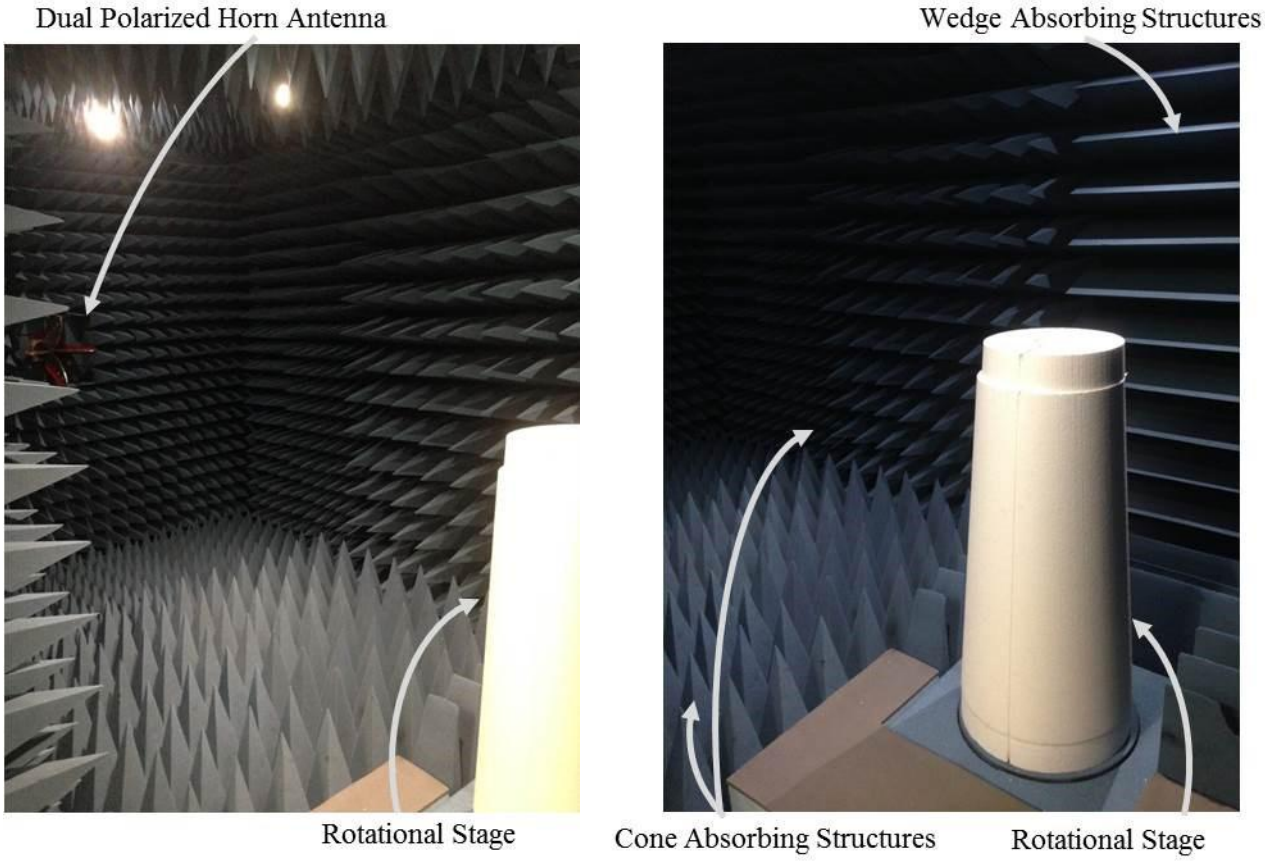

(*a*) Corner view of anechoic chamber (*b*) Rotational stage inside anechioc chamber

Figure III.6. Photographs of the rotational stage inside the anechoic chamber

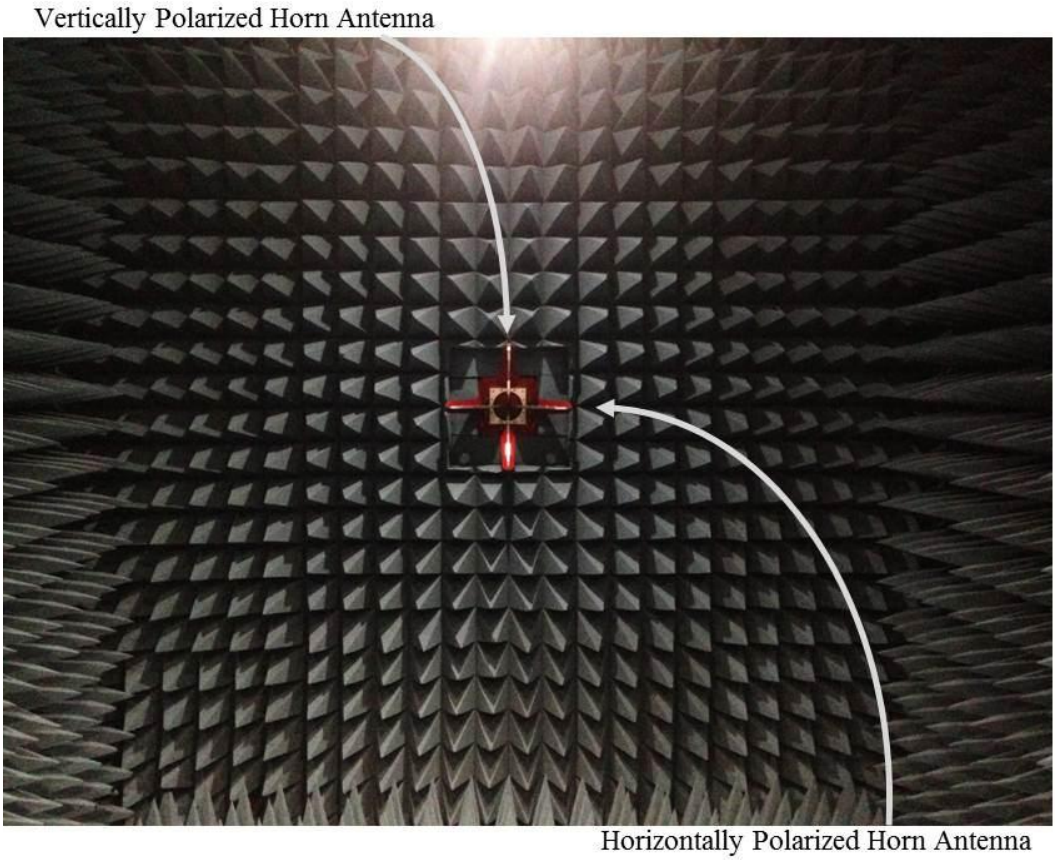

Figure III.7. Photograph of the dual polarized horn taken inside the anechoic chamber

Aside from the anechoic chamber and network analyzer, several precision coaxial cables were needed throughout the antenna characterization measurements. Traditionally coaxial cables consist of an inner conductor, an outer conducting shell, and a dielectric material like PTFE between the two; however precision coaxial transmission lines are air filled and do not have a typical dielectric between the two conductors. The air filled lines provide a higher level of fidelity since the electrical properties of air are much more consistent over time than that of manufactured artificial dielectrics such as PTFE. Along with the precision coaxial cables, many SMA adapters and precision adapters were used in the MIMO antenna characterization measurement process.

C. MIMO Antenna Characterization Results

Following the fabrication of the MIMO antenna, several measurements were taken to characterize the functional behavior of the antenna. The characterization methods and equipment previously discussed were implemented during this process. This section contains the measurement results of the MIMO antenna characterization along with comparisons to the simulated data shown in chapter 2.

Scattering Parameters

The four scattering parameters of the MIMO antenna (S_{11}, S_{12}, S_{21}, S_{22}) were measured from 500-6500 MHz in 15 MHz steps with a reference power level set to 0 dBm or 1 mW for each port. The measurement was setup inside of the anechoic chamber with the antenna placed on top of the rotational stage's foam pillar. Precision coaxial air filled lines were used to connect the AUT to the network outside of the chamber. Once the 8510C network analyzer reached a stable operating temperature, short-open-load-thru (SOLT) calibration was performed to correct for error within the system. Statistical averaging was used throughout the calibration procedure and while recording measurements. The averaging was set to ×4096; meaning at every 15 MHz step the corresponding S-parameter values (S_{11}, S_{12}, S_{21}, S_{22}) represented an average of 4096 individual measurements. Averaging the results in this manor helped eliminate random noise and provided a more precise result of the scattering parameters. Both antenna elements measured reflection coefficients as well as the isolation parameter are shown on the standard log scale in Figure III.8. Once again the major LTE, WLAN and WMAN bands are displayed in the background to provide an idea of the overall spectrum that is covered. The recorded measurements were also plotted against the simulated results in Figure III.9-11 so that clear distinctions can be seen. These comparison figures show the four major operating regions plotted

and labeled in the background as calculated from the 6-dB return loss bandwidth of the measured results.

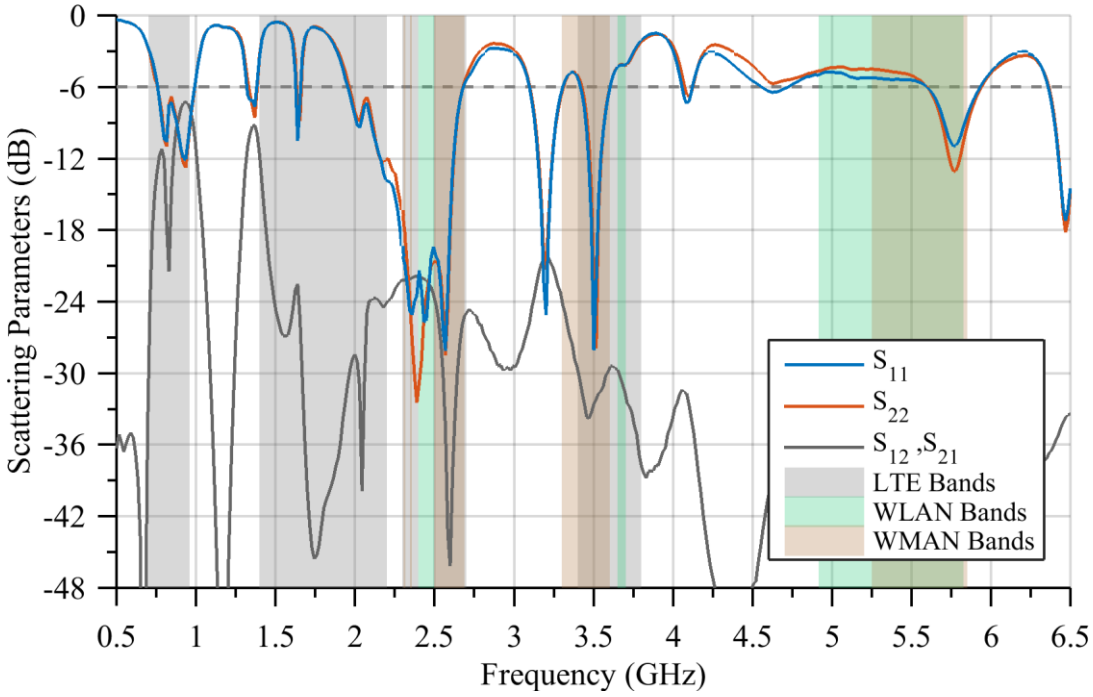

Figure III.8. Measured MIMO antenna scattering parameters

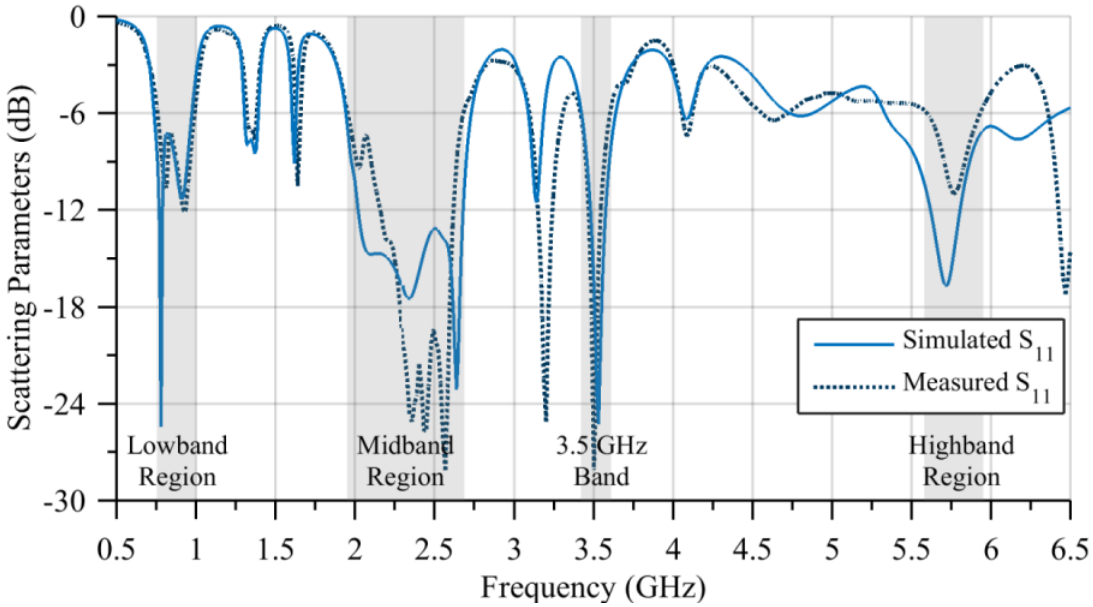

Figure III.9. Comparison of measured and simulated S_{11}

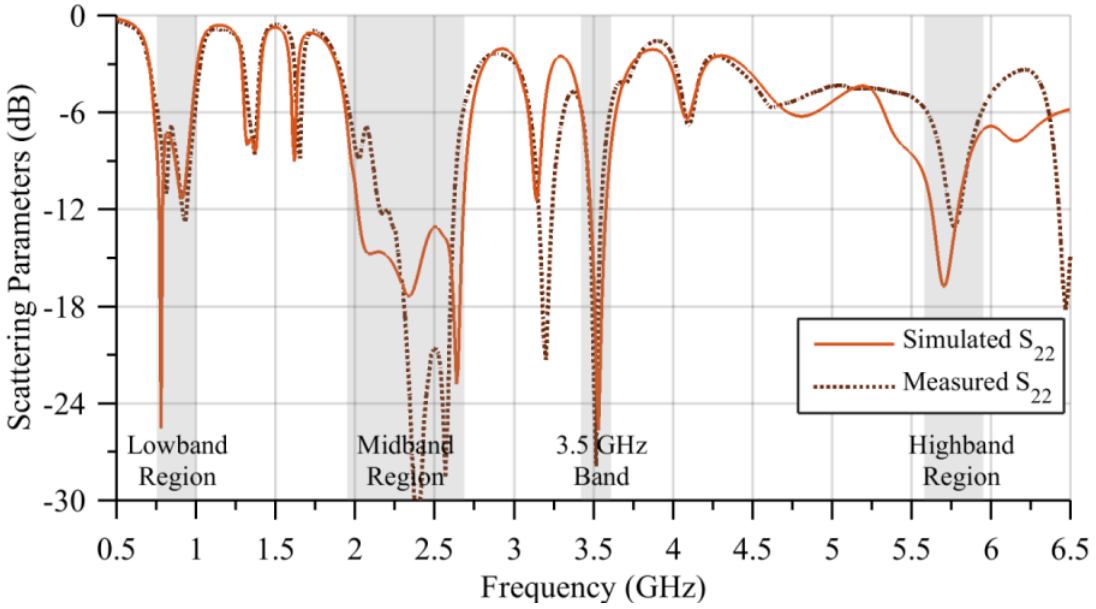

Figure III.10. Comparison of measured and simulated S_{22}

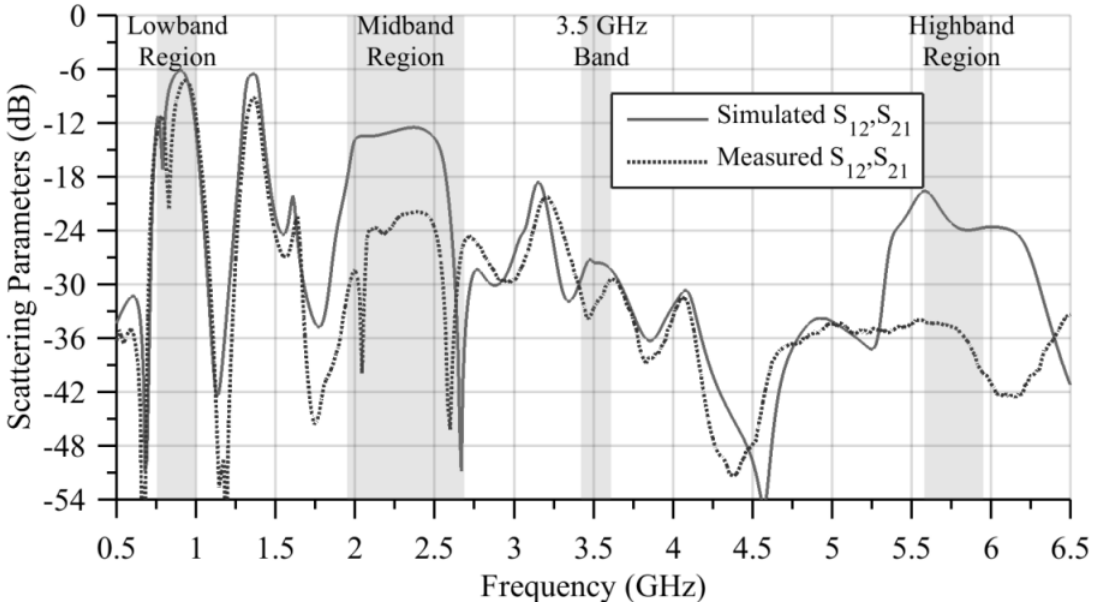

Figure III.11. Comparison of measured and simulated $S_{12,}$ S_{21}

Observing the results, it is first noticed that the return loss for both antennas show very similar behavior as expected since the two radiating elements are geometrically identical aside from a mirrored ground plane. Although slight variations between the two elements exist, their

bandwidth and operational regions are nearly equal. The lowband region of operation meets or exceeds the 6-dB return loss criteria for both antenna elements from 755 MHz to 995 MHz; a 240 MHz bandwidth. This shows operation across LTE bands 5, 6, 8, 13, 14, 18, 19, 20, 26, 27, 28, 44. The lowband isolation reaches a peak value close to -7.5dB at 935 MHz confirming that there is some correlation in this region however the ECC will provide more insight into how much this will affect the lowband MIMO performance. The only observable discrepancy between the measured and simulated results in the lowband is the peaked -24 dB return loss at 780 MHz in the simulated results. This sharp region in the simulation results had a bandwidth of less than 15 MHz meaning the results that were taken in 15 MHz step sizes may not have recorded this narrow bandwidth region explaining the inconsistency.

The midband 6-dB operating region starts at 1.95 GHz and extends through 2.69 GHz. The midband region shows good return loss across the common Wi-Fi 2.5 GHz WLAN band, the 2.3 GHz and 2.5 GHz WiMAX WMAN bands as well as LTE bands 1, 7, 23, 30, 34, 36, 38, 40, 41. Isolation throughout the midband should correspond to low correlation between elements based on the initial observation of the peak isolation parameter, -22 dB at 2.4 GHz. This region shows areas where the measured reflection coefficient was more than 10 dB less than the simulated; however considering the maximum deviations occur in regions less than -15 dB, in reference to the incident power levels the results actually show less than 3 % difference.

Additionally the 3.5 GHz region shows a 6-dB return loss operating bandwidth of 190 MHz from 3.42-3.61 GHz with an isolation parameter peak value of -30 dB at 3.61 GHz. This region covers LTE frequency bands 22, 42 and 43 as well as the 3.5 GHz WiMAX WMAN band. Both elements show a measured peak reflection coefficient of around -25 dB at 3.515 GHz, which is less than a 0.5 % deviation from the simulated resonant frequency in this region.

All isolation parameters, measured and simulated in the 3.5 GHz band are less than -26 dB indicating such a low value that the measured differences are irrelevant to the correlation and performance of the MIMO antenna.

The measured highband region of operation for the MIMO antenna, 5.58-5.95 GHz, showed the most inconsistent behavior compared to the simulated results. While this 370 MHz bandwidth still covers many 5 GHz WLAN and WMAN channels, the simulated antenna displayed over 1000 MHz bandwidth. Measurement results had a peak isolation parameter -34.4 dB at 5.67 GHz which is much lower than the simulated values however once again, overall these values are so low compared to the reference that the difference between simulation and measurement is not relevant.

Radiation Patterns

Upon completing the scattering parameters measurements, the radiation pattern cross sections were recorded. Once again using the setup shown previously shown, the antenna was placed on the rotational stage inside the anechoic chamber, adjusting the orientation three times in order to measure the main cross sections. For this measurement setup the network analyzer was set to source its maximum power of +3 dBm. Since the dynamic range of the network analyzer is over 100 dBm no external amplifiers were needed for measurements. Post processing of the raw pattern power measurements was done to normalize the data to the maximum power value recorded for each frequency. The patterns were measured at 850 MHz, 2.5 GHz, 3.5 GHz, and 5.7 GHz so that the radiated behavior for each main operating region of the antenna could be observed. Figures III.12-23 show the measurement results of the fabricated antenna plotted along with the simulation results from the MIMO model that featured lumped ports shown in Figure II.26.

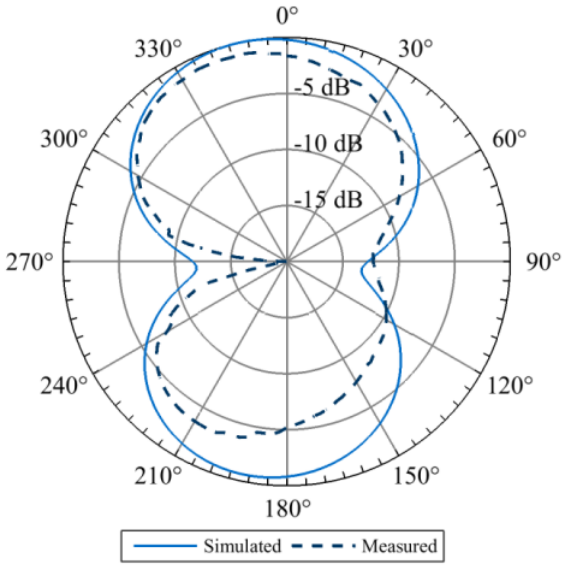

(*a*) Antenna element 1

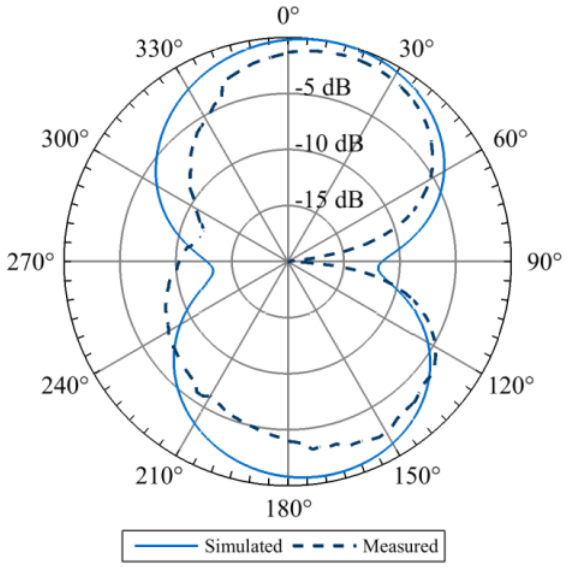

(*b*) Antenna element 2

Figure III.12. X-Y cross section measured radiation patterns at 850 MHz

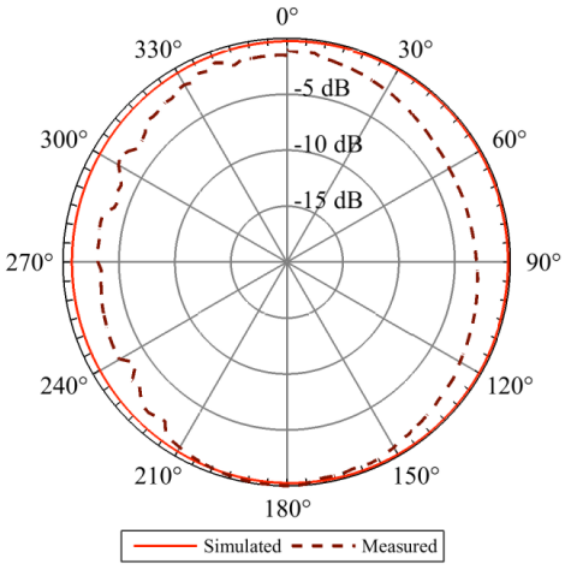

(*a*) Antenna element 1

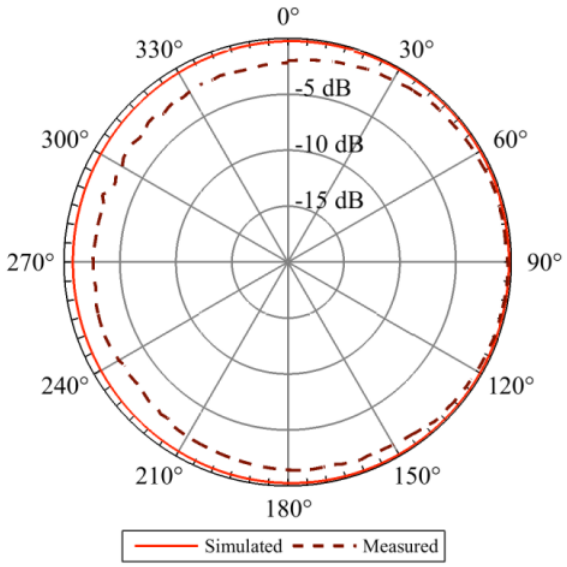

(*b*) Antenna element 2

Figure III.13. X-Z cross section measured radiation patterns at 850 MHz

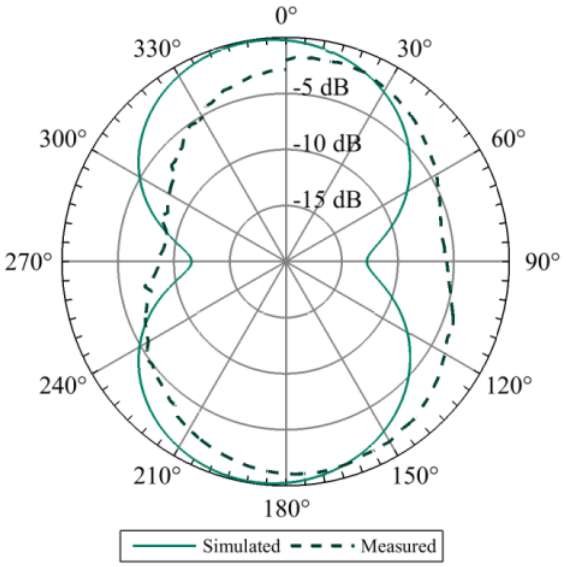

(*a*) Antenna element 1

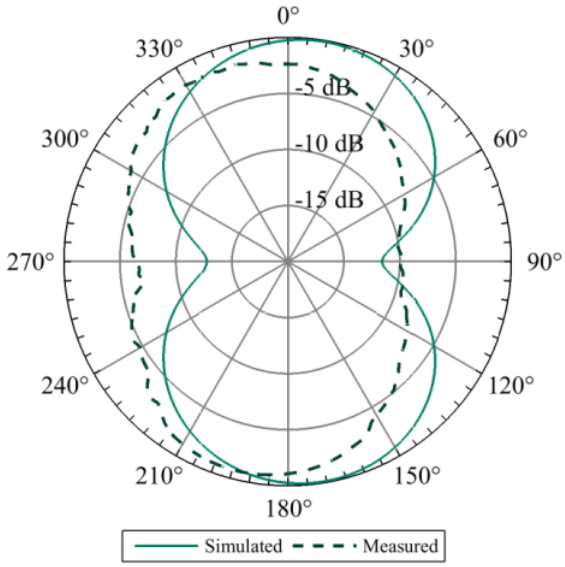

(*b*) Antenna element 2

Figure III.14. Z-Y cross section measured radiation patterns at 850 MHz

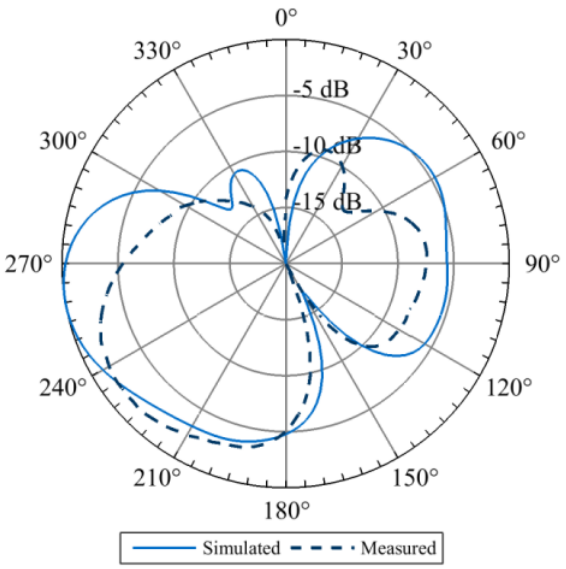

(*a*) Antenna element 1

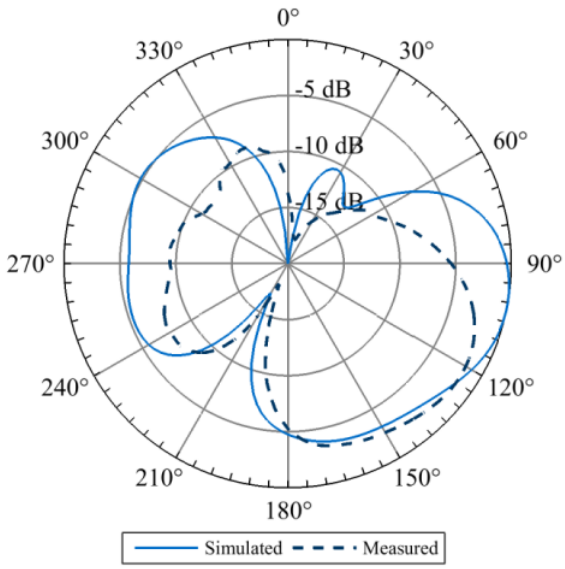

(*b*) Antenna element 2

Figure III.15. X-Y cross section measured radiation patterns at 2500 MHz

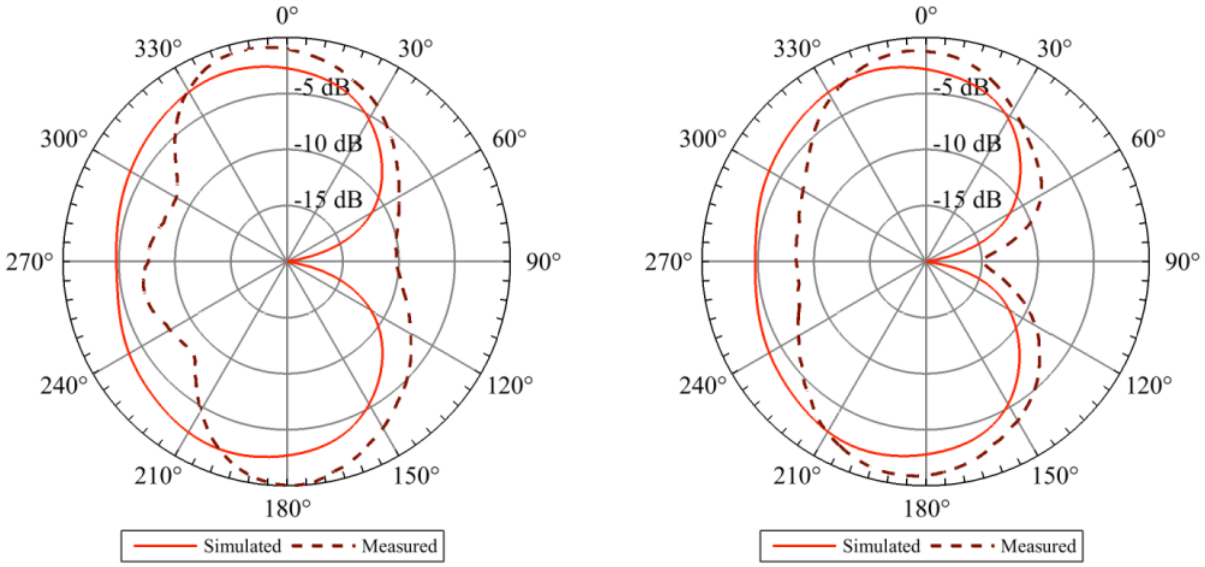

(*a*) Antenna element 1 (*b*) Antenna element 2

Figure III.16. X-Z cross section measured radiation patterns at 2500 MHz

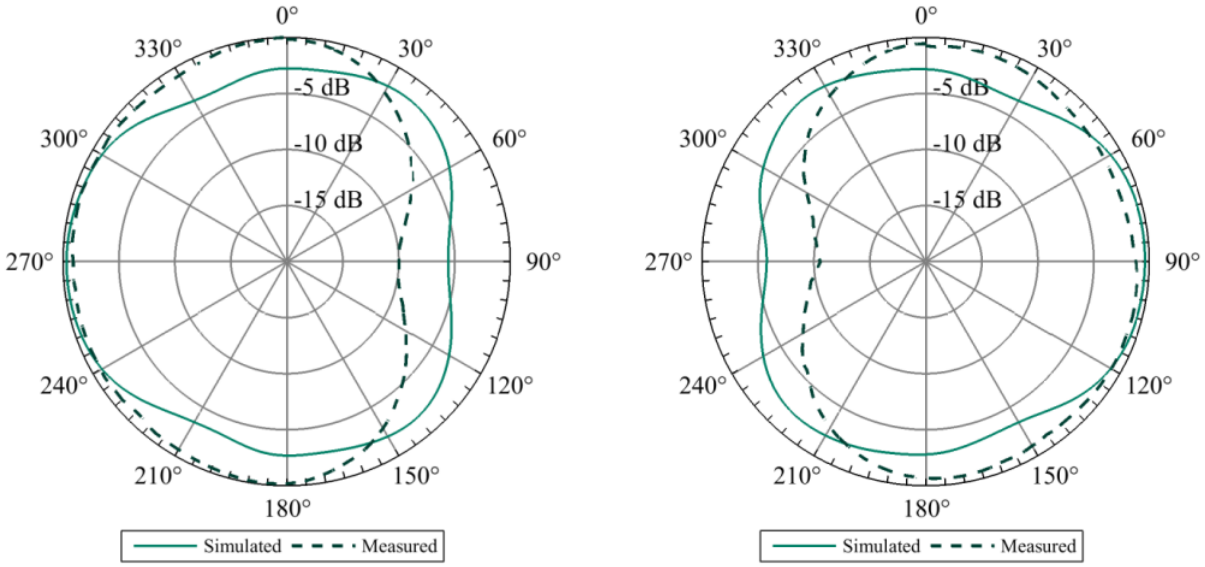

(*a*) Antenna element 1 (*b*) Antenna element 2

Figure III.17. Y-Z cross section measured radiation patterns at 2500 MHz

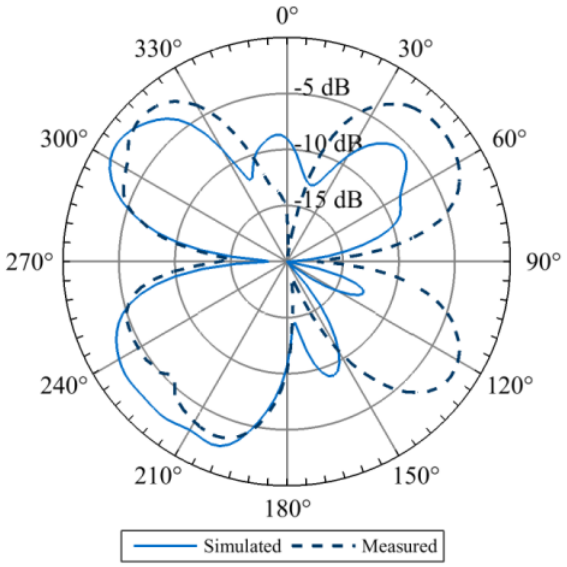

(*a*) Antenna element 1

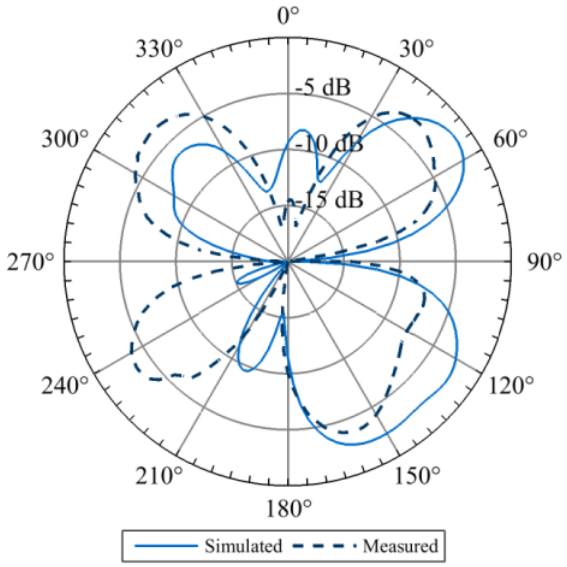

(*b*) Antenna element 2

Figure III.18. X-Y cross section measured radiation patterns at 3500 MHz

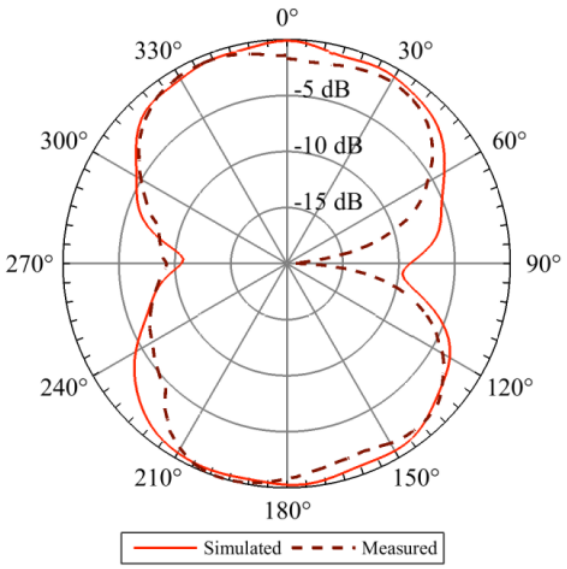

(*a*) Antenna element 1

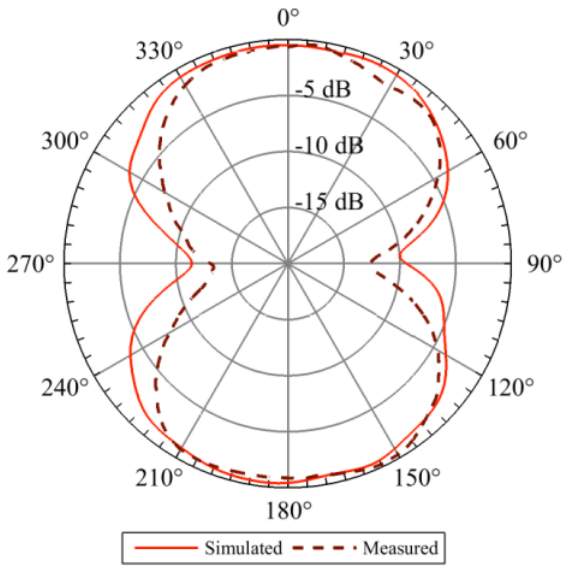

(*b*) Antenna element 2

Figure III.19. X-Z cross section measured radiation patterns at 3500 MHz

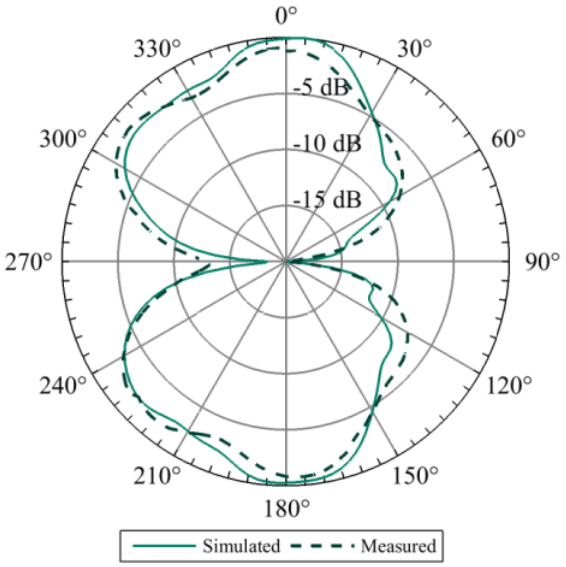

(*a*) Antenna element 1

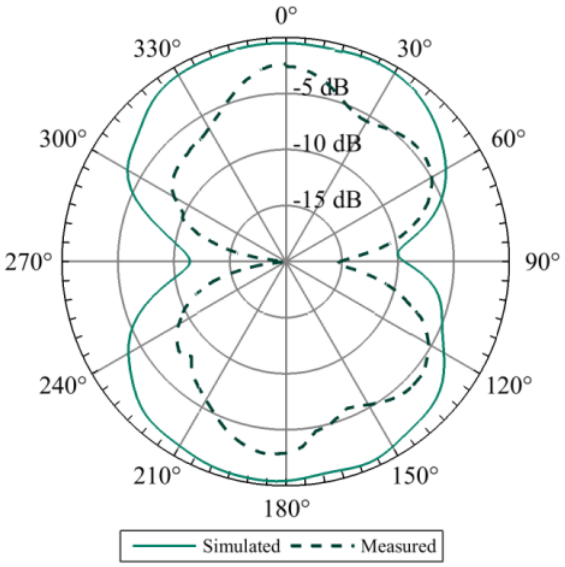

(*b*) Antenna element 2

Figure III.20. Y-Z cross section measured radiation patterns at 3500 MHz

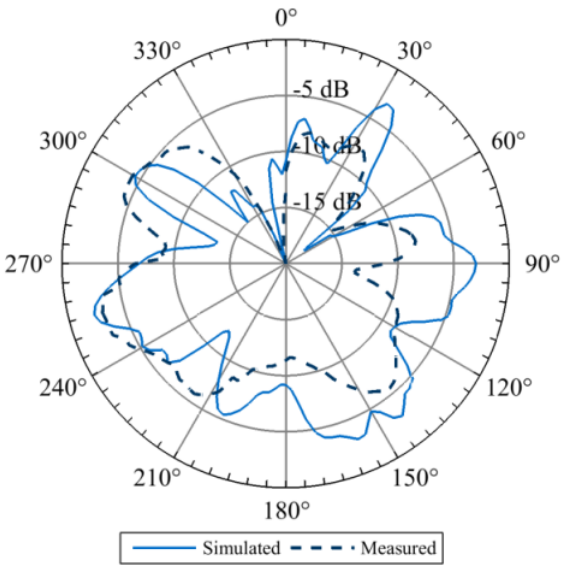

(*a*) Antenna element 1

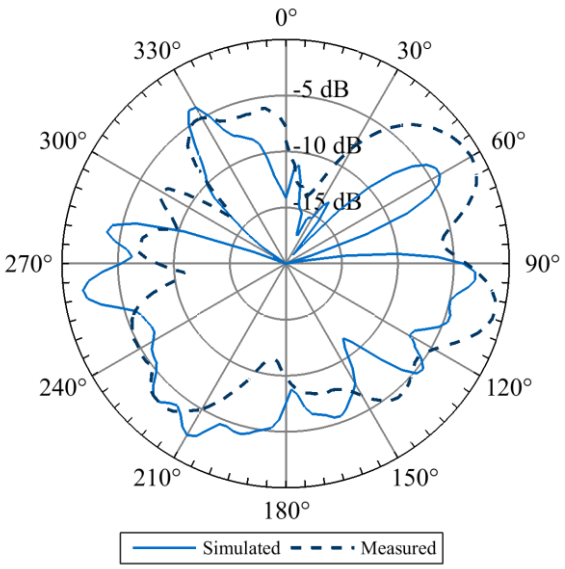

(*b*) Antenna element 2

Figure III.21. X-Y cross section measured radiation patterns at 5700 MHz

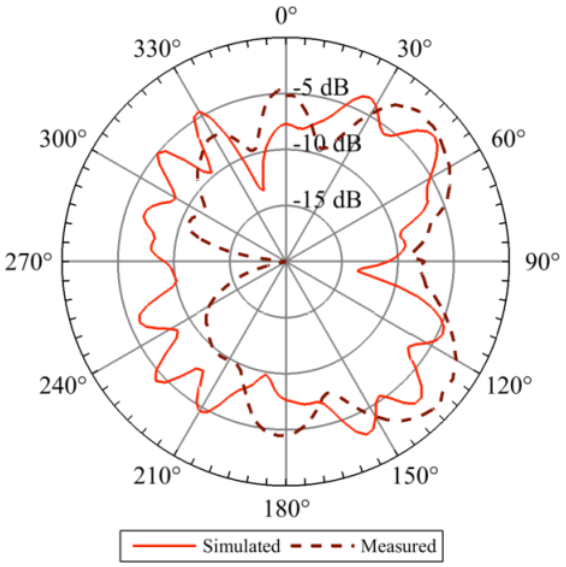

(*a*) Antenna element 1

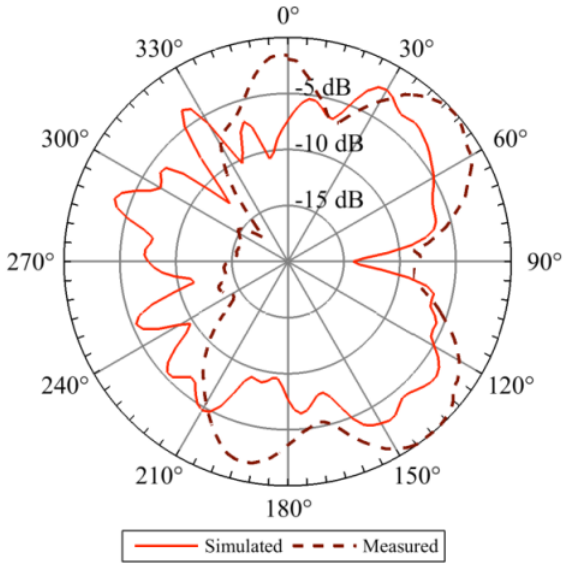

(*b*) Antenna element 2

Figure III.22. X-Z cross section measured radiation patterns at 5700 MHz

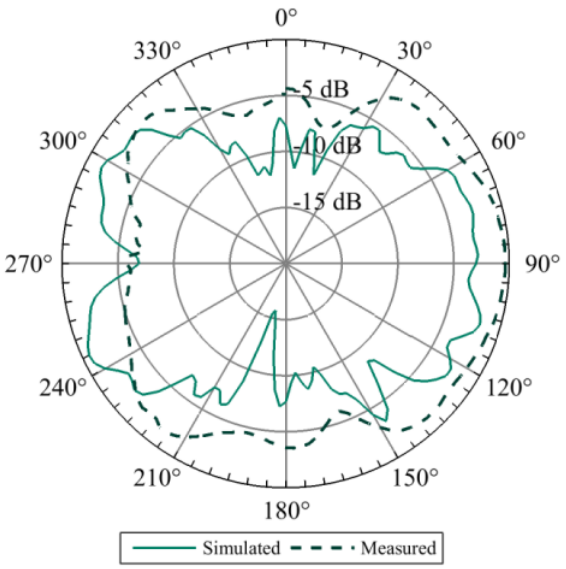

(*a*) Antenna element 1

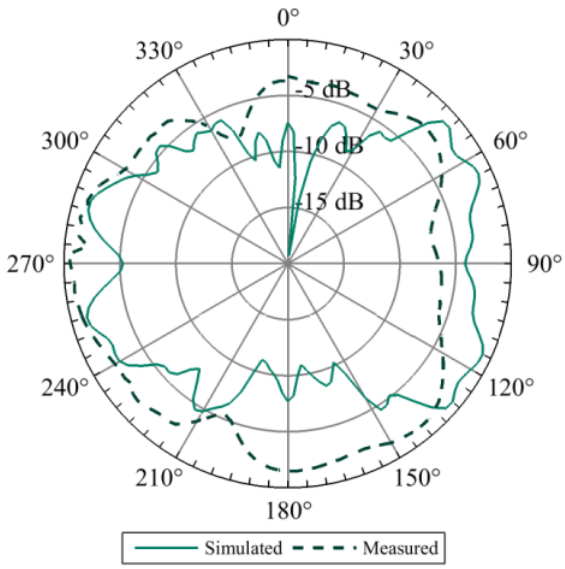

(*b*) Antenna element 2

Figure III.23. Y-Z cross section measured radiation patterns at 5700 MHz

The measured 850 MHz pattern cross sections show the characteristic doughnut shaped radiating behavior that was simulated. Some differences arise near the null area in the X-Y cut where the power measured was significantly less, however aside from these small areas the measured pattern is consistent with the simulated results. The X-Z cross section at 850 MHz shows exactly the omnidirectional behavior desired for the antenna, where both elements measured less than 4dB deviation from the simulated results. It is observed from the Z-Y pattern that the measured antenna has less distinct nulls at 90° and 270° which is possibly a phenomenon caused by surface currents on the soldered coaxial ground leads.

The radiation patterns of the fabricated MIMO antenna at 2500 MHz were also in good agreement with the simulated antenna. As expected from the simulations the three dimensional pattern is orthogonal to the 850 MHz pattern, due to different components conducting the surface currents. Overall each cross section at 2500 MHz follows the simulated model behavior and exhibits a strong non-directional properties.

Radiation pattern cross sections at 3.5 GHz and 5.7 GHz begin to show more of the interference due to the various conductive traces on each element. Comparing the measured and simulated results in these regions becomes slightly more challenging however in most cases the peaks and valleys of the patterns occur in similar areas and the magnitudes are relatively equivalent. Discrepancies in the higher frequency patterns are more difficult to specifically diagnose.

Additionally the measured radiation patterns are plotted along with the simulation results from the model that included the physical coaxial cable in all simulations. This simulation model better represents the fabricated antenna and since the coaxial cable is present in the model. The results are shown below in Figures III.24-35.

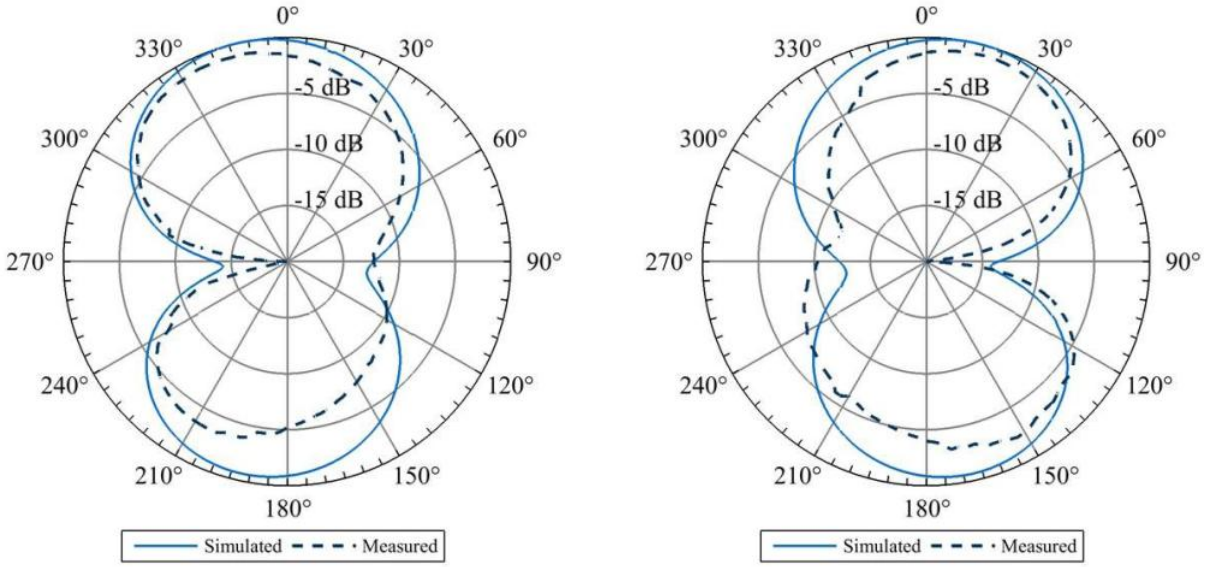

(*a*) Antenna element 1 (*b*) Antenna element 2

Figure III.24. X-Y cross section measured radiation patterns at 850 MHz plotted against simulated results with coaxial cable included

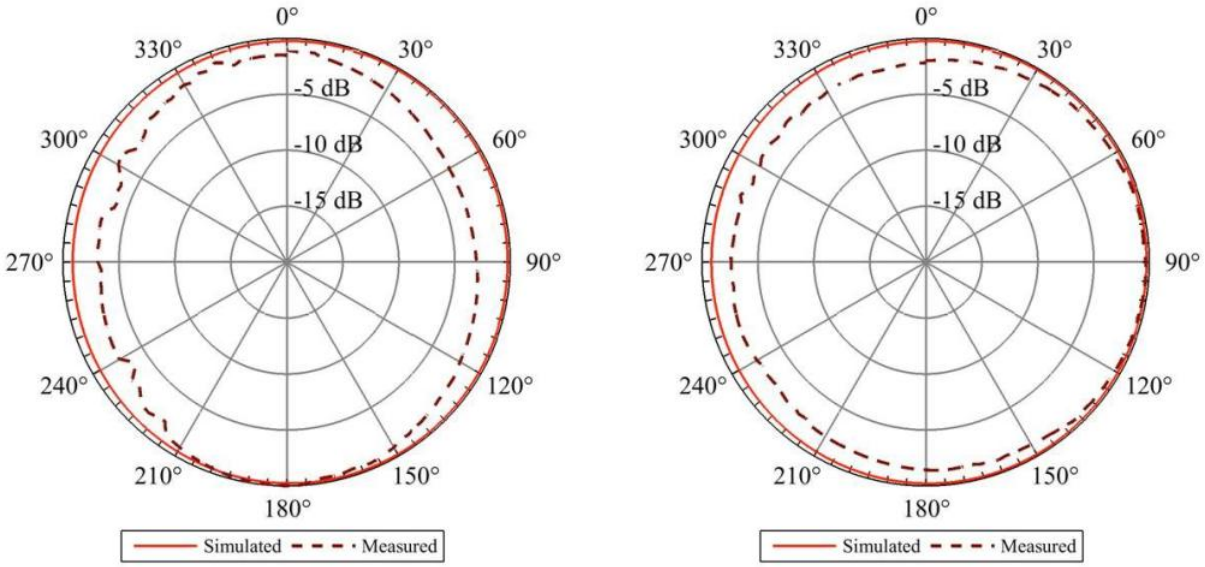

(*a*) Antenna element 1 (*b*) Antenna element 2

Figure III.25. X-Z cross section measured radiation patterns at 850 MHz plotted against simulated results with coaxial cable included

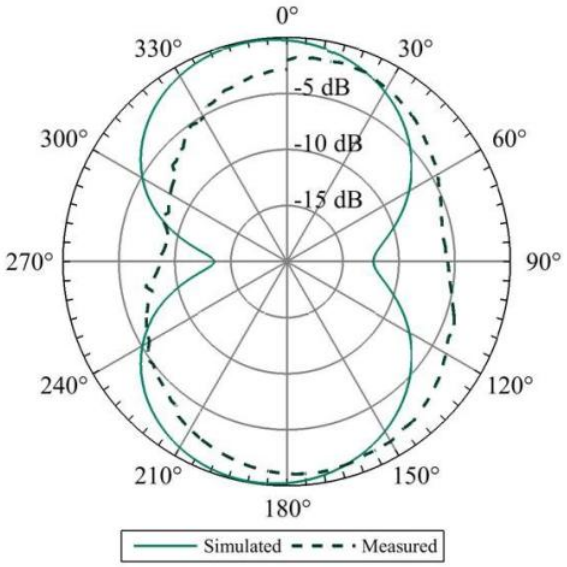

(*a*) Antenna element 1

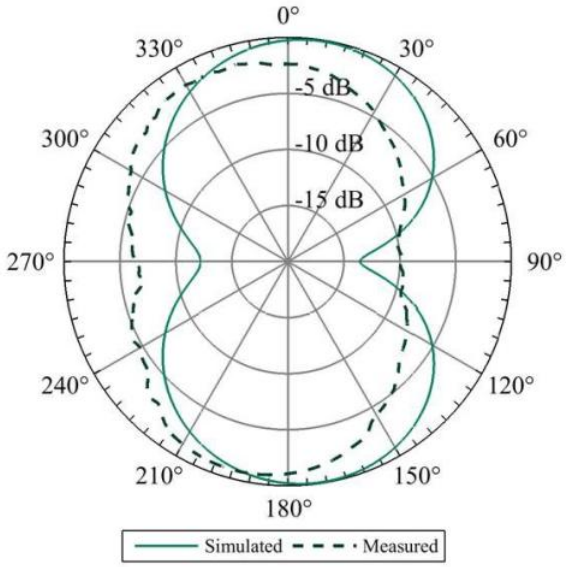

(*b*) Antenna element 2

Figure III.26. Z-Y cross section measured radiation patterns at 850 MHz plotted against simulated results with coaxial cable included

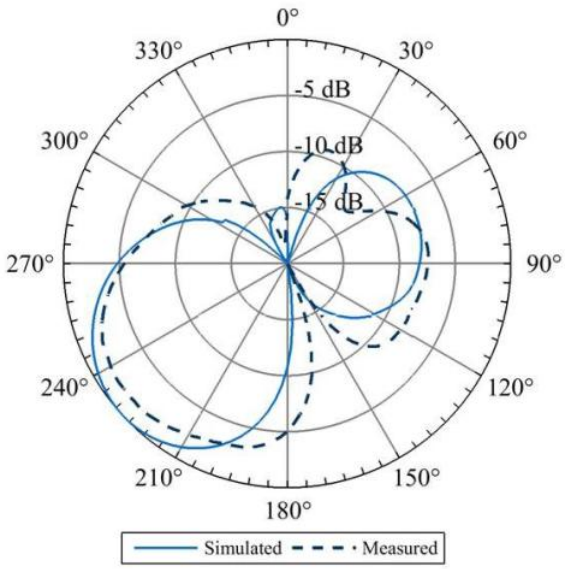

(*a*) Antenna element 1

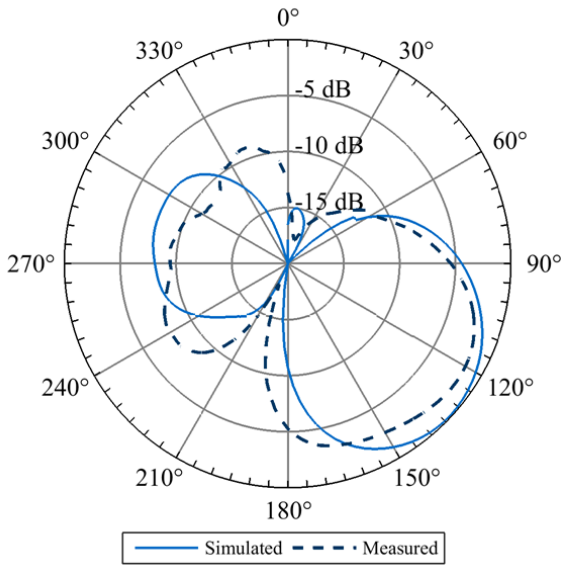

(*b*) Antenna element 2

Figure III.27. X-Y cross section measured radiation patterns at 2500 MHz plotted against simulated results with coaxial cable included

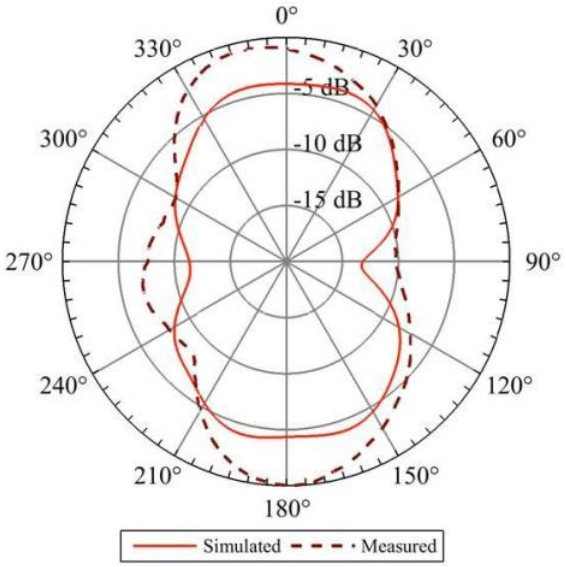

(*a*) Antenna element 1

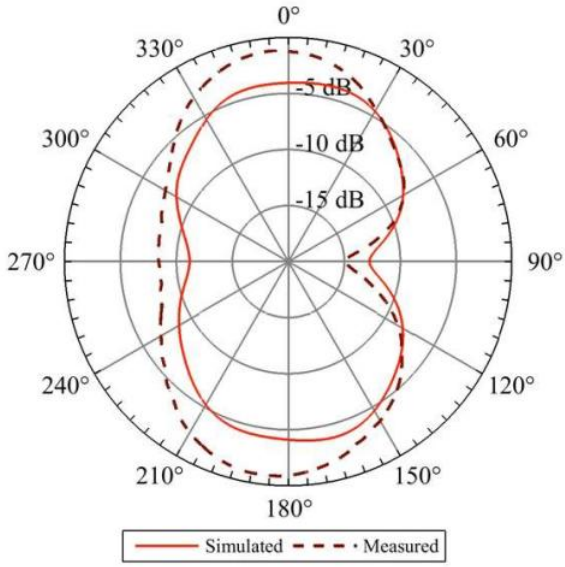

(*b*) Antenna element 2

Figure III.28. X-Z cross section measured radiation patterns at 2500 MHz plotted against simulated results with coaxial cable included

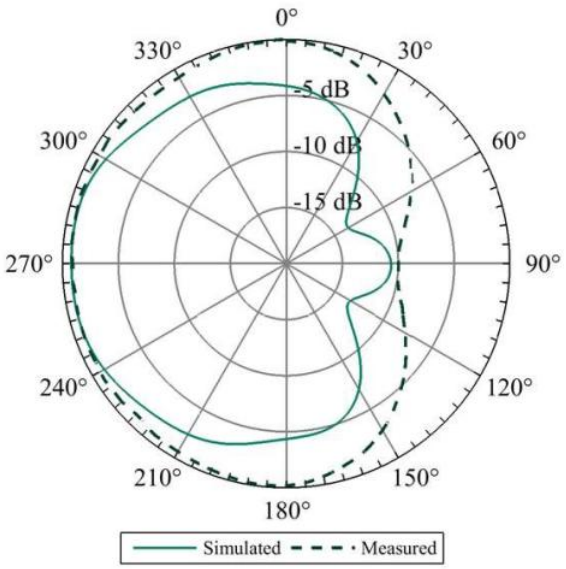

(*a*) Antenna element 1

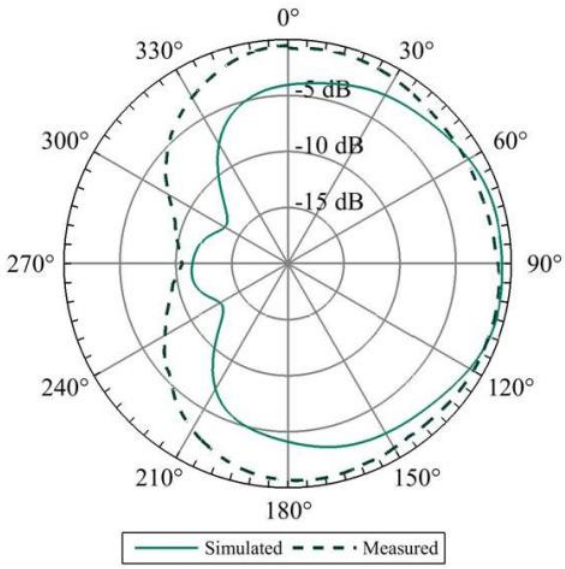

(*b*) Antenna element 2

Figure III.29. Y-Z cross section measured radiation patterns at 2500 MHz plotted against simulated results with coaxial cable included

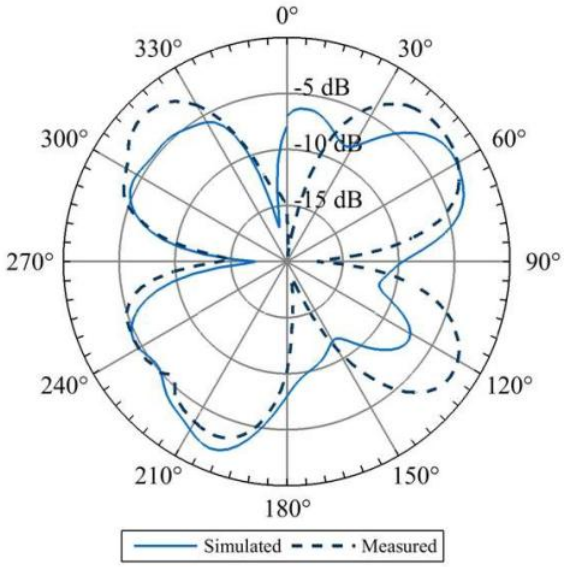

(*a*) Antenna element 1

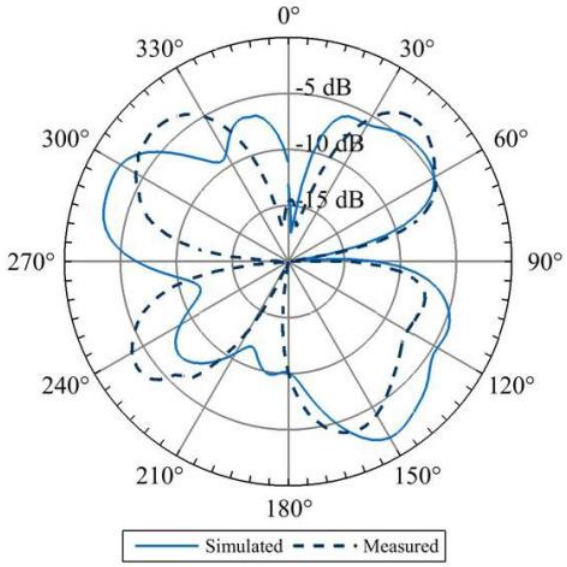

(*b*) Antenna element 2

Figure III.30. X-Y cross section measured radiation patterns at 3500 MHz plotted against simulated results with coaxial cable included

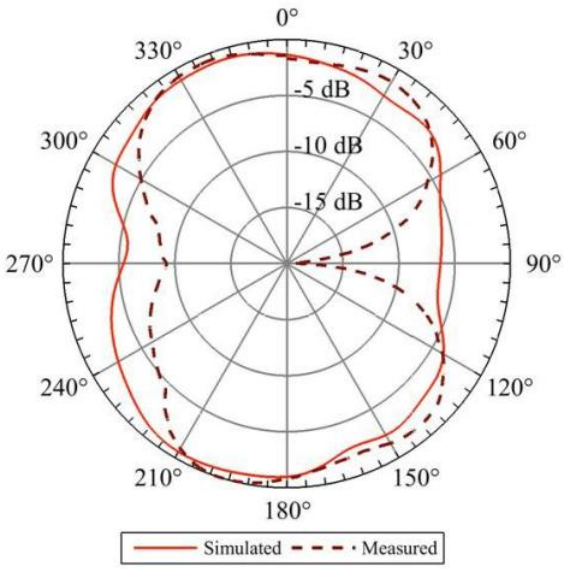

(*a*) Antenna element 1

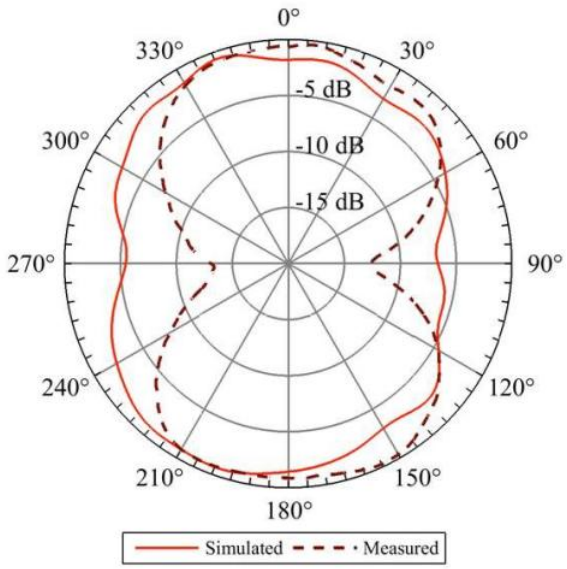

(*b*) Antenna element 2

Figure III.31. X-Z cross section measured radiation patterns at 3500 MHz plotted against simulated results with coaxial cable included

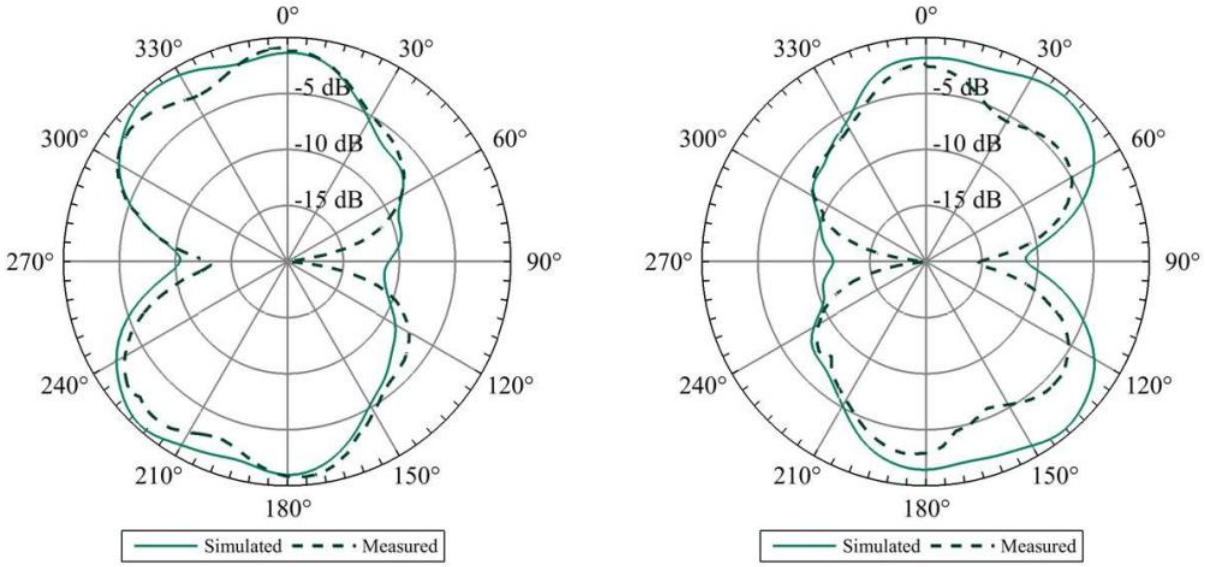

(*a*) Antenna element 1 (*b*) Antenna element 2

Figure III.32. Y-Z cross section measured radiation patterns at 3500 MHz plotted against simulated results with coaxial cable included

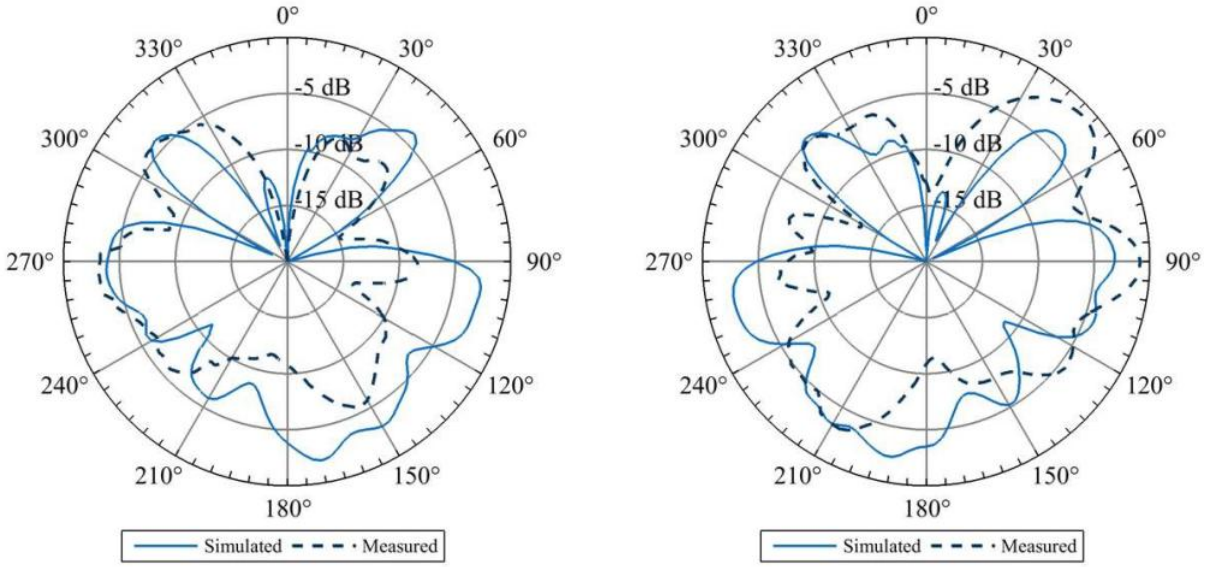

(*a*) Antenna element 1 (*b*) Antenna element 2

Figure III.33. X-Y cross section measured radiation patterns at 5700 MHz plotted against simulated results with coaxial cable included

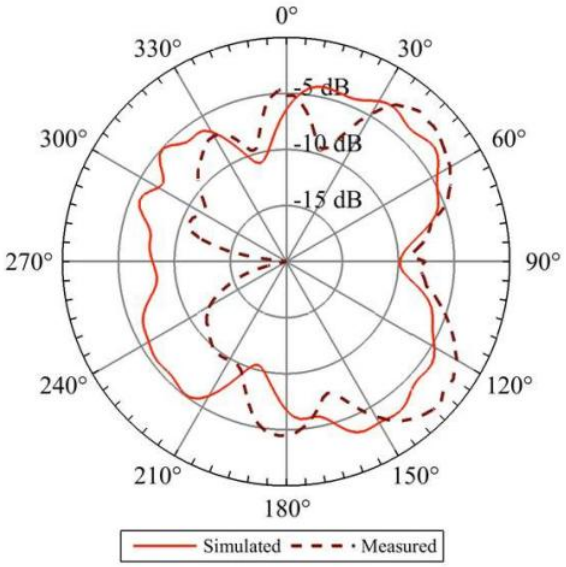

(*a*) Antenna element 1

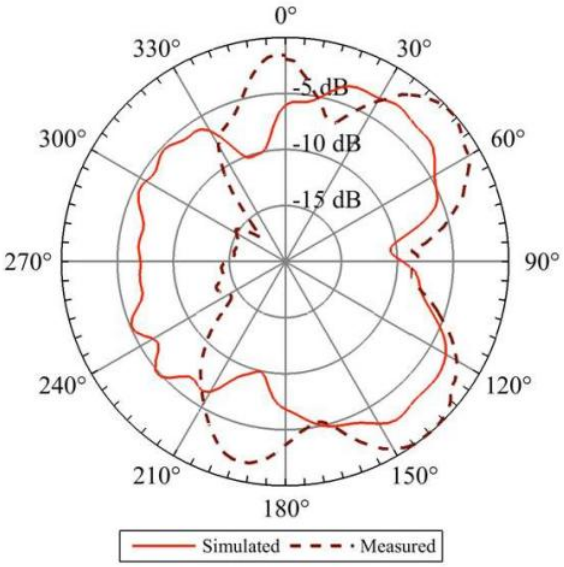

(*b*) Antenna element 2

Figure III.34. X-Z cross section measured radiation patterns at 5700 MHz plotted against simulated results with coaxial cable included

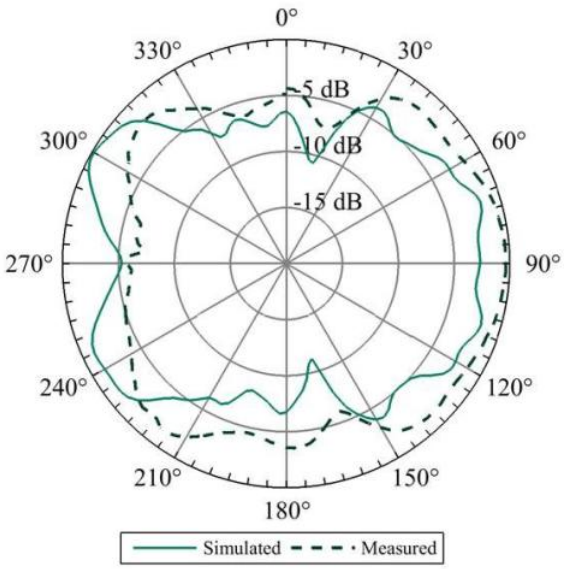

(*a*) Antenna element 1

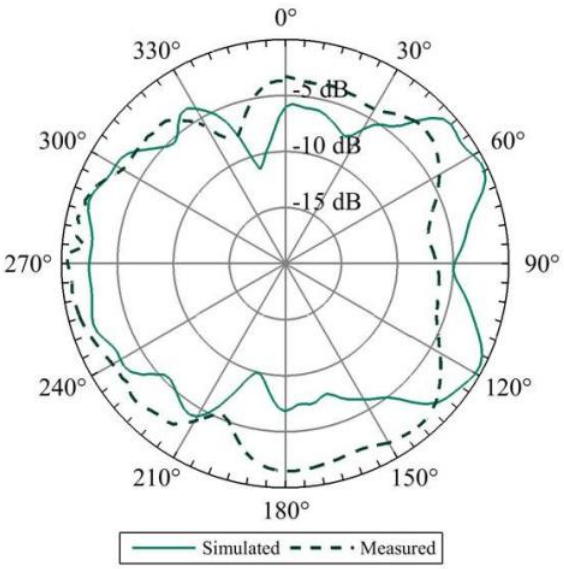

(*b*) Antenna element 2

Figure III.35. Y-Z cross section measured radiation patterns at 5700 MHz plotted against simulated results with coaxial cable included

Envelope Correlation Coefficient

Taking the measured complex scattering parameter values, the envelope correlation coefficient was calculated using Eq. I.11. The results can be seen in Figure III.36 below, which displays both the simulated and measured ECC values with the 6-dB operating regions shaded in the background.

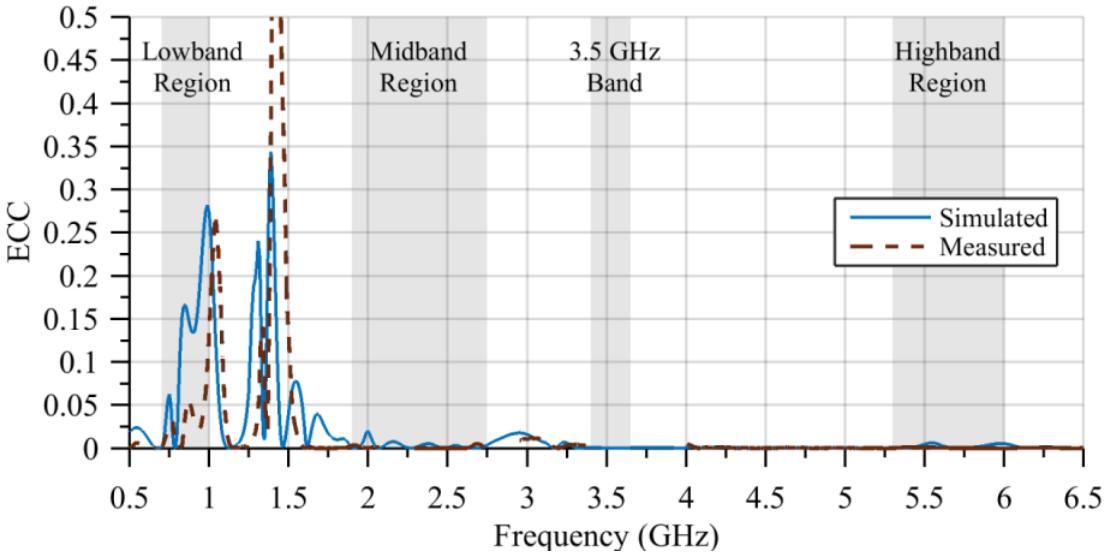

Figure III.36. Measured envelope correlation coefficient for MIMO antenna

As previously discussed, a MIMO system is not efficient if the individual elements have a strong correlation, thus the lower ECC values correspond to a greater system diversity. MIMO antennas for mobile communication are considered diverse and advantageous when the ECC values are less than 0.5. The measured results show a peak ECC value greater than 0.5 at 1480 MHz however since this value resides outside of the operating regions, it does not negatively affect the performance of the MIMO antenna. The measurements showed much lower than 0.5 ECC throughout all regions of operation. As expected from the isolation parameters, the lowband shows the highest correlation with a maximum ECC value of 0.25. Aside from the small peak at the 1 GHz edge of the lowband the ECC values calculated across all other operating regions are

very low, much less than the 0.5 metric set forth in the literature. This proves the MIMO antenna is behaving as desired with each element contributing a diverse signal.

D. Discussion of Measured Results

The use of common cost effective materials along with the simple geometries and single layer uniplanar design allowed the MIMO antenna be fabricated in house. An Accurate CNC 427 milling machine was used to etch the designed antenna structure and the coaxial test leads were hand shaped and soldered onto the antennas ground plane. Reflecting the original goals, the antenna fabrication and assembly was an easy process, which represents a desirable practical quality for mobile communication antennas. Using an HP 8510C network analyzer and ETS-Lindgren anechoic chamber, the fabricated antenna was characterized to the fullest extent given the available equipment. Specific care was taken to properly calibrate the system and along with point averaging; highly repeatable and accurate measurements were recorded to characterize the MIMO antenna.

The measured scattering parameters clearly showed 6-dB return loss regions for the lowband, midband, 3.5 GHz region, and highband with 240 MHz, 740 MHz, 190 MHz, and 370 MHz respectively. The computational HFSS antenna simulations modeled the actual behavior of the MIMO antenna well. Overall return loss followed the predicted model closely, with the most deviation occurring at the higher frequencies. The most significant discrepancies between the simulation and measurement results was likely caused by two sources. The two coaxial feeding lines that were soldered to the ground plane likely had the most effect the small deviations in radiation patterns which can be most clearly seen in the lowband 850 MHz cross sections. Although the measured patterns results was not exactly as modeled, the overall trend was still consistent and favored an omnidirectional behavior. The other possible source for error was

likely the inconsistency of the FR4 material used. Since this material was chosen due to its availability and low cost, the permittivity and loss tangents were not fully provided by the manufacturer and only a 1 GHz value was given which was set to be constant in the simulated models. In reality the permittivity is a frequency dependent value which can deviate as much as 5% across the given frequency range. Despite the small sources of error the MIMO antenna showed good multiband behavior and low correlation across the operating spectrum in alignment with the original goals set forth in Chapter 1 of this thesis.

IV. Summary and Conclusion

The focus of this work was to design a multiband uniplanar MIMO antenna for hand-held mobile communication devices on LTE, WLAN, and WMAN networks. The antenna design methodology outlined in this thesis combined many broadbanding techniques from the literature and resulted in a hybrid style antenna that featured a direct-fed monopole, multiple parasitic elements and a couple-fed meander C-shaped monopole. The optimized single antenna design was evolved into a two element MIMO antenna that retained a 115×55×1.54 mm sized substrate in which each element occupied 15×55×1.54 mm.

Simulation results of the MIMO antenna featured greater than 6-dB return loss across much of the LTE spectrum, completely covering the 2.5 GHz WLAN band, 2.3 GHz and 2.5 GHz WMAN bands and 19 individual LTE bands; additionally the antenna partially covering another 12 LTE bands, and many 5 GHz WLAN and WMAN channels. The simulated lowband radiation efficiency out preformed many similar sized multiband LTE antennas from the literature and showed an envelope correlation coefficient of less than 0.28 from 750-1000 MHz with efficiencies as high as 63%. Outside of the lowband, the simulated antenna exhibited radiation efficiencies ranging from 50-85% across 6-dB return loss regions from 1940-2740 MHz, 3420-3640 MHz, and 5330-6430 MHz with correlation coefficients all less than 0.02. The radiation patterns of the simulated antenna across the four major operating regions all showed non-directional behavior further indicated that the designed antenna would be suitable in a wireless communication application.

The MIMO antenna model was designed using single layer FR4 and featured geometrically simple elements which allowed for the model to be easily fabricated on site. The antenna was etched using an Accurate CNC 427 milling machine and coaxial test leads were

soldered onto the board so that the antenna could be interfaced with an SMA connector. The characterization of the fabricated antenna took place inside a fully enclosed anechoic chamber in which the antenna was connected to an HP8510C network analyzer via precision coaxial air lines. Complex four port scattering parameters and radiation pattern cross section measurements of the antenna were recorded.

Several distinguishable 6-dB operating regions were evident in the measurement results of the MIMO antenna; 755-995 MHz, 1950-2690 MHz, 3420-3610 MHz and 5580-5950 MHz. As expected the isolation between elements was minimal at the lower operating frequencies due to the mutual surface currents along the length of the ground plane; however the calculated envelope correlation was still much less than 0.5 which provides acceptable diversity gain. Isolation in the midband, 3.5 GHz region, and highband regions all showed excellent diversity with ECC values less than 0.02. Additionally the measured radiation patterns displayed desirable omnidirectional characteristics in accord with the simulated model. Some small discrepancies between the measured and simulated radiation patterns arise from the soldered coaxial leads used to interface with the antenna however the general behavior was predictable and well modeled. Some slight inconsistencies in the electrically properties of the FR4 are likely the cause of the subtle shifts in high frequency resonant peaks of the fabricated antenna. Overall the measurement results showed that the fabricated antenna was in good agreement with the simulated model.

In conclusion the MIMO antenna presented was able to optimally utilize a large portion of the LTE spectrum in addition to covering the main WLAN and WMAN frequency bands. Utilizing various broadbanding techniques integrated on a small uniplanar substrate the proposed antenna occupies only a fractional volume within the size of an average cellular phone. Additionally the use of simple geometries and common cost effective materials allow the

antenna to be easily fabricated with readily available manufacturing techniques. The novel multiband uniplanar MIMO antenna discussed in this thesis represents a practical option for use within future generations of mobile communication technology.

References

[1] "The Mobile Economy 2015," Groupe Speciale Mobile Association (GSMA), London, United Kingdom, 2015.

[2] International Telecommunications Union, *Telecommunication/ICT Indicators - Yearbook of Statistics*. ITU, 2014.

[3] C. S. Patil, R. R. Karhe, and M. A. Aher, "Review on Generations in Mobile Cellular Technology," *Int. J. Emerg. Technol. Adv. Eng.*, vol. 2, pp. 614–619, 2012.

[4] E. Dahlman, S. Parkvall, and J. Skold, *4G LTE/LTE-Advanced for Mobile Broadband*. Amsterdam: Elsevier/Academic Press, 2011.

[5] M. R. Bhalla and A. V. Bhalla, "Generations of mobile wireless technology: A survey," *Int. J. Comput. Appl. 0975–8887*, vol. 5, no. 4, 2010.

[6] ITU-R, "International mobile telecommunications-2000 (IMT-2000)," Recomendation ITU-R M.287-2, Feb. 1997.

[7] ITU-R, "Principles for the process and development of IMT-Advanced," Resolution ITU-R 57, Oct. 2007.

[8] M. Jamil, S. P. Shaikh, M. Shahzad, and Q. Awais, "4G: The future mobile technology," in *TENCON 2008-2008 IEEE Region 10 Conference*, 2008, pp. 1–6.

[9] A. Ali and A. Barakabitze, "Evolution of LTE and Related Technologies Toward IMT-Advanced," *Int. J. Adv. Res. Comput. Sci. Softw. Eng.*, vol. 5, no. 1, Jan. 2015.

[10] I. F. Akyildiz, D. M. Gutierrez-Estevez, and E. C. Reyes, "The evolution to 4G cellular systems: LTE-Advanced," *Phys. Commun.*, vol. 3, no. 4, pp. 217–244, Dec. 2010.

[11] ITU-R, "Requirements related to technical performance for IMT-Advanced radio interface(s)," Rep. ITU-R M.2134, 2008.

[12] E. U. Terrestrial, "LTE; Evolved Universal Terrestrial Radio Access Network (E-UTRAN); X2 data transport (3GPP TS 36.424 version 12.0. 0 Release 12)," 2011.

[13] D. Gesbert and J. Akhtar, "Breaking the barriers of Shannon's capacity: An overview of MIMO wireless systems," *Signal Process.*, vol. 1, no. B2, p. B3, 2002.

[14] K. I. Pedersen, J. B. Andersen, J. P. Kermoal, and P. Mogensen, "A stochastic multiple-input-multiple-output radio channel model for evaluation of space-time coding algorithms," in *Vehicular Technology Conference, 2000. IEEE-VTS Fall VTC 2000. 52nd*, 2000, vol. 2, pp. 893–897.

[15] B. P. Lathi and Z. Ding, *Modern Digital and Analog Communication Systems*. New York: Oxford University Press, 2009.

[16] T. Asoke, Y. Roopa, and A. Hasan, *Mobile computing: technology, applications, and service creation*. New Delhi: McGraw Hill.

[17] S. Banerji and R. S. Chowdhury, "Wi-Fi & WiMAX: A Comparative Study," *ArXiv Prepr. ArXiv13022247*, 2013.

[18] C. A. Balanis, *Antenna Theory - Analysis and Design*, Third Edition. Hoboken, NJ: Wiley Interscience, 2005.

[19] W. L. Stutzman and G. A. Thiele, *Antenna Theory and Design*. Hoboken, NJ: Wiley, 2013.

[20] R. G. Vaughan and J. B. Andersen, "Antenna diversity in mobile communications," *Veh. Technol. IEEE Trans. On*, vol. 36, no. 4, pp. 149–172, 1987.

[21] S. Blanch, J. Romeu, and I. Corbella, "Exact representation of antenna system diversity performance from input parameter description," *Electron. Lett.*, vol. 39, no. 9, pp. 705–707, 2003.

[22] V. Plicanic, Z. Ying, T. Bolin, G. Kristensson, and A. Derneryd, "Antenna diversity evaluation for mobile terminals," in *Antennas and Propagation, 2006. EuCAP 2006. First European Conference on*, 2006, pp. 1–3.

[23] I. Salonen and P. Vainikainen, "Estimation of signal correlation in antenna arrays," *Journ. Int. Nice Sur Antennes*, vol. 2, pp. 383–386, 2002.

[24] P. Hallbjorner, "The Significance of Radiation Efficiencies When Using S-Parameters to Calculate the Received Signal Correlation From Two Antennas," *Antennas Wirel. Propag. Lett.*, vol. 4, no. 1, pp. 97–99, Dec. 2005.

[25] B. Guo, "Antenna Diversity In Mobile Phone," Chalmers University of Technology, 2008.

[26] K. Rosengren and P.-S. Kildal, "Radiation efficiency, correlation, diversity gain and capacity of a six-monopole antenna array for a MIMO system: theory, simulation and measurement in reverberation chamber," *IEE Proc. - Microw. Antennas Propag.*, vol. 152, no. 1, p. 7, 2005.

[27] H. A. Wheeler, "Fundamental limitations of small antennas," *Proc. IRE*, vol. 35, no. 12, pp. 1479–1484, 1947.

[28] J.-H. Lu and Y.-S. Wang, "Planar Compact Tablet Monopole Antenna for LTE/WWAN System."

[29] J.-H. Lu and F.-C. Tsai, "Planar Internal LTE/WWAN Monopole Antenna for Tablet Computer Application," *IEEE Trans. Antennas Propag.*, vol. 61, no. 8, pp. 4358–4363, Aug. 2013.

[30] W.-S. Chen and W.-C. Jhang, "A Planar WWAN/LTE Antenna for Portable Devices," *IEEE Antennas Wirel. Propag. Lett.*, vol. 12, pp. 19–22, 2013.

[31] L. Tchoketch-Kebir and B. Tlili, “Dual Frequency Broadband Planar Monopole Antenna for LTE Applications,” presented at the Loughborough Antennas & Propagation Conference, 2013.

[32] D. Navarro-Mendez, L. Carrera-Suarez, E. Antonino-Daviu, M. Ferrando-Bataller, M. Baquero-Escudero, M. Gallo, and D. Zamberlan, “Compact Wideband Vivaldi Monopole for LTE Mobile Communications,” *IEEE Antennas Wirel. Propag. Lett.*, pp. 1–1, 2015.

[33] L. Lizzi and A. Massa, “Dual-Band Printed Fractal Monopole Antenna for LTE Applications,” *IEEE Antennas Wirel. Propag. Lett.*, vol. 10, pp. 760–763, 2011.

[34] Kin-Lu Wong and Shu-Chuan Chen, “Printed Single-Strip Monopole Using a Chip Inductor for Penta-Band WWAN Operation in the Mobile Phone,” *IEEE Trans. Antennas Propag.*, vol. 58, no. 3, pp. 1011–1014, Mar. 2010.

[35] G. Augustin, B. Chacko, and T. Denidni, “Uniplanar Folded Monopole Antenna for Mobile Phone Applications in LTE/GSM/UMTS/WiFi Band,” 2014.

[36] J.-L. Guo, H.-M. Chin, and J.-H. Lu, “Planar multi-band monopole antenna for WWAN/LTE operation in a mobile device,” in *Antennas & Propagation (ISAP), 2013 Proceedings of the International Symposium on*, 2013, vol. 1, pp. 168–171.

[37] Jui-Han Lu and Jia-Ling Guo, “Small-Size Octaband Monopole Antenna in an LTE/WWAN Mobile Phone,” *IEEE Antennas Wirel. Propag. Lett.*, vol. 13, pp. 548–551, 2014.

[38] S.-H. Chang and W.-J. Liao, “A Broadband LTE/WWAN Antenna Design for Tablet PC,” *IEEE Trans. Antennas Propag.*, vol. 60, no. 9, pp. 4354–4359, Sep. 2012.

[39] W. Xiao, R.-P. Huang, W.-L. Lin, and Y.-L. Ban, “Simple octa-band monopole antenna with rectangular-loop-loaded meandered line for LTE/WWAN smartphone applications,” in *Microwave Workshop Series on RF and Wireless Technologies for Biomedical and Healthcare Applications (IMWS-BIO), 2013 IEEE MTT-S International*, 2013, pp. 1–4.

[40] M. S. Sharawi, Y. S. Faouri, and S. S. Iqbal, “Design of an electrically small meander antenna for LTE mobile terminals in the 800 MHz band,” in *GCC Conference and Exhibition (GCC), 2011 IEEE*, 2011, pp. 213–216.

[41] M. I. Jais, M. F. Jamlos, M. F. Malek, M. Jusoh, I. Adam, N. I. Iliyes, and P. Saad, “Design Analysis of 2.45 GHz Meander Line Antenna (MLA),” 2012, pp. 628–631.

[42] L. Jian-Ying, Y. Y. Kyi, and G. Y. Beng, “Analysis of dual-band meander line antenna,” in *Antennas and Propagation Society International Symposium 2006, IEEE*, 2006, pp. 2033–2036.

[43] Y. J. Cho, S. H. Hwang, and S. O. Park, “Printed antenna with folded non-uniform meander line for 2.4/5 GHz WLAN bands,” *Electron. Lett.*, vol. 41, no. 14, pp. 786–788, 2005.

[44] C. C. Hsu and H. H. Song, “Design, Fabrication, and Characterization of a Dual-Band Electrically Small Meander-line Monopole Antenna for Wireless Communications,” *Int. J. Electromagn. Appl. Issue-3*, vol. 2, 2013.

[45] D. Misman, I. Salamant, M. Kadir, and M. Che Rose, “The Effect of Conductor Line to Meander Line Antenna Design,” in *Applied Electromagnetics, Asia-Pacific*, 2007.

[46] T.-N. Mai, A.-C. Lepage, B. Huyart, and Y. Pinto, “Compact multi-band planar monopole antenna for LTE terminals,” in *Antennas and Propagation (EuCAP), 2014 8th European Conference on*, 2014, pp. 3278–3280.

[47] K. S. Sultan, H. H. Abdullah, E. A. Abdallah, and E. A. Hashish, “Low-SAR, Miniaturized Printed Antenna for Mobile, ISM, and WLAN Services,” *IEEE Antennas Wirel. Propag. Lett.*, vol. 12, pp. 1106–1109, 2013.

[48] Yuan Yao, Junsheng Yu, and Xiaodong Chen, “Compact Multi-band Planar Antenna Design,” in *Asia-Pacific Microwave Conference*, 2012.

[49] K. Mishra, D. Garg, and M. Jaju, “Design of a Compact PIFA for PCS Applications,” *Dep. Electron. Commun. Eng. Indian Inst. Technol. Guwahati India*.

[50] C.-J. Park, J.-W. Kim, T.-G. Kim, and S.-J. Lee, “A Study on Fan Type PIFA for LTE Band Handy-phone Application,” in *Proceedings of the Asia-Pacific Microwave Conference*, 2011.

[51] T.-W. Kang and K.-L. Wong, “Simple small-size coupled-fed uniplanar PIFA for multiband clamshell mobile phone application,” *Microw. Opt. Technol. Lett.*, vol. 51, no. 12, pp. 2805–2810, Dec. 2009.

[52] Y. Sung and S. Lee, “Reconfigurable PIFA with a parasitic strip line for a hepta-band WWAN/LTE mobile handset,” *IET Microw. Antennas Propag.*, vol. 9, no. 2, pp. 108–117, Jan. 2015.

[53] S. Jeon, Y. Liu, S. Ju, and H. Kim, “PIFA with parallel resonance feed structure for wideband operation,” *Electron. Lett.*, vol. 47, no. 23, pp. 1263–1265, 2011.

[54] P. Li, J. Pan, D. Yang, Z.-P. Nie, and J. Xing, “A novel quad-band (GSM850 to IEEE 802.11 a) PIFA for mobile handset,” *Prog. Electromagn. Res.*, vol. 137, pp. 539–549, 2013.

[55] J. Ilvonen, R. Valkonen, J. Holopainen, and V. Viikari, “Design Strategy for 4G Handset Antennas and a Multiband Hybrid Antenna,” *IEEE Trans. Antennas Propag.*, vol. 62, no. 4, pp. 1918–1927, Apr. 2014.

[56] R. Janaswamy, “Effect of element mutual coupling on the capacity of fixed length linear arrays,” *IEEE Antennas Wirel. Propag. Lett.*, vol. 1, no. 1, pp. 157–160, 2002.

[57] G. Srinivas, D. Jabin, and A. K. Singh, “Multiband MIMO antenna with reduction in mutual coupling and ECC,” in *Engineering and Systems (SCES), 2014 Students Conference on*, 2014, pp. 1–5.

[58] S. Shoaib, I. Shoaib, N. Shoaib, X. Chen, and C. G. Parini, “Design and Performance Study of a Dual-Element Multiband Printed Monopole Antenna Array for MIMO Terminals,” *IEEE Antennas Wirel. Propag. Lett.*, vol. 13, pp. 329–332, 2014.

[59] S. Zhang, K. Zhao, Z. Ying, and S. He, “Adaptive Quad-Element Multi-Wideband Antenna Array for User-Effective LTE MIMO Mobile Terminals,” *IEEE Trans. Antennas Propag.*, vol. 61, no. 8, pp. 4275–4283, Aug. 2013.

[60] H. S. Singh, B. R. Meruva, G. K. Pandey, P. K. Bharti, and M. K. Meshram, “Low mutual coupling between MIMO antennas by using two folded shorting strips,” *Prog. Electromagn. Res. B*, vol. 53, pp. 205–221, 2013.

[61] H. S. Singh, G. K. Pandey, P. Bharti, and M. Meshram, “Spiral-shaped High Isolated Monopole MIMO/Diversity Antenna for Small Mobile Terminals,” in *Advances in Communications and Control Systems*.

[62] M. S. Sharawi, S. S. Iqbal, and Y. S. Faouri, “An 800 MHz 2 x 1 Compact MIMO Antenna System for LTE Handsets,” *IEEE Trans. Antennas Propag.*, vol. 59, no. 8, pp. 3128–3131, Aug. 2011.

[63] X. Zhao, Y. Lee, and J. Choi, “Design of a compact planar MIMO antenna for LTE mobile application,” in *Antennas and Propagation (ISAP), 2012 International Symposium on*, 2012, pp. 1365–1368.

[64] M. S. Sharawi, Y. S. Faouri, and S. S. Iqbal, “Design and fabrication of a dual electrically small MIMO antenna system for 4G terminals,” in *Microwave Conference (GeMIC), 2011 German*, 2011, pp. 1–4.

[65] Z. Z. Abidin, Y. Ma, R. A. Abd-Alhameed, K. N. Ramli, D. Zhou, M. S. Bin-Melha, J. M. Noras, and R. Halliwell, “Design of 2x2 U-shape MIMO slot antennas with EBG material for mobile handset applications.,” 2011.

[66] K. A. Abdelwahab, E. A. Abdallah, and M. Aboul-Dahab, “Compact Quad-band PIFA Antenna for LTE Handsets with MIMO and Low Mutual Coupling,” *Sess. 3A6 4 Focus. SC4 Chall. Small Antennas*, p. 979.

[67] G. Li, H. Zhai, Z. Ma, C. Liang, R. Yu, and S. Liu, “Isolation-Improved Dual-Band MIMO Antenna Array for LTE/WiMAX Mobile Terminals,” *IEEE Antennas Wirel. Propag. Lett.*, vol. 13, pp. 1128–1131, 2014.

[68] E. Michailidis, C. Tsimenidis, and G. Chester, “Mutual coupling reduction in a linear two element patch array and its effect on theoretical MIMO capacity,” in *Antennas and Propagation Conference, 2008. LAPC 2008. Loughborough*, 2008, pp. 457–460.

[69] Fan Yang and Y. Rahmat-Samii, “Microstrip antennas integrated with electromagnetic band-gap (EBG) structures: A low mutual coupling design for array applications,” *IEEE Trans. Antennas Propag.*, vol. 51, no. 10, pp. 2936–2946, Oct. 2003.

[70] F. Y. Zulkifli and E. T. Rahardjo, “Compact MIMO Microstrip Antenna with Defected Ground for Mutual Coupling Suppression,” in *Progress in Electromagnetics Research Symp.(PIERS), Marrakesh, Morocco*, 2011, pp. 89–92.

[71] M.-S. Han and J. Choi, “MIMO antenna using a decoupling network for next generation mobile application,” in *Communications and Information Technology, 2009. ISCIT 2009. 9th International Symposium on*, 2009, pp. 568–571.

[72] J.-F. Li and Q.-X. Chu, “Compact MIMO antenna with simple decoupling method,” in *Microwave Conference (EuMC), 2013 European*, 2013, pp. 774–777.

[73] D. Kim, K. Kwon, D. Kang, and J. Choi, “MIMO antenna with decoupling network for headset applications,” in *Microwave Conference Proceedings (APMC), 2013 Asia-Pacific*, 2013, pp. 46–48.

[74] J. Kim, M. Han, C. Lee, and J. Choi, “Dual band MIMO antenna using a decoupling network for WLAN application,” in *Advanced Communication Technology (ICACT), 2011 13th International Conference on*, 2011, pp. 624–627.

[75] D. H. Margaret, M. R. Subasree, S. Susithra, S. S. Keerthika, and B. Manimegalai, “Mutual coupling reduction in MIMO antenna system using EBG structures,” in *Signal Processing and Communications (SPCOM), 2012 International Conference on*, 2012, pp. 1–5.

[76] M. N. Sadiku, “A simple introduction to finite element analysis of electromagnetic problems,” *Educ. IEEE Trans. On*, vol. 32, no. 2, pp. 85–93, 1989.

[77] CNC, “Accurate 427 (A427) CNC Milling Machine Specifications,” Acurate CNC, PCB Prototyping Machine, 2014.

[78] D. Ballo, *Network analyzer basics*. Hewlett-Packard Company Microwave Instruments Division, 1997.